

NORTHWESTERN UNIVERSITY

Electrostatically Driven Transformation in Assembly of Charged Amphiphiles

A DISSERTATION

for the degree

DOCTOR OF PHILOSOPHY

Field of Materials Science and Engineering

By

Changrui Gao

EVANSTON, ILLINOIS

September 2018

Abstract

Electrostatically Driven Transformation in Assembly of Charged Amphiphiles

Changrui Gao

Self-assembly is an important process in biological system to build various bioactive structures from small amphiphilic molecules. The structural versatility of amphiphile self-assembly also provides a unique platform for the design of functional soft materials with controllable structural features. However, little is known about the correlation between external stimuli, intermolecular forces and the self-assembly structure, which is extremely significant for understanding the transformation of assembly structures in biological processes as well as the materials design. Intermolecular electrostatic interaction is one of the dominant forces for driving the self-assembly process. In this dissertation, different self-assembly system will be investigated and I will present how electrostatic interaction affects the self-assembly structures and properties. I will first demonstrate a modular series of $C_{16}K_n$ peptide amphiphiles where intermolecular electrostatic interaction and steric repulsion can be controlled by solution pH and size of the ionizable headgroup. A large diversity of self-assembly structures, ranging from spherical micelle to bilayer nanotube, can be observed through subtle changes in the electrostatic and steric repulsions. Moreover, $C_{16}K_1$ peptide bilayer membrane exhibits a structural transformation from planar bilayer ribbon to rolled-up cochleate structure when increasing the ionic strength, and the interlayer spacing in the cochleate structure is directly related to the solution Debye length. Theoretical studies on each step of the morphological transition successfully correlate the electrostatic interaction with the equilibrium structures of the membrane. Other than peptide

amphiphile, thermodynamic phase behaviors of phospholipid bilayer membranes consisting of binary lipid molecules are also studied. The gel-to-fluid phase transition temperatures of lipid bilayers with DMTAP (+1)/DMPC (0) and DMTAP (+1)/DMPS (-1) binary mixtures are measured to explore the contribution of intermolecular electrostatic attraction to stabilizing the gel-phase lipid bilayer membrane. In addition, 2-D lattices of lipid bilayers show “universal” thermal expansion behavior for all lipid binary mixtures, and the intermolecular spacing is also minimized as the intermolecular electrostatic attraction increases.

Acknowledgements

At the time of writing this thesis, I understand that my graduate studies are coming to the end. Despite the challenges and difficulties, my graduate studies eventually have a fairly happy ending, and I feel so grateful that I was not walking alone. So before I start the new endeavor in my life, I would like to acknowledge those who mentored me, helped me and supported me during my Ph.D. pursuit.

First and foremost, I would like to thank my advisor Prof. Michael J. Bedzyk. When I joined his group in 2013, I knew very little about my research projects and the X-ray physics. Prof. Bedzyk is very patient and approachable, he provided lots of guidance and support, especially on X-ray skills and knowledge. He also encouraged me to find my own interests in my research area, and gave valuable advices for my personal development. During my Ph.D. years in his group, I have also learned a lot from Prof. Bedzyk on the importance of critical thinking and “spirit of the craftsman”, and I will certainly carry those to my future careers.

I would thank Prof. Monica Olvera de la Cruz for her support on the theoretical studies of my research projects. I learn a lot from her ways of thinking and solving problems during our discussions, and she also shows me the intellectual curiosity and visionary perspective. Other than the theoretical studies, she also provides her unique insight on the experimental design, as well as writing scientific papers. I would also thank Prof. Jiaxing Huang and Prof. Pulak Dutta for serving on my thesis committee. Their advices on my thesis are very inspiring.

During my PhD studies, I feel truly blessed to work with all the wonderful Bedzyk group members. In particular, I have to show my special appreciation to Dr. Sumit Kewalramani, for mentoring and helping me throughout my research. Sumit spent a lot of time guiding me on the every single aspect of my projects, and he was also super-patient throughout the time. I would also thank Dr. Li Zeng for the guidance and friendship, and Jerry Carsello for training and helping me in the X-ray lab. I also feel very grateful to have the amazing group members: Dr. Bor-rong Chen, Dr. Stephanie Moffitt, Dr. Xiao Chen, Dr. Boris Harutyunyan, Dr. Gavin Campbell, Dr. Liane Moreau, Janak Thapa, Kurinji Krishnamoorthy, Katherine Harmon, Anusheela Das, Dr. Bo-Hong Liu, Dr. Narayanachari and Dr. Guennadi Evmenenko.

I would also thank Dr. Liam Palmer for introducing the analytical characterization techniques for my research, and sharing his knowledge on the molecular chemistry, and thank Dr. Mark Karver for producing high quality samples for our experiments. I thank Honghao Li for conducting the simulations for the theoretical support of my studies. I also want to acknowledge Dr. Steve Weigand and Denis Keane at the DND-CAT and Byeongdu Lee at Sector 12-ID for their assistances in setting up the small angle X-ray scattering experiments, and also Dr. Reiner Bleher for training me multiple times on the Cryo-TEM imaging.

I also want to thank my parents for raising me up and being supportive when I decided to study in a place thousands of miles away from home. They encouraged me to follow my dream and gave me great advices on my career development.

Finally I want to honor my wife and my beloved Shuyu Li for her deep affection and strong support in my life. She encouraged me a lot during my PhD research and always listened to me

when I shared my work and life experience with her. She also gave me great advices on the presentation and communication skills. I feel really fortunate to have her during my graduate studies.

For Shuyu

TABLE OF CONTENTS

Abstract	2
Acknowledgements	4
TABLE OF CONTENTS	8
LIST OF FIGURES	11
LIST OF TABLES.....	19
Chapter 1. Introduction	20
Chapter 2. Overview.....	25
Chapter 3. Characterization Methods	28
1. Small/Wide Angle X-ray Scattering (SAXS)	28
2. Grazing-Incidence Wide Angle X-ray Scattering (GIWAXS).....	33
3. Transmission Electron Microscopy (TEM)	35
4. Atomic Force Microscopy	37
5. Dynamic Light Scattering (DLS)	38
6. Differential Scanning Calorimetry (DSC)	40
Chapter 4. Polymorphism of Peptide Amphiphile Assembly Induced by Headgroup Charge and Size Regulation.....	42
4.1. Introduction.....	42
4.2. Materials and Methods.....	44
4.2.1. Sample Preparation	44
4.2.2. Characterization Methods	45

	9
4.2.3. Monte-Carlo Simulations:.....	46
4.3. Results and Discussion.....	47
4.4. Summary.....	64
Chapter 5. Electrostatic Control of Nanoribbon-to-Cochleate Transition in a Charged Peptide Amphiphile Assembly.....	65
5.1. Introduction.....	65
5.2 Materials and Methods.....	67
5.2.1. Sample Preparation.....	67
5.2.2. Characterization Methods.....	68
5.3 Results and Discussion.....	68
5.4. Summary.....	91
Chapter 6. Thermodynamic Phase Behavior in Membranes of Binary Phospholipid Mixtures.....	92
6.1. Introduction.....	92
6.2 Materials and Methods.....	93
6.2.1. Sample Preparation.....	93
6.2.2. Characterization Methods.....	94
6.3. Results and Discussion.....	95
6.4. Summary.....	106
Chapter 7. Summary and Outlook.....	107
7.1. Summary.....	107
7.2 Outlook.....	109
7.2.1. Cochleate Encapsulation Ability.....	109

7.2.2. C ₁₆ K ₁ Membrane Intrinsic Curvature.....	109
Appendix.....	111
Appendix A. Alignment of C₁₆K₁ Nanoribbons Under Shear Flow	111
A.1. Anisotropic SAXS Pattern Induced by Nanoribbon Alignment	111
A.2. Shear-aligned Ribbons Deposited on Substrate	115
Appendix B. Solution WAXS Analysis on Flat C₁₆K₁ Bilayer	118
Appendix C. Theoretical Calculation of Ribbon-to-cochleate Transition	120
C.1. Ribbon-to-sheet Transition.....	120
C.2. Membrane Rolling.....	124
C.3. Interlayer Separation vs. Salt Concentration.....	125
Appendix D. SAXS and WAXS Data Processing and Fitting.....	129
D.1. SAXS/WAXS Data Processing.....	129
D.2. SAXS Data Analysis and Fitting Programs	129
Reference:.....	132

LIST OF FIGURES

- Figure 1.1. Schematic of (a) spherical micelle, (b) planar bilayer, (c) bilayer vesicle and (d) fiber.
 21
- Figure 1.2. Critical packing parameter and the corresponding assembled structure. (Image from Israelachvili[12])..... 22
- Figure 3.1. Theoretical SAXS intensity profile of dilute monodisperse spheres, showing Guinier and Porod regime of the curve..... 31
- Figure 3.2. Schematic of the SAXS/MAXS/WAXS detector system, SAXS, MAXS and WAXS patterns are collected simultaneously by three separate CCD X-ray areal detectors. 33
- Figure 3.3 Schematic of GIWAXS experimental geometry. The angle of incidence, θ , is close to the critical angle of the sample. A 2D detector (or phosphor image plate) is used to simultaneously collect the scattered X-rays..... 34
- Figure 3.4. Cryo-TEM specimen preparation by plunge-freezing. Aqueous sample solution is applied onto glow-discharged (hydrophilic) holey carbon film supported by EM grid. Excess solution is removed with filter paper from one or both sides. Blotted grid is rapidly plunged into a cryogen precooled at liquid nitrogen temperature. Biomolecules embedded in thin amorphous ice film are observed in cryo-electron microscope. 36
- Figure 3.5. Schematic representation shows the principle of size measurement in Dynamic Light Scattering. The intensity fluctuation due to the Brownian motion is more frequent for

smaller particles (left image), which leads to faster decay of autocorrelation function. The decay rate can be used to calculate the particle size. 39

Figure 4.1. Molecular structures of positively charged $C_{16}K_4$, $C_{16}K_3$, $C_{16}K_2$, and $C_{16}K_1$ peptide amphiphiles 44

Figure 4.2. (a) $C_{16}K_n$ titration curves showing how pH changes as function of the volume of NaOH added. All $C_{16}K_n$ exhibit single buffer stage. (b) Averaged $C_{16}K_n$ headgroup charge as a function of pH obtained through Henderson-Hasselbach equation of monoprotic acid (eq. 3.3). pKa is determined from the titration curves. (c) Averaged $C_{16}K_2$ headgroup charge as a function of pH in standard water environment obtained by Monte Carlo theoretical simulation, showing deprotonation around pH 8.2. 49

Figure 4.3. In situ small- and wide-angle X-ray scattering data showing the background subtracted scattered intensity profile for $C_{16}K_n$ as a function of solution pH. The data sets are offset vertically for clarity. The solid black curves are the best fits over the SAXS region ($0.1 < q < 8 \text{ nm}^{-1}$) using different models (Table 4.1). 51

Figure 4.4. Representative cryogenic TEM images of self-assembly formed by $C_{16}K_1$. Flat ribbon morphology with high aspect ratio is found when pH is low (left image). When the pH increases, the flat morphology transforms into tubular structures (right image). 54

Figure 4.5. Representative cryogenic TEM images of self-assembly formed by $C_{16}K_2$. No elongated objects are observed at pH 5, while the solution at pH 8 shows long fibers (red arrow). The black rod in the center is lacey carbon grid. Black stains in the background are

excessive ethane from sample preparation. At pH 9, flat ribbons can be observed, and there are also indications of long fibers (red arrow) similar to the fibers formed at pH 8. 57

Figure 4.6. Representative cryogenic TEM images of self-assembly formed by $C_{16}K_3$. No elongated objects are observed at pH 5, and the solution at pH 8.4 shows only the long fibers. Further increase to pH 9 induces the formation of flat ribbons in addition to long fibers. 60

Figure 4.7. Representative cryogenic TEM images of self-assembly formed by $C_{16}K_4$. Similar with $C_{16}K_3$, no objects are observed at low pH. The formation of both flat ribbons and long fibers is shown at pH 10. Intermediate phase with the only cylindrical fibers is not captured in $C_{16}K_4$ 60

Figure 4.8. Phase diagram showing the formation and transition of self-assembly morphology of $C_{16}K_n$ peptide amphiphile as a function of headgroup size and pH. 63

Figure 5.1. (a) Molecular structure of +1 charged $C_{16}K_1$ peptide with estimates for hydrophobic tail length and hydrophilic headgroup length. The molecular conformation was derived from an MD simulation for a single $C_{16}K_1$ molecule in water using the Universal force field.[56] (b) Atomic Force Microscopy image at a silica/water interface showing high aspect ratio $C_{16}K_1$ ribbons. (c) The height profile for a nanoribbon. The scan was performed along the green line in Figure 5.1b. 70

Figure 5.2. (a-d) AFM peakforce error images for $C_{16}K_1$ membranes at Si/NaCl solution interfaces. As the NaCl concentration increases, nanoribbon to isotropic sheet and to rolled-

up cochleate transformations are observed. (e-h) Cryogenic TEM images of cochleates exhibit scroll morphology and the internal multilayer features. It can be readily seen that the interbilayer spacing D within the cochleate structure decreases with increasing NaCl concentration..... 71

Figure 5.3. (a) Background subtracted *in situ* small-angle X-ray scattering intensity profile for $C_{16}K_1$ ribbon in zero salt condition. The solid black curve is the best fit over the range of $0.1 < q < 6 \text{ nm}^{-1}$ using a symmetric bilayer model. (b) Background subtracted *in situ* wide-angle X-ray scattering intensity profile for $C_{16}K_1$ ribbons in pure water shows diffraction peaks over the range of $10 < q < 30 \text{ nm}^{-1}$. The solid black curve is the simulated diffraction pattern. (c) The interdigitated $C_{16}K_1$ bilayer structure and electron density profile determined from small-angle X-ray scattering data. (d) 2D oblique unit cell and lattice parameters derived from wide-angle X-ray scattering data..... 73

Figure 5.4. Grazing-Incidence X-ray scattering from $C_{16}K_1$ bilayer drop-casted on Si (001) substrate. Scattered intensity was scaled from blue (weak) to red (strong). The long exposure time required to clearly discern the intensity rods at $q_{xy} = 2.5, 5, 0, 7.5$ and 10 nm^{-1} resulted in detector saturation in the region $13 < q_{xy} < 16 \text{ nm}^{-1}$. Therefore, the three diffraction peaks from the packing of alkyl tails observed in solution SAXS in this region appear as a broad maximum in GIXS, and cannot be separated out..... 77

Figure 5.5. (a) Background subtracted *in situ* small- and wide-angle X-ray scattering data for 4 mM $C_{16}K_1$ as the solution NaCl concentration is increased from 1 to 5 mM. The data sets are offset vertically for clarity. For NaCl concentration $c \geq 2 \text{ mM}$, the appearance of

multiple intensity modulations for $q < 0.1 \text{ nm}^{-1}$ and the reduction in the intensity of the sharp Bragg reflections in the WAXS regime are due to the ribbon-to-cochleate transition.

(b) Background subtracted *in situ* small-angle X-ray scattering data for 4 mM C_{16}K_1 as the solution NaCl concentration is increased from 5 to 50 mM. The data sets are offset vertically for clarity. The position of first order small angle diffraction peaks ($0.1 < q < 1 \text{ nm}^{-1}$) is used to determine the interbilayer spacing D inside the cochleate. We note that the data in (a) and (b) are from different synthetic batches of C_{16}K_1 . Small deviations, for example, in the interbilayer spacing D were observed from batch to batch. The relationship between D and the NaCl concentration in the text and in (c) is based on the data in (b). (c) SAXS-derived interbilayer spacing of cochleate varies linearly as function of $c^{-1/2}$, where c is molar NaCl concentration. The solid black line is the best fit: $D \text{ (nm)} = 6.40 + 2.05 \times c^{-1/2}$.

..... 78

Figure 5.6. Background subtracted *in-situ* SAXS/WAXS intensity profiles of 10 mM C_{16}K_1 solution as the NaCl concentration is increased from 1 to 5 mM. The data sets are offset vertically for clarity. The data shows similar trends as the 4 mM C_{16}K_1 solution. 80

Figure 5.7. (a) Schematic representation of C_{16}K_1 nanoribbon showing ribbon dimensions used for the energy calculation. (b) The calculated membrane energy per unit area in equation 5.1 as a function of the inverse of membrane aspect ratio D_1/L for 5 different salt concentrations. 84

Figure 5.8. (a) An array of charged species with predefined array length L_0 and intrinsic spontaneous curve C_0 . This model is used to calculate the sum of electrostatic and curvature

energy as a function of salt concentration and curvature. (b) Total energy per unit length in equation 5.2 versus array curvature C_l for different salt concentrations ($\mathbf{3} > \mathbf{2} > \mathbf{1} > \text{No salt}$).
 87

Figure 5.9. (a) The geometry of the lamellar stack. The thicknesses of the membrane and the interbilayer aqueous regions are δ and d , respectively. (b) Theoretical prediction showing a linear relation between interbilayer spacing $D = \delta + d$ and $c^{-1/2}$, where c is molar NaCl concentration. The deviation relative to experimental result is likely due to the assumption of a planar stack in calculations, as compared to the experimentally observed spiral geometry. 90

Figure 6.1. Molecular structures of phospholipid molecules DMPS (-1), DMPC (0), and DMTAP (+1) described in Table 1. 98

Figure 6.2. *In situ* small- and wide-angle X-ray scattering data showing background subtracted scattered intensity profiles for pure DMPS lipid bilayers as function of temperature. The data sets are offset vertically for clarity. The solid black curves are the best fits of SAXS data at 25 °C and 50 °C using planar bilayer and vesicle models, respectively. The WAXS diffraction peak at $q = 15 \text{ nm}^{-1}$ represents the crystalline order of gel-phase lipid bilayer. . 98

Figure 6.3. Differential Scanning Calorimetry (DSC) measurement for solution of pure DMPS lipid bilayers, shows the gel-to-fluid phase transition temperature at 37.5°C. 99

Figure 6.4. WAXS-derived gel-to-fluid transition temperature vs. composition for DMTAP (+1)/DMPS (-1) and DMTAP (+1)/DMPC (0) binary lipid mixtures showing inverted

parabolas with highest melting temperature close to 50%/50% mixture. The error bar of each data point is from the temperature step size (3 to 5 °C) of *in situ* X-ray scattering measurements..... 99

Figure 6.5. Cryo-TEM image of DMPS vesicles formed at 50°C, which is above DMPS transition temperature (~38°C). The size of vesicle in this image ranges between 20 and 50 nm. 101

Figure 6.6. DMPS vesicle size distribution determined from Dynamic Light Scattering (DLS). The number-averaged diameter of vesicle is measured to be 27.0 nm, and polydispersity of size distribution is 0.33. Those values are highly consistent with SAXS fitting result. 102

Figure 6.7. Lattice parameter of DMPS (-1)/DMTAP (+1) and DMPC (0)/DMTAP (+1) gel phase lipid bilayers as a function of temperature..... 104

Figure 6.8. (a) Lattice parameter of DMPS (-1)/DMTAP (+1) and DMPC (0)/DMTAP (+1) lipid bilayer as a function of lipid composition under the fixed temperature. The lattice parameter values are determined from Figure 6.7. (b) Average area per lipid $\langle A \rangle$ as a function of the composition χ_{TAP} in DMTAP (0)/DMTAP (+1) lipid bilayer. (c) A proposed schematic picture of the observed change in the area per lipid versus lipid composition χ_{TAP} . Only headgroups of the lipids are shown here. 105

Figure 7.1. AFM Peakforce images showing right-handed spiral marks on C_{16}K_1 cochleate structure. The scale bars in both image a and b represent 2 μm 110

Figure A.1. (a) 2D SAXS pattern of $C_{16}K_1$ nanoribbon formed at pH 4.6 showing anisotropic shape. (b) 2D SAXS pattern of $C_{16}K_1$ nanotube formed at pH 10 showing isotropic shape. (c) Schematic representation of *in situ* SAXS measurement of $C_{16}K_1$ nanoribbon aligned in the capillary flow cell. The alignment of the nanoribbons leads to the anisotropic SAXS pattern. 112

Figure A.3. (a) Aligned $C_{16}K_1$ nanoribbons on solid substrate prepared by shearing the $C_{16}K_1$ solution. (b) Grazing Incidence X-ray diffraction data showing intensity versus in-plane scattering vector q_{xy} . The diffraction peaks at 13.9 and 15.0 nm^{-1} coincide with solution wide-angle X-ray scattering data. (c) The intensity of both diffraction peaks shows no significant variation when changing the in-plane rotation angle of aligned nanoribbons. . 116

Figure C.1. Simple membrane model with uniform charge density to understand aspect ratio (L/D_1) change in $C_{16}K_1$ bilayer membrane as the salt concentration increases. 120

LIST OF TABLES

Table 3.1. Common form factors of particular shapes such as spheres, core-shell spheres, ellipsoids, cylinders, and disks.[27].....	30
Table 4.1. Fitting models used for C ₁₆ K _n SAXS fittings	52
Table 4.2. WAXS diffraction peak positions and derived lattice structures of C ₁₆ K _n bilayers	62
Table 5.1. Numerical values of parameters used in equation 5.1	85
Table 5.2. Numerical values of parameters used in equation 5.2	87
Table 5.3. Numerical values of parameters used in equation 5.3, 5.4 and 5.5	90
Table 6.1. Selected compositions of lipid binary mixtures for SAXS/WAXS studies.....	97

Chapter 1. Introduction

Molecular self-assembly is defined as the process of spontaneous association of randomly distributed molecular units into highly organized supramolecular structures. The well-known examples of self-assembly are the folding of polypeptide chains into proteins, the folding of nucleic acid into their functional forms such as DNA and RNA, and the aggregation of phospholipid molecules into cell membrane. These self-assembly processes constitute the occurrence of life on our planet. In the modern research, molecular self-assembly has grown into an important topic in materials science because of their applications in fabricating functional biomaterials and soft electronic materials. For example, self-assembled amphiphilic diketopyrrolopyrrole-based oligothiophenes have been fabricated for organic field-effect transistors[1] and molecular bulk-heterojunction solar cells[2]. Furthermore, this type of structure can also incorporate with a large variety of materials to produce functional hybrid materials. Specifically, surface of carbon nanotubes[3] and metal nanowires[4] can be easily coated and modified by amphiphiles, which increase the biocompatibility of these materials and therefore have future significance in diagnostics and therapies.

A typical building block of those functional self-assembly structure is the amphiphilic molecule, which is a type of molecule possessing both hydrophilic and hydrophobic properties. The structure of common amphiphilic molecules consists of a polar hydrophilic headgroup grafted to a hydrophobic carbon chain. When dissolved in aqueous solution, these molecules can self-assemble into a large variety of aggregates such as micelles, fibers, planar membranes, and

vesicles (Figure 1.1). Unlike solid particles and rigid polymers, the forces that hold the molecules together in the self-assembled system are not strong covalent or ionic bonds, but the weak interactions such as van der Waals, hydrogen-bonding, π - π stacking and electrostatic interactions. Therefore, by varying the solution conditions and molecular structures, one could possibly modulate those weak intermolecular forces and change the size and shape of the resulting supramolecular structures, and ultimately open the gateways of constructing customized nanomaterials with desired functionalities. For example, unilamellar vesicles have been designed and synthesized for many different technologies such as drug delivery[5, 6], gene therapy[7], nano-reactors[8], and biomineralization[9]. Cylindrical fibers have also been fabricated and modified to build artificial extracellular matrix and promote tissue regeneration.[10, 11] These functional nanostructures could be formed through the careful selection and design of the amphiphilic molecules, as well as the control of the assembling environments.

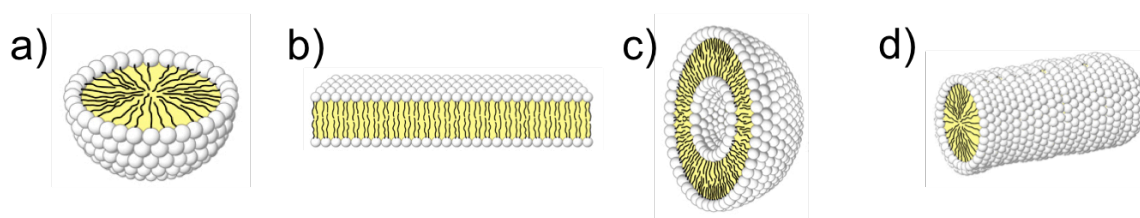


Figure 1.1. Schematic of (a) spherical micelle, (b) planar bilayer, (c) bilayer vesicle and (d) fiber.

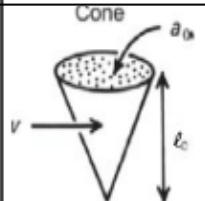
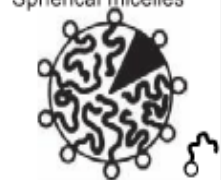
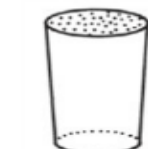
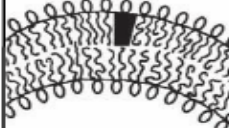
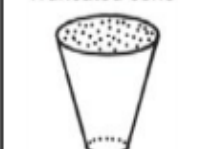
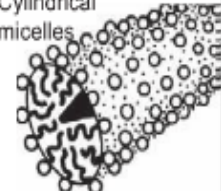
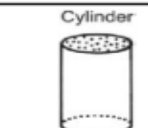
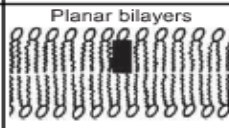
Critical packing parameter $v/a_0 l_c$	Critical packing shape	Structures formed	Critical packing parameter $v/a_0 l_c$	Critical packing shape	Structures formed
$< 1/3$	Cone 	Spherical micelles 	$1/2-1$	Truncated cone 	Flexible bilayers, vesicles 
$1/3-1/2$	Truncated cone 	Cylindrical micelles 	-1	Cylinder 	Planar bilayers 

Figure 1.2. Critical packing parameter and the corresponding assembled structure. (Image from Israelachvili[12])

The increasing needs for new applications continue to challenge the field of molecular self-assembly, through demanding precise control of the nano and the meso-scale architecture for desired functionalities. The earliest model to predict the self-assembly structure was brought up by Israelachvili.[12] He has summarized a simple and effective parameter to determine the geometry of self-assembly based on the molecular structure of the amphiphiles, which is known as the critical packing parameter $v/(a_0 l_c)$. In this parameter, v is the volume occupied by the hydrocarbon chain, a_0 is the effective cross-sectional area of the headgroup and l_c is the critical chain length that defines the maximum limit on how far the tail can extend. Figure 1.2 shows the summarized relationship between critical packing parameter and the self-assembled structures. When the packing parameter is smaller than $1/3$, the packing shape of each individual molecule is cone shape which forms spherical micelles. As packing parameter increases, the molecular shape becomes more cylindrical, which leads to other structures such as cylindrical

micelles and bilayers. The concept of critical packing parameter is widely invoked in the literature[13-15] to explain and predict the molecular self-assembly of amphiphiles. However, this theory does not fully consider the effect from some short-range and long-range intermolecular forces, which also play a critical role in determining the self-assembly structures. For example, β -sheet hydrogen bonding could lead the peptides to form an elongated nanostructures,[16, 17] and aromatic side chains in peptide could drive the self-assembly into amyloid-like fibrils due to π - π stacking.[18, 19] Although large variety of self-assembly structures have been developed for different applications, the connections between intermolecular interactions and equilibrium self-assembly structures in many molecular systems are still elusive. Therefore it remains a big challenge to precisely design and control the assembly nanostructure, and even the process of many basic structural transformations of self-assembly such as micelle-to-vesicle transition is still not well understood.

Electrostatic interaction is one of the major intermolecular interactions in molecular assembly, especially in the charged amphiphile system. Previous studies[20, 21] on binary mixtures of cationic and anionic amphiphiles have shown that electrostatic attraction between could induce the coassembly of amphiphiles into bilayer membranes. In this research thesis, we continue to focus on the assembly from charged amphiphilic molecules, but with aim to develop model systems where the intermolecular electrostatic interactions can be tuned systematically by facile changes in external parameters such as pH, salt concentration, and molecular compositions. Structural transformations over \AA to μm length scales are observed as a function of the above-mentioned external parameters for different amphiphilic molecules. These studies demonstrate how electrostatic interactions determine the self-assembly features from the molecular packing

level (\AA scale) to the overall assembly morphology (μm scale). An overview of the thesis is presented in Chapter 2.

Chapter 2. Overview

Amphiphiles have the ability to self-assemble into a large variety of structures including micelles, bilayers and fibers. Furthermore, structures like bilayer membrane can also present different morphologies such as vesicles, twisted ribbons[22, 23], helical ribbons[24, 25], nanotubes[26], etc. Therefore, the characterization methods are extremely critical in probing the structural variation at different length scales. The primary methods such as small- and wide-angle X-ray scattering (SAXS/WAXS) and transmission electron microscopy (TEM) are discussed in Chapter 3. In Chapter 4, we explored the self-assembly behavior of a modular series of charged peptide amphiphiles (PA): $C_{16}\text{-K}_n$ ($n = 1, 2, 3$ and 4). *In situ* SAXS/WAXS and cryo-TEM are combined to characterize the assembly structure from nanoscale molecular arrangement to the mesoscopic morphology. Specifically, we found the structural transformation from unaggregated state, to spherical micelles, to cylindrical micelles, to nanoribbons and finally to microtubules, as the charge and headgroup size is reduced. The complete phase diagram is also constructed for the equilibrium assembly structure as a function of headgroup size and solution pH, which provides detailed insights into the coupling of the steric and electrostatic interactions in driving the PA assembly.

The assembly structure of $C_{16}\text{K}_1$ peptide amphiphile is specifically discussed in Chapter 5. Chapter 4 has shown that $C_{16}\text{K}_1$ can self-assemble into bilayer with nanoribbon morphology. Instead of varying pH, here the salt concentration, or the ionic strength (μ), is systematically changed to screen the electrostatic interaction. We found that with increasing ionic strength, high

aspect ratio ($>10:1$) nanoribbons transform into low aspect ratio sheets before rolling onto themselves to form cochleates. This transformation is accompanied by a decrease of crystallinity in the molecular packing of the lipid tail based on WAXS result. Furthermore, the interlayer spacing (D) in the cochleate structure is directly proportional to the solution Debye length (λ_D): $D \propto \lambda_D \propto \mu^{-1/2}$, and could be tuned over a range: 40 to 10 nm by increasing the ionic strength. This feature could facilitate the controlled encapsulation and release in the drug delivery system. Theoretical models show that the interplay between electrostatics, van der Waals' elastic and interfacial energies govern the nanoribbon to cochleate transformation. In particular, the initial increase in the nanoribbon aspect ratio is driven by a competition between the electrostatic and interfacial edge energies. The cochleate transformation is due to the intrinsic curvature of the membrane, and finally the equilibrium interlayer spacing inside the cochleate results from the balance of interlayer repulsive electrostatic energy and attractive van der Waals interactions.

In addition to peptide amphiphile systems, cationic phospholipid bilayers are also an attractive model system because of their ability to mimic natural cellular membranes. In Chapter 6, we seek to investigate the role of electrostatic interactions in driving the bilayer assembly by looking at the gel (solid-like) to fluid (liquid-like) phase transformation temperatures of binary mixtures of phospholipid molecules that have charges of +1, 0, or -1. Gel to fluid phase transformation temperature can be determined from the temperature dependent WAXS studies. Therefore, the phase diagram of binary mixture of DMTAP (+1)/DMPS (-1) and DMTAP (+1)/DMPC (0) phospholipid can be constructed by repeating temperature dependent WAXS studies at different lipid compositions. The diagram indicates the highest melting temperature at

a 1:1 mixture when the headgroup electrostatic interaction is the strongest. Additionally, 2D hexagonal lattice parameters in the gel phase membrane can also be adjusted through precise control of temperature and lipid composition.

Chapter 7 provides a summary of this thesis and some possible future works. The first part describes an experiment to test the particle encapsulation ability of the cochleate structure. The second part proposes the possible origin of intrinsic curvature observed in cochleate structure, and also the experimental methods to verify the hypothesis.

Chapter 3. Characterization Methods

1. Small/Wide Angle X-ray Scattering (SAXS)

SAXS is a technique that collects the scattered intensity pattern at small scattering angles. SAXS can probe relatively large structural features with length scales ranging from 1nm to 200 nm[27]. Therefore, it is very useful in measuring size and shape of the self-assembly aggregates. The scattering intensity $I(\mathbf{q})$ of particles in solution is given by

$$I(\mathbf{q}) = |A(\mathbf{q})|^2 S(\mathbf{q}) \quad (2.1)$$

In this equation, $A(\mathbf{q})$ is the form factor, i.e. scattering from a single particle which has been corrected for the electron density contrast between the particle and the solvent and $S(\mathbf{q})$ is the structure factor determined by the interparticle correlations such as local order or crystallization of colloidal particles. \mathbf{q} the scattering vector is the momentum transfer or the difference of the incident and scattered wave vectors ($\mathbf{q}=\mathbf{K}_f-\mathbf{K}_i$). The magnitude of \mathbf{q} can be defined as

$$q = \frac{4\pi\sin(\theta)}{\lambda} \quad (2.2)$$

θ is half of the scattering angle 2θ , and λ is the wavelength of the incident and scattered X-ray beams.

In dilute systems, each particle can be regarded as an independent scatterer, which means there is no interparticle correlations, $S(\mathbf{q})$ is N , the number of particles in the X-ray footprint.

Then the scattered intensity $I(\mathbf{q})$ only depends on particle form factor $A(\mathbf{q})$ (apart from a constant), which provides information on the electron density distribution within the particles and the concentration of the particles. The form factor can be calculated by the Fourier transform of the spatial electron density distribution of the particle ρ .

$$A(\mathbf{q}) = \int_V (\rho(\mathbf{r}) - \rho_s) e^{-i\mathbf{q}\mathbf{r}} dV \quad (2.3)$$

Table 3.1 shows form factors for some common morphologies. Therefore, if the sample morphology is known, we are able to determine the dimension of the particles by simply fitting the intensity $I(\mathbf{q})$ to these form factors. Otherwise, we can extract the particle size and shape information from intensity $I(\mathbf{q})$ by Guinier's law and Porod's law described below.

Guinier's law is used to approximate $I(\mathbf{q})$ at relatively smaller \mathbf{q} region ($q \cdot R_g < 1$), where equation (2.1) can be expressed as a following exponential function

$$I(\mathbf{q}) \propto e^{-q^2 R_g^2 / 3} \quad (2.4)$$

R_g is the radius of gyration of the particle defined as the electron density weighted root mean square distance of the particle's parts from its center of gravity, which can determine the approximate size of the particles.

Porod's law applies to higher \mathbf{q} region ($q \cdot R_g \gg 1$). In the Porod region, $I(\mathbf{q})$ can be approximated by the power law

$$I(\mathbf{q}) \propto q^{-\alpha} \quad (2.5)$$

The exponent α defines the dimensionality of the particles: 1 for one-dimensional objects, 2 for two-dimensional objects and 4 for three-dimensional objects. Figure 3.1 is an example of scattering intensity from dilute monodisperse spheres, showing the corresponding Guinier's and Porod's regions.

Table 3.1. Common form factors of particular shapes such as spheres, core-shell spheres, ellipsoids, cylinders, and disks.[28]

Morphologies	P(q)	Morphologies
Spheres (radius :R)	$\frac{9}{(qR)^6}[\sin(qR) - qR \cdot \cos(qR)]^2 = A_{\text{sph}}^2(qR)$	
Spherical shells (outer radius: R ₁ inner radius: R ₂)	$\frac{[R_1^3 \cdot A_{\text{sph}}(qR_1) - R_2^3 \cdot A_{\text{sph}}(qR_2)]^2}{(R_1^3 - R_2^3)^2}$	
Triaxial ellipsoids (semiaxes: a,b,c)	$\int_0^1 \int_0^1 A_{\text{sph}}^2[q \sqrt{a^2 \cos^2(\pi x/2) + b^2 \sin^2(\pi x/2)(1-y^2) + c^2 y^2}] dx dy$	
Cylinders (radius: R length: L)	$4 \int_0^1 \frac{J_1^2[qR\sqrt{1-x^2}]}{[qR\sqrt{1-x^2}]^2} \frac{\sin^2(qLx/2)}{(qLx/2)^2} dx$ <i>J₁(x) is the first kind Bessel function of order 1</i>	
Thin disk (radius: R)	By setting L = 0 $\frac{2 - J_1(2qR)/qR}{q^2 R^2}$	
Long rod (length: L)	By setting R = 0 $\frac{2}{qL} \int_0^{qL} \frac{\sin(t)}{t} dt - \frac{\sin^2(qL/2)}{(qL/2)^2}$	

"Structure Analysis by Small Angle X-Ray and Neutron Scattering" L. A. Feigen and D. I. Svergun

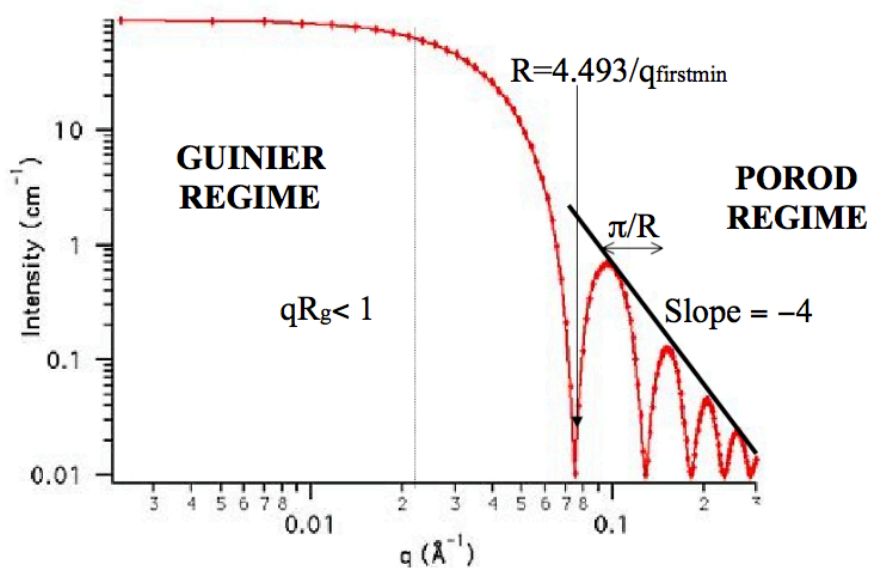


Figure 3.1. Theoretical SAXS intensity profile of dilute monodisperse spheres, showing Guinier and Porod regime of the curve.

WAXS is sensitive to the structures of length scale smaller than 1 nm; therefore it is useful for studying crystalline molecular packing inside the assembly. For example, WAXS diffraction peaks can be used to determine the lattice structures and intermolecular spacing.

SAXS/WAXS intensities ($0.05 \text{ nm}^{-1} < q < 30 \text{ nm}^{-1}$) were collected simultaneously by three CCD detectors at the 5ID-D undulator beamline of the Advanced Photon Source at Argonne National Laboratory. The sample solutions were injected through a capillary tube flow-cell (1.5 mm, quartz) at 2-5 mm/sec to reduce radiation damage. The capillary was surrounded by vacuum to avoid air scattering. A fast shutter was used such that the samples are exposed to X-rays only during the data collection time (5-10 s for each measurement). For improving statistics, 5-10

measurements were made per sample. All scattering data were collected at an incident photon energy of 15.00 keV (wavelength $\lambda = 0.827 \text{ \AA}$). For background subtraction and for calibrating the intensities to the absolute scale (differential scattering cross-section per unit volume), SAXS/WAXS patterns were also collected from the empty capillary and from the capillary containing pure water before measurements on every sample. The 2D SAXS/WAXS patterns were converted into 1D intensity patterns, $I(q)$, by azimuthal integration while taking into account the polarization, solid-angle, flat field and transmission corrections. The data were also normalized for the scan time. For absolute intensity calibration, the normalized and corrected scattered intensity profiles from pure water (obtained as the difference of the scattering from capillary filled with water and the empty capillary) were fitted to straight lines. The intercept of these line was set to 0.0165 cm^{-1} , which is the expected scattered intensity from water at $q = 0$ on the absolute scale and at $T = 25 \text{ }^\circ\text{C}$. [29] The data from the corresponding samples were thereafter scaled accordingly.

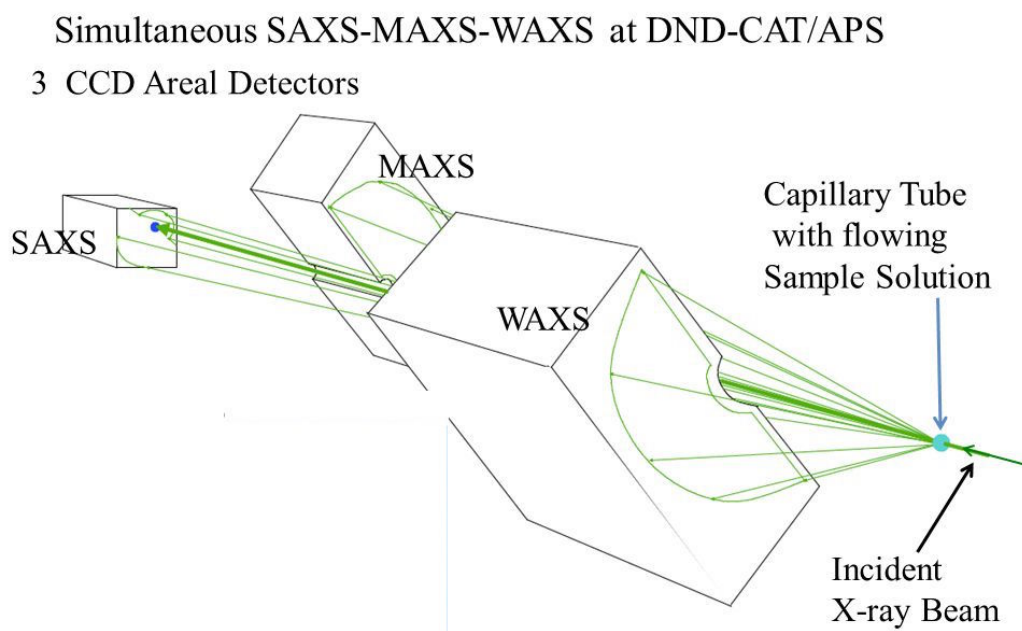


Figure 3.2. Schematic of the SAXS/MAXS/WAXS detector system, SAXS, MAXS and WAXS patterns are collected simultaneously by three separate CCD X-ray areal detectors.

2. Grazing-Incidence Wide Angle X-ray Scattering (GIWAXS)

Grazing Incidence Wide Angle X-ray Scattering (GIWAXS) is used to determine the 2D crystalline structure of flat bilayer membranes deposited on the solid substrate. Compared with solution WAXS described above, GIWAXS is highly specialized in studying film structures on the surface, and it allows observation of higher order diffraction peaks, which may have been smeared out due to the intrinsic powder averaging in solution scattering, thereby yielding higher spatial resolution for molecular packing. This technique uses very small incident angles (usually close to the critical angle of the sample) for the incident X-ray beam onto the surface, so the

diffraction is surface sensitive. In this thesis, the bilayer membrane samples are prepared by drop casting 30 μL aqueous solution with bilayer assemblies, onto a $1\text{cm} \times 3\text{cm}$ piranha pretreated silicon (001) substrates with a thin native oxide layer. GIWAXS measurement was conducted on Rigaku SMAX3000/Molecular Metrology ($\text{Cu K}\alpha$ source) using a phosphor image plate to collect the scattering signal. After exposing the sample under X-ray for 2h, phosphor image plate was scanned by GE Healthcare Typhoon 9400 to get the X-ray scattering pattern. Nika SAS 2D macro in Igor Pro was used to transform the raw scattering pattern into reciprocal space.

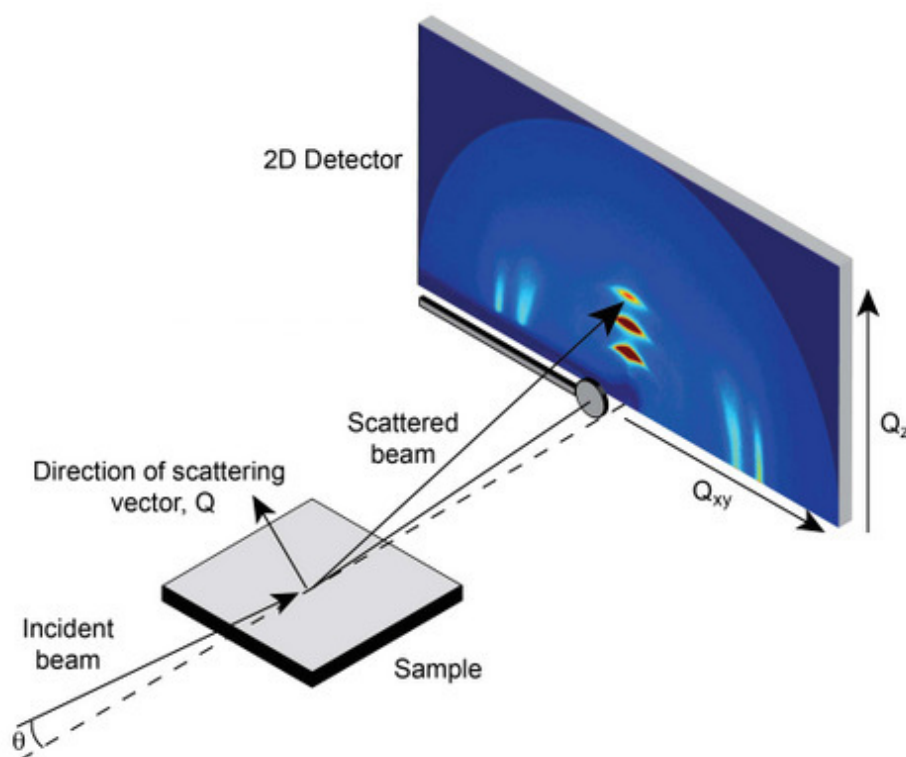


Figure 3.3 Schematic of GIWAXS experimental geometry. The angle of incidence, θ , is close to the critical angle of the sample. A 2D detector (or phosphor image plate) is used to simultaneously collect the scattered X-rays.

3. Transmission Electron Microscopy (TEM)

Cryogenic transmission electron microscopy (cryo-TEM)[30] and conventional transmission electron microscopy (TEM) are the techniques for imaging self-assembly structures such as vesicles, ribbons and fibers. Cryo-TEM images the frozen sample solution directly and therefore allows us to see the structures in their native environment. Conventional TEM images the dry samples that have been stained by heavy metal element and hence produce images with relatively high contrast.

Cryogenic transmission electron microscopy (cryo-TEM) imaging is performed on a HT7700 microscope, operating at 80 kV. A small droplet of the solution (5 μ L) is placed on a holey carbon film supported on a TEM copper grid. The grid is held by a tweezer mounted on a Vitrobot VI equipped with a controlled humidity and temperature environment. The specimen is blotted and plunged into a liquid ethane reservoir cooled by liquid nitrogen. The vitrified samples are transferred to a Gatan 626 cryo-holder through a cryo-transfer stage cooled by liquid nitrogen. During observation of the vitrified samples, the cryo-holder temperature is maintained below -180 °C. The images are recorded with a CCD camera.

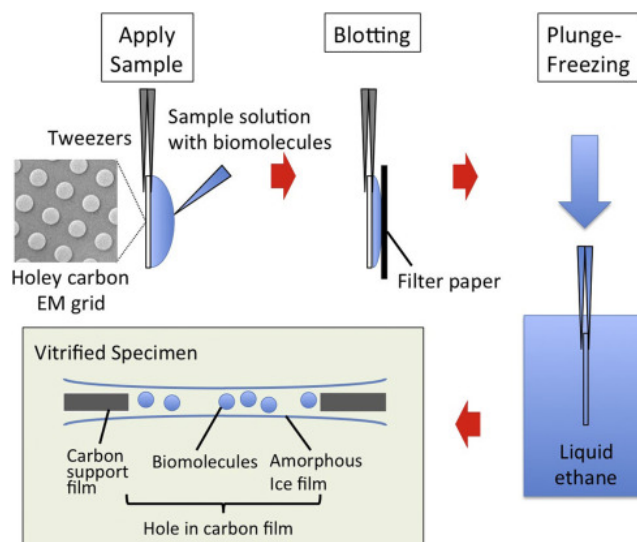


Figure 3.4. Cryo-TEM specimen preparation by plunge-freezing. Aqueous sample solution is applied onto glow-discharged (hydrophilic) holey carbon film supported by EM grid. Excess solution is removed with filter paper from one or both sides. Blotted grid is rapidly plunged into a cryogen precooled at liquid nitrogen temperature. Biomolecules embedded in thin amorphous ice film are observed in cryo-electron microscope.

Conventional transmission electron microscopy imaging is also performed on a HT7700 microscope, operating at 100kV. 1% Uranyl acetate ($\text{UO}_2(\text{CH}_3\text{COO})_2 \cdot 2\text{H}_2\text{O}$) solution is used as heavy metal stain for the sample to increase image contrast. A small droplet of the sample solution (10 μL) is first placed on a TEM grid, and blotted by kimwipes after 3-5 min. Then a droplet of uranyl acetate solution (10 μL) is added on the grid, and blotted by kimwipes after 3-5 min. The staining process can be repeated depending on the required imaging contrast of the sample. The grid is dried under ambient conditions for 2 h before transferring to the microscope.

The images are recorded with a CCD camera.

4. Atomic Force Microscopy

Atomic force microscopy is typically used to image the surface structures at solid-air interface. In this thesis, we used ScanAsyst in Bruker Bioscope AFM to image the membrane structure at solid-liquid interface, which allows the structures to be studied in their solution state. ScanAsyst is a PeakForce Tapping mode based image optimization technique that can create high-resolution AFM images with very low imaging forces. Therefore this mode is ideal for imaging biological structures.

The sample is prepared by dropping 25 μL solution onto piranha-treated Si substrate. The Si substrate is taped onto a petri dish that can be held stable by the AFM sample stage. Scanasyst fluid+ AFM probe is used for the high-resolution imaging in fluid. The AFM probe is first placed on Easy-align system to align the probe by centering the reflected laser beam on the photodetector. Then the probe is manually controlled to approach the sample surface before using the automatic engagement to find the solid-liquid interface. The contrasts of AFM images shown in this thesis include height contrast and peakforce error contrast. Image with height contrast shows the height of the surface features. Peakforce error contrast originates from the feedback loop in the PeakForce Tapping mode, and corresponds to the difference between instantaneous peakforce of probe oscillation and the peakforce setpoint. This contrast could highlight the changes in surface height and hence produce images with better surface topography.

5. Dynamic Light Scattering (DLS)

Dynamic light scattering (DLS) is a technique in physics that can be used to determine the size distribution profile of small particles in solution. Compared to Static Light Scattering, DLS utilize the temporal fluctuations of scattering intensity at a fixed scattering angle to extract the size distribution of suspended particles in solution. Specifically, Brownian motions of particles result in the intensity fluctuation of scattered photons, which can be recorded and analyzed through auto-correlation function. In the time domain analysis, the autocorrelation function usually decays starting from zero delay time, and faster dynamics due to smaller particles lead to faster decay of the autocorrelation function $g(\tau)$ (Figure 3.5). The decay rate of the autocorrelation function has the linear correlation with the diffusion coefficient D_t of the particle in solution (Equation 2.6), which is often used to calculate the hydrodynamic radius R of spherical particles through the Stokes-Einstein equation (Equation 2.7).

$$g(\tau) = g_0 \exp(-D_t q^2 \tau) \quad (2.6)$$

$$D_t = \frac{k_B T}{6\pi\eta R} \quad (2.7)$$

Here the q is scattering vector typically fixed in DLS experiment. τ is time delay between two scattered intensity measurements. In Stokes-Einstein equation, T is absolute temperature and η represents the solution viscosity.

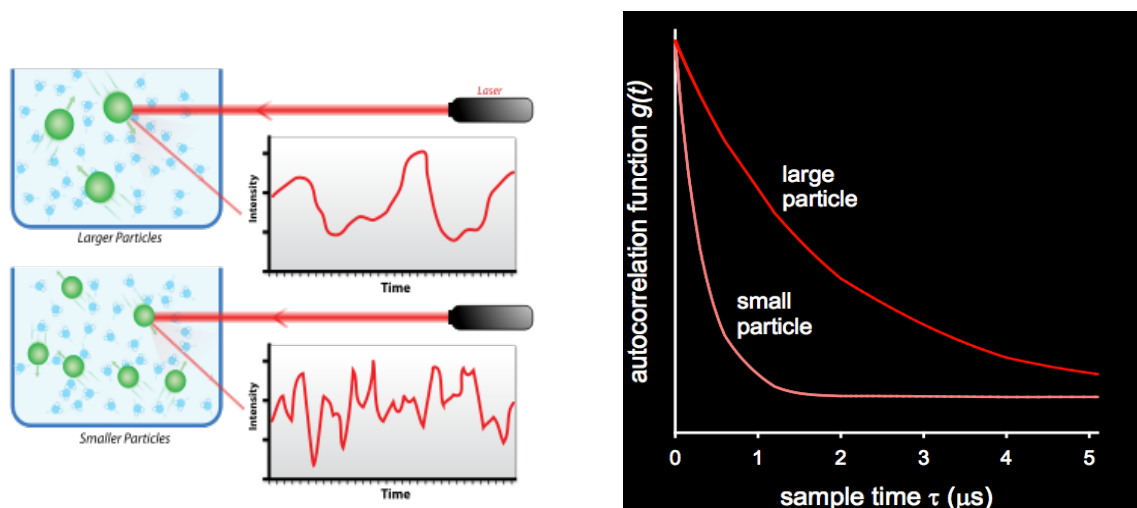


Figure 3.5. Schematic representation shows the principle of size measurement in Dynamic Light Scattering. The intensity fluctuation due to the Brownian motion is more frequent for smaller particles (left image), which leads to faster decay of autocorrelation function. The decay rate can be used to calculate the particle size.

In this thesis, dynamic light scattering is used for studying the size of lipid bilayer vesicles, since the bilayer vesicles are typically in spherical shape that satisfies the premise of Stoke-Einstein equation. The experiment is conducted on a Zetasizer Nano instrument. The light source of the instrument is He-Ne laser with wavelength of 633 nm and the scattered intensity fluctuation is detected at 173° backscattering angle. This backscatter detection reduces the effect of multiple scattering as well as the large particle scattering, both of which usually happens at scattering in the forward direction. The prepared solution is filled into a specific polystyrene cuvette and the temperature in the sample chamber is stabilized for at least 5 min before the

measurement. For improving the statistics, 10 identical runs are performed for each measurement with total duration of 50 s. The measurement results are presented in a report page with information including Z-average size, number-averaged size, size distribution, polydispersity, etc.

6. Differential Scanning Calorimetry (DSC)

Differential Scanning Calorimetry (DSC) is used to study the gel-to-fluid phase transition in bilayer assemblies, especially the phase transition temperature. DSC is a thermoanalytical technique in which the difference in the heat capacity of the sample and reference is measured as function of temperature. The reference is typically the blank buffer solution and has well-defined heat capacity over the range of temperatures to be scanned. Therefore, when the temperature approaches the phase transition temperature of bilayer sample, the DSC scan produces a peak due to the significant increase in the heat absorbance or emission of the bilayer sample. Through the DSC peak analysis, we can extract phase transition temperatures, transition enthalpies, as well as the phase transition types.

DSC experiments are performed on a MicroCal (GE Healthcare) differential scanning calorimeter. It has non-reactive Tantalum 61TM cells with volume around 0.5 mL and the operating temperature range could be between -10°C to 130°C. Prior to each experiment, the sample and reference cells are thoroughly cleaned with warm DI water, and the solution samples are degassed for 5 min to remove bubbles. A blank test to measure instrument background is also conducted by loading the buffer solution into both sample and reference cells. For each DSC

scan, the scan rate is fixed to 30 °C per hour and the scan range is selected based on the phase transition temperature. The collected DSC curves shown in this thesis are background subtracted, calibrated and further analyzed by Origin macros for DSC.

Chapter 4. Polymorphism of Peptide Amphiphile Assembly Induced by Headgroup Charge and Size Regulation

4.1. Introduction

Precise control of the supramolecular architecture in aqueous solution is integral to molecular self-assembly applications and biological processes. In particular, self-assembly of peptide amphiphile (PA) can exhibit a large variety of nanostructures such as cylindrical fibers[31-33], nanoribbons[34] and even the closed vesicle structures[20]. Most PA molecules contain the biocompatible amino acid sequences[10] and they have been frequently used as building block for creating self-assembly structures for a broad range of biological applications. Therefore, it is of great significance to have better structural control of the PA self-assembly with properties tailored for the desired purposes. However, the varying structures of PA assembly could arise from interplay of several different intermolecular interactions, including van der Waals, hydrogen bonding, electrostatic interaction, steric effect, and π - π stacking. For example, PA with different amino acid sequences have shown that the coupling of hydrogen bonding, π - π stacking and van der Waals attraction could induce a variety of bilayer membrane morphologies.[24, 35] However, it remains highly challenging to experimentally regulate those intermolecular interactions, and also detailed physical explanations of the equilibrium self-assembly structure are often lacking in those studies.

Electrostatic interaction, unlike other interactions, can be experimentally tuned by the solution pH and salt concentration. The solution pH controls the charge of the amino acids in the headgroup, and the counterions from the salt screen the intermolecular electrostatic interactions. Theoretical investigations have probed the dependence of PA assembly structures on the relative strengths of the electrostatic interactions.[36, 37] For example, a combined Monte Carlo, molecular dynamics (MD) simulation, and transmission electron microscopy (TEM) study on the assembly of a bioactive PA showed that PAs assemble into spherical or cylindrical micelle structure only if the electrostatic repulsion between the headgroup is weak. This demonstrates the critical role of electrostatic interactions in the PA assembly. Although the effects of headgroup charge have also been experimentally studied in PA assembly, electrostatic interactions are often coupled with intermolecular hydrogen bonding interactions in those systems.[38-41] To determine purely the effects of interheadgroup electrostatic interactions, here we completely eliminated the hydrogen bond forming block.

In this chapter, we will focus on the self-assembly of a modular series of peptide amphiphiles: $C_{16}K_4$, $C_{16}K_3$, $C_{16}K_2$, and $C_{16}K_1$, which carry different number of ionizable lysine residues conjugated to the same C_{16} -alkyl tail (Figure 4.1). Because the headgroup charge originates from pH-sensitive primary amine, it can be tuned by pH in a continuous manner. In addition, geometric size of the headgroup should be related to the number of lysine group sequences. SAXS and TEM are used for detecting self-assembly structures from 10 to 1000 nm length scale, and the results exhibit a large structural diversity transitioning from unaggregated state, to spherical micelles, to cylindrical micelles, to nanoribbons and finally to microtubules, as the electrostatic interaction and steric interaction is weakened. WAXS results reveal the Å-scale

intermolecular packing within the 2D bilayer assemblies, and also give hints on the molecular conformations inside the 2D lattice. Since the structural transformation is driven simply by headgroup charge and size regulation, this model system allows us to visualize the correlation between equilibrium self-assembly structures and the intermolecular forces, and it also opens the gateway of constructing supramolecular nanostructures with precise structural control from simple unary molecular system.

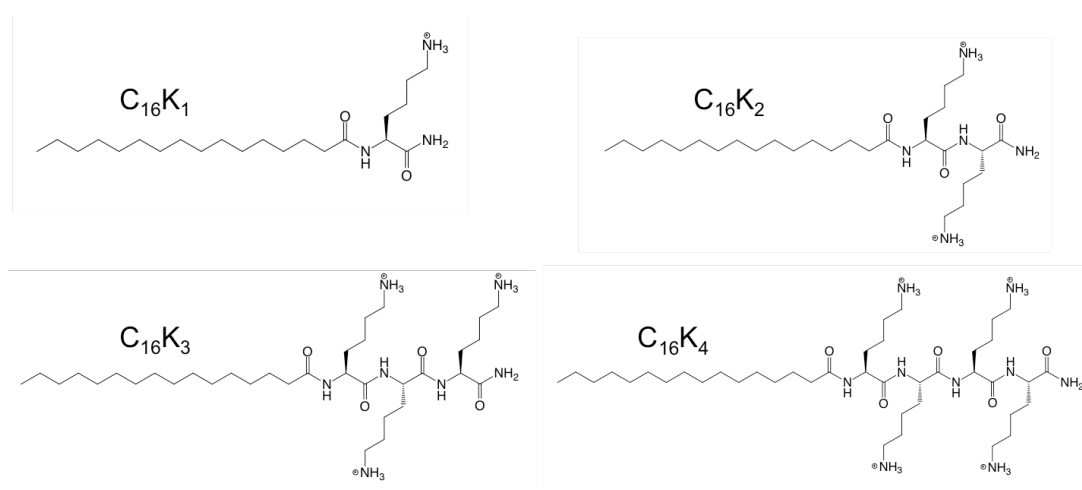


Figure 4.1. Molecular structures of positively charged C₁₆K₄, C₁₆K₃, C₁₆K₂, and C₁₆K₁ peptide amphiphiles

4.2. Materials and Methods

4.2.1. Sample Preparation

Peptides were synthesized in the Peptide Synthesis Core at the Simpson Querrey Institute for BioNanotechnology of Northwestern University using a CEM Liberty microwave-assisted

peptide synthesizer. Standard fluoren-9-ylmethoxycarbonyl (Fmoc) solid-phase peptide synthesis was used with rink amide MBHA resin (100-200 mesh). For each coupling, 5 equivalents of Fmoc-protected amino acid (or palmitic acid) in DMF was added with 5 equivalents of N,N,N',N'-tetramethyl-O-(1H-benzotriazol-1-yl)uronium hexafluorophosphate (HBTU) in DMF and 10 equiv of N,N-diisopropylethylamine (DIPEA) in NMP. Fmoc removal was accomplished using a solution of 20% piperidine in DMF and 0.1 M 1-hydroxybenzotriazole (HOBt). Peptides were cleaved from the resin using a mixture of 95% trifluoroacetic acid (TFA), 2.5% water, and 2.5% triisopropylsilane for 3 h. Crude peptide was precipitated from this solution using cold diethyl ether. Purification was carried out on a Waters Prep 150 HPLC using a water/acetonitrile with 0.1% TFA solvent system and a Phenomenex Kinetex 30x150 mm C18 column. Eluting fractions were analyzed by ESI-MS using an Agilent 6520 Q-TOF LCMS before lyophilization and purity analysis by the same Agilent LCMS (water/acetonitrile with 0.1% formic acid solvent system and Phenomenex Proteo 100 x 1 mm column).

4.2.2. Characterization Methods

To monitor the assembly structure of $C_{16}K_n$ as a function of solution pH, $C_{16}K_n$ molecules with trifluoroacetate counterions (CF_3COO^-) were dissolved in aqueous solution at 4 mM concentration and the solution pH is adjusted with aqueous NaOH. SAXS/WAXS and Cryogenic transmission electron microscopy (Cryo-TEM) imaging are then used to study the structure of the PA assemblies in aqueous solution. Detailed experimental setups of SAXS and cryo-TEM are discussed in Chapter 3. Titration experiments of $C_{16}K_n$ are conducted to determine the molecular charge vs. pH correlation. 5 ml solutions of 4 mM $C_{16}K_n$ are each titrated with a solution of 100 mM NaOH. The PA and the NaOH solutions are both freshly prepared in ultrapure water

(resistivity = 18.2 M Ω .cm). The pH is measured using an Oakton pH 6 Acorn Series meter equipped with a PHR-146 microelectrode, which is calibrated at pH 4, 7 and 10 using buffer solutions, prior to titration experiments.

4.2.3. Monte-Carlo Simulations:

The effects of charge correlations on the ionization of C₁₆K₂ headgroup as a function of pH were examined by Monte Carlo simulations, which were performed by Honghao Li in Professor Monica Olvera de la Cruz's group.

We model the effects of electrostatic interactions by a lattice model introduced by Netz[42], and used by previous studies[20]. As a simplification, we choose a square lattice for C₁₆K₂ molecules. Two nearby sites separated by 0.5 nm are connected to represent a single molecule. Each site can be either in state $n = 0$ (neutral) or $n = 1$ (dissociated). The energy is measured in terms of $k_B T$, and the Bjerrum length $l_B = \frac{e^2}{4\pi\epsilon_0\epsilon_r k_B T}$ is introduced for simplicity, where ϵ_r is the relative permittivity and the e is the unit charge. The Hamiltonian used in the simulations is given by

$$\frac{H}{k_B T} = \frac{\mu}{k_B T} \sum_i n_i + \frac{1}{2} \sum_{i \neq j} l_B \frac{e^{-\kappa r_{ij}}}{r_{ij}}$$

(3.1) where $n_i = 0$ or 1 is the dissociation state of site i , and κ is the inverse of the Debye screening length which is controlled by the salt concentration. In order to model actual experiment, we set the Bjerrum length $l_B = 0.7$ nm for aqueous environment and $l_B = 1.4$ nm for water-air interface. The chemical potential is given by[43]

$$\frac{\mu}{k_B T} = -\ln 10(pH - pK_a) \quad (3.2)$$

A typical simulation consists of 10,000 equilibration steps and 100,000 measurement sweeps, where a sweep is defined as an attempted flip of each site.

4.3. Results and Discussion

Figure 4.2a shows the measured titration curves for 5 mL 4 mM C₁₆K_n with 100 mM NaOH solution. All the molecules are soluble over the studied pH range. We can observe that the titration curves for all C₁₆K_n molecules exhibit only one buffer stage, indicating that the fully ionized C₁₆K_n behave as monoprotic acid regardless of the number of lysines (K) on the headgroup. Therefore, we are able to use Henderson-Hasselbach equation to derive the charge vs. pH curves for C₁₆K_n. The headgroup charge α for the monoprotic acid can be formulated as

$$\alpha = \frac{1}{1 + 10^{pH - pK_a}} \quad (3.3)$$

The pK_a in this equation can be determined from the center positions on the buffer stages of the titration curves, the pK_a for C₁₆K₁, C₁₆K₂, C₁₆K₃ and C₁₆K₄ are found to be 7.4, 8.3, 9.1, and 9.7 respectively. We notice that the pK_a for all four molecules are lower than the pK_a ~ 10.0 expected for isolated lysine. This implies that in C₁₆K_n assemblies, the ionization tendency of lysines is reduced, because any arrangement of like-charged molecules in close proximity increases the overall electrostatic potential energy of the ionized state. This can also be proven by Monte-Carlo simulation of C₁₆K₂ assembly showing a theoretical deionization curve with pKa

~ 8.2 (Figure 4.2c). Figure 4.2b shows the averaged headgroup charge vs. solution pH curves for $C_{16}K_1$, $C_{16}K_2$, $C_{16}K_3$ and $C_{16}K_4$ peptide amphiphiles from Henderson-Hasselbach equation (eq. 3.3). At low pH, the lysine groups are fully ionized and further increase in pH leads to a monotonic decrease in the headgroup charge for all four peptide amphiphiles. The significant decrease in headgroup charge occurs around the pK_a of each $C_{16}K_n$ molecule, therefore we hypothesized that nano- or mesoscopic structural transformations would also occur at $pH \sim pK_a$. Following studies will focus on the structural transformation around $pH \sim pK_a$, and explore the correlations between the electrostatic repulsion and self-assembly morphologies for different $C_{16}K_n$ molecules.

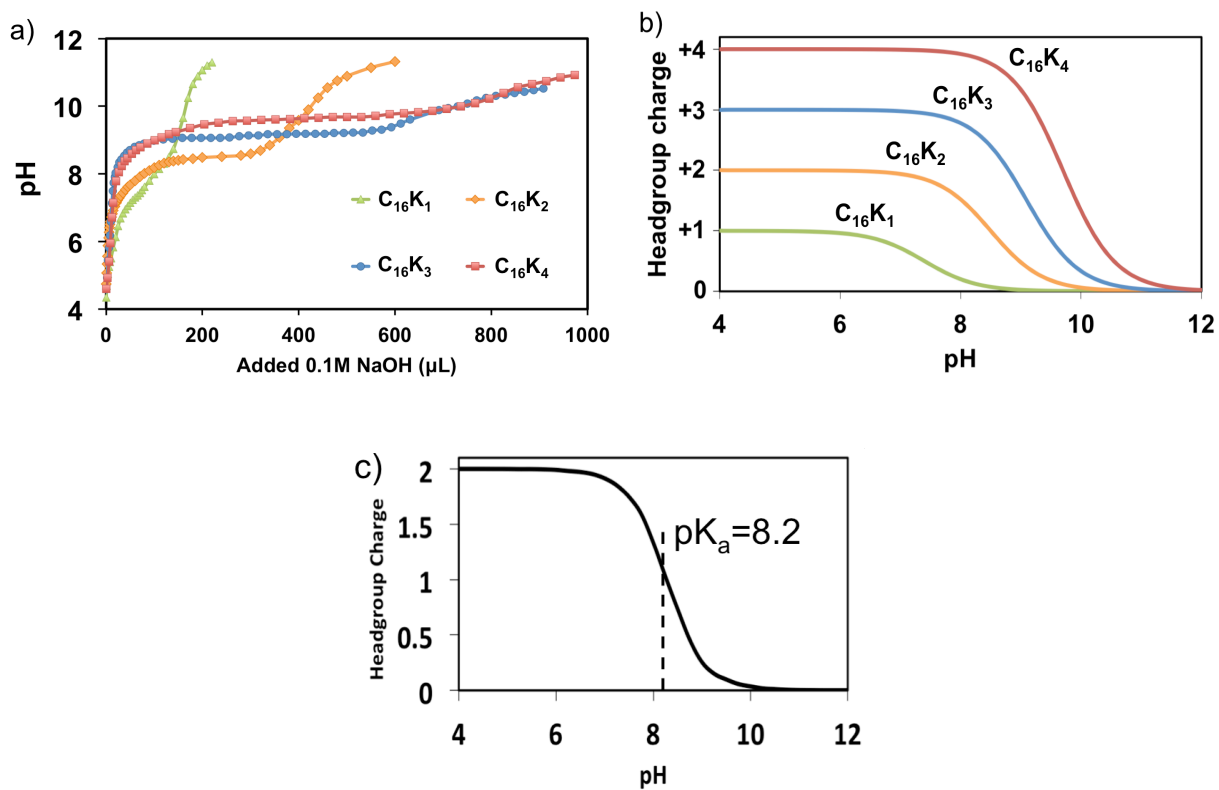


Figure 4.2. (a) $C_{16}K_n$ titration curves showing how pH changes as function of the volume of NaOH added. All $C_{16}K_n$ exhibit single buffer stage. (b) Averaged $C_{16}K_n$ headgroup charge as a function of pH obtained through Henderson-Hasselbach equation of monoprotic acid (eq. 3.3). pK_a is determined from the titration curves. (c) Averaged $C_{16}K_2$ headgroup charge as a function of pH in standard water environment obtained by Monte Carlo theoretical simulation, showing deprotonation around pH 8.2.

Figure 4.3 shows the background subtracted SAXS/WAXS intensities as function of the scattering vector magnitude $q = 4\pi\sin \theta/\lambda$. Here, λ is the X-ray wavelength, and 2θ is the scattering angle. Solid black curves are the best SAXS fits using the models described in Table 4.1. Some general changes in the intensity profiles with varying pH and headgroup size can be discerned without detailed analysis. First, for $q < 0.3 \text{ nm}^{-1}$, i.e., within the SAXS regime, the I vs q slope becomes steeper for higher pH and smaller headgroup. The changes in the slope are related to the changes in the overall morphology of the assembly based on Porod's law (See Chapter 3). Second, no intensity oscillations (i.e., scattering features) are observed at the condition close to the lowest pH and largest headgroup, which corresponds to the state where no assembly is formed. In addition, the appearance of diffraction peaks at WAXS regime ($10 < q < 20 \text{ nm}^{-1}$) indicates the formation of crystalline ordering in the $C_{16}K_n$ molecular packing. Detailed analyses are described in the following.

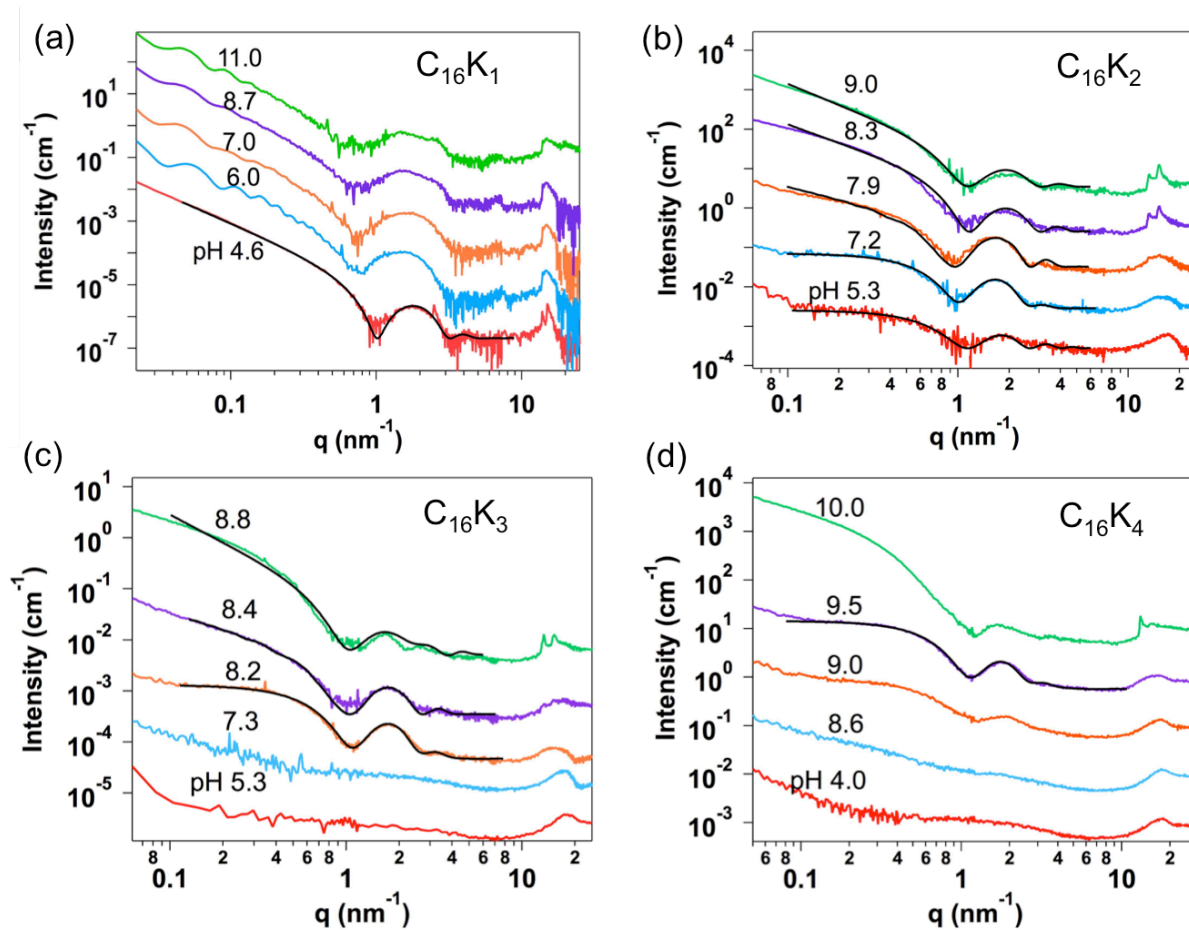
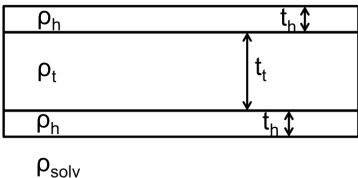
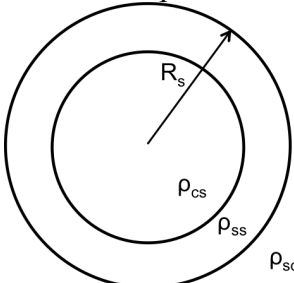
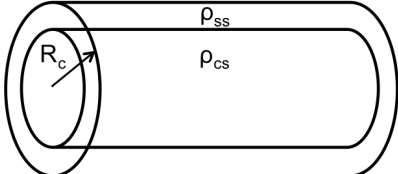
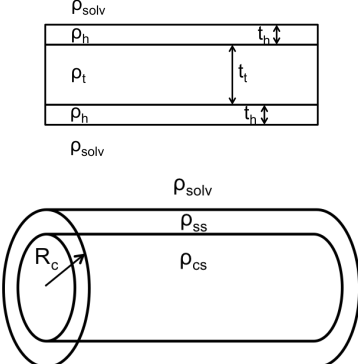


Figure 4.3. In situ small- and wide-angle X-ray scattering data showing the background subtracted scattered intensity profile for $C_{16}K_n$ as a function of solution pH. The data sets are offset vertically for clarity. The solid black curves are the best fits over the SAXS region ($0.1 < q < 8 \text{ nm}^{-1}$) using different models (Table 4.1).

Table 4.1. Fitting models used for $C_{16}K_n$ SAXS fittings

SAXS data	Models
$C_{16}K_1$ at pH 4.6	<p>Symmetric bilayer model</p> 
$C_{16}K_2$ at pH 5.3 and 7.2 $C_{16}K_3$ at pH 8.2 $C_{16}K_4$ at pH 9.5	<p>Core-shell sphere model</p> 
$C_{16}K_2$ at pH 7.9 $C_{16}K_3$ at pH 8.4	<p>Core-shell cylinder model</p> 
$C_{16}K_2$ at pH 8.3 and 9 $C_{16}K_3$ at pH 8.8 $C_{16}K_4$ at pH 10	<p>Symmetric bilayer + Core-shell cylinder</p> 

First we start with the structural transformations in the molecular assembly of C₁₆K₁, which has the smallest ionizable headgroup. When no NaOH is added and the molecule remains fully charged (pH 4.6), SAXS/WAXS intensity profile shows that the SAXS intensity (*I*) falls off as q^{-2} in the low *q* region. The exponent of -2 at low *q* is indicative of 2D structure, which is supported by the cryo-TEM image showing a planar ribbon structure (Figure 4.4). Furthermore, the SAXS *I* vs *q* profile could be reasonably fitted with a simplified symmetric bilayer model, and WAXS region also shows several diffraction peaks. These strongly indicate the formation of crystalline planar bilayer. For the SAXS fitting, the electron density of the tail region ρ_t was constrained to be 95% of the electron density of pure water ($\rho_t = 320 \text{ e}^-/\text{nm}^3$), corresponding to the crystalline packing of the alkyl tails.[44] Fitting results reveals that the electron density of the headgroup region ρ_h is $386_{-0}^{+61} \text{ e}^-/\text{nm}^3$, and total thickness of bilayer is $4.0_{-0.4}^{+0.0} \text{ nm}$. This value is lower than the length of two fully extended C₁₆K₁ molecules ($2 \times 2.7 \text{ nm}$), which indicate that the two leaflets of bilayer are strongly interdigitated. Detailed SAXS analysis on C₁₆K₁ bilayer will also be discussed in Chapter 5. In Figure 4.3a, we observe that increasing pH does not change the -2 exponent at low *q*, but it leads to a number of oscillations at very low *q*, implying the formation of large and monodisperse object. Cryo-TEM image (Figure 4.4) shows a tubular structure formed at pH 10, with a diameter of around 200 nm. This is highly consistent with minimum position of the first oscillation ($q_{firstmin} \sim 0.035 \text{ nm}^{-1}$) in SAXS data through the equation $R = 3.78/q_{firstmin}$ for cylindrical object, which gives average radius of 108 nm for the nanotube structure. In addition, the concurrent disappearance of strong diffraction peaks at WAXS regions suggests the decrease of 2D crystallinity when the C₁₆K₁ bilayer transitions from a planar to a tubular morphology. This transition may arise from the competition between the

intrinsic curvatures of the $C_{16}K_1$ bilayer membrane that drive the formation of microtubular structure, and the intermolecular electrostatic repulsions with the tendency to flatten the membrane to minimize the repulsion energy. When the increasing solution pH reduces the charge on $C_{16}K_1$ molecule, it also reduces the intermolecular electrostatic repulsion energy. Therefore the intrinsic curvature of the bilayer membrane becomes the dominant force that drives the structural transformation from flat membrane to tubular structures. A similar transformation from flat membrane to rolled-up cochleate sheet in $C_{16}K_1$ bilayer membrane system will be discussed in Chapter 5, with qualitative analysis on the competing energies between the electrostatic repulsion and intrinsic membrane curvature.

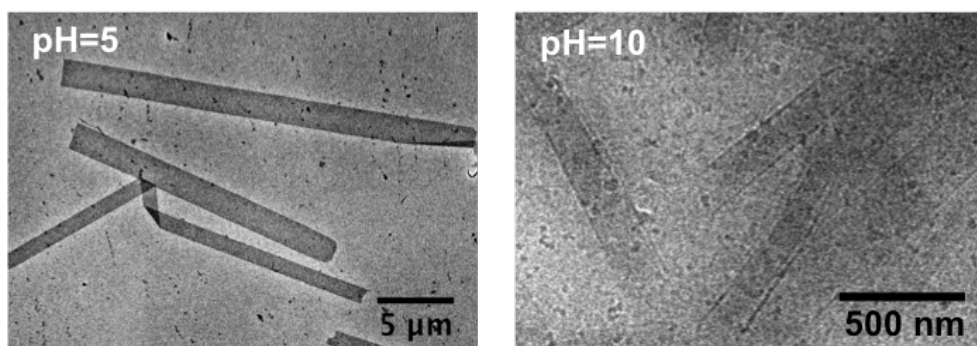


Figure 4.4. Representative cryogenic TEM images of self-assembly formed by $C_{16}K_1$. Flat ribbon morphology with high aspect ratio is found when pH is low (left image). When the pH increases, the flat morphology transforms into tubular structures (right image).

For $C_{16}K_2$ peptide with two lysine groups, the total headgroup charge and size is doubled and therefore the intermolecular electrostatic and steric repulsion becomes stronger.

Consequently, the effective molecular shape turns from nearly cylindrical shape into conical shape where the bilayer assembly is not thermodynamically favorable. For example, when C₁₆K₂ molecules are nearly fully charged (pH 5.3 and 7.2), the SAXS intensity profiles (Figure 4.3b, bottom 2 curves) could be fitted by spherical core-shell models. In this model fitting, the electron density of the core (assumed to comprise of hydrophobic tails) was constrained to be around 80% of that for pure water ($\rho_w = 334 \text{ e}^-/\text{nm}^3$). This assumption is consistent with a non-crystalline, fluid-like packing of alkyl tails. The most robust fitting parameters are the overall spherical radius (R_s) and the electron densities for the core (ρ_{cs}) and the shell (ρ_{ss}). For pH 5.3, $R_s = 2.4 \pm 0.1 \text{ nm}$, $\rho_{cs} = 260 \pm 20 \text{ e}^-/\text{nm}^3$, and $\rho_{ss} = 450 \pm 40 \text{ e}^-/\text{nm}^3$. For pH 7.2, $R_s = 2.7 \pm 0.2 \text{ nm}$, $\rho_{cs} = 250 \pm 30 \text{ e}^-/\text{nm}^3$, and $\rho_{ss} = 450 \pm 40 \text{ e}^-/\text{nm}^3$. The average spherical radius R_s for both pH 5.3 and 7.2 derived from SAXS fitting compare well with the C₁₆K₂ molecular length (2.7 nm), which implies that C₁₆K₂ molecules form spherical micelles structure at low pH. We notice that C₁₆K₂ does not have longer molecular length than C₁₆K₁ because the molecular conformation of two lysine branches on C₁₆K₂ is aligned perpendicular to the carbon backbone, whereas in C₁₆K₁ the lysine group is aligned along the carbon backbone.

In this chapter we keep reiterating that increasing solution pH can reduce the headgroup charge and thus the intermolecular electrostatic repulsion. Here for C₁₆K₂, this effect could induce the structural transformations from loosely packed spherical micelles to tightly packed assembly structures. For example at pH 7.9, where the lysines are partially charged, SAXS intensity (I) profile falls off as q^{-1} in the low q region, and the exponent of -1 at low q indicates long 1D nanostructures. In fact, the intensity profile could be reasonably fitted with a cylindrical core-shell model. Similar to the spherical core-shell model, the average radius of the cylinder R_c

(2.3 ± 0.2 nm) is again close to the $C_{16}K_2$ molecular length (2.7 nm), and the core and the shell electron densities are $\rho_{cs} = 275 \pm 25$ and $\rho_{ss} = 455 \pm 35$ e⁻/nm³, indicating the formation of cylindrical micelle. A visual confirmation of this structural transformation is obtained via cryo-TEM (Figure 4.5). For pH 5 (spherical micelle case), only small globular aggregates are observed. By contrast, 1D nanofibers with persistent lengths > 100 nm are observed for pH 8. Further increasing pH to 9 results in nearly uncharged lysine headgroup. In this case, SAXS intensities I falls off as $q^{-1.5}$ in the low q region. The exponent lies between -1 and -2, which correspond to nanostructures with extended dimension in 1D and 2D respectively. The linear combination of cylindrical core-shell model and symmetric bilayer membrane model is used to reasonably fit the SAXS intensity profiles at pH 8.3 and 9. This approach is verified through cryo-TEM showing a mixture of nanofibers (cylindrical micelle) and nanoribbons (bilayer) for pH 9. Moreover, the appearance of diffraction peaks at WAXS regions for pH 8.3 and 9 also suggest the formation of crystalline bilayer in addition to cylindrical micelle. To reduce the free parameters in the fitting of SAXS data from the bilayer-cylindrical micelle mixture, the parameters for the cylinder component were held fixed at the best fit values obtained for pH 7.9, as described above. That is, $R_c = 2.3$ nm; $\rho_{cs} = 275$ e⁻/nm³, and $\rho_{ss} = 455$ e⁻/nm³. The best-fit parameters for the SAXS data reveal that in going from pH 8.3 to 9, the fraction of the bilayers indeed increases from 51 ± 20 to $73 \pm 20\%$. For the bilayer component, fitting of the SAXS data reveals thickness $t_t = 2.2 \pm 0.5$ nm for the hydrophobic tail region, and the enhanced electron density of the hydrophobic region $\rho_t = 330$ e⁻/nm³ corresponds to a crystalline packing of the alkyl tails. The hydrophobic region thickness is substantially smaller than the length of two fully extended alkyl tails, implicating that the two leaflets of the bilayer are strongly interdigitated.

Overall, SAXS and cryo-TEM shows that, with increasing pH and reducing molecular charge, $C_{16}K_2$ molecular assemblies undergo transitions from spherical micelles to long cylindrical micelles to planar bilayers with the two bilayer leaflets interdigitated.

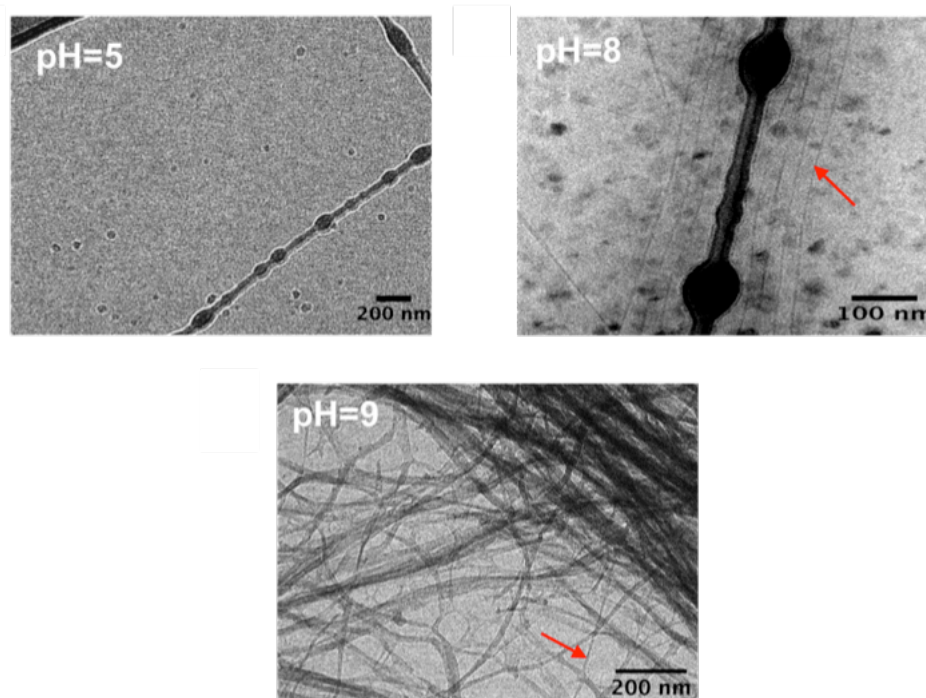


Figure 4.5. Representative cryogenic TEM images of self-assembly formed by $C_{16}K_2$. No elongated objects are observed at pH 5, while the solution at pH 8 shows long fibers (red arrow). The black rod in the center is lacey carbon grid. Black stains in the background are excessive ethane from sample preparation. At pH 9, flat ribbons can be observed, and there are also indications of long fibers (red arrow) similar to the fibers formed at pH 8.

Both SAXS and cryo-TEM reveal that C₁₆K₃ and C₁₆K₄ manifest very similar morphological transformations as C₁₆K₂, except that at very low pH, the SAXS intensity profile of C₁₆K₃ and C₁₆K₄ do not show any scattering features, indicating that no ordered self-assembly structures are formed when the molecules are nearly fully charged. This could be attributed to the fact that C₁₆K₃ and C₁₆K₄ have even stronger intermolecular electrostatic and steric repulsion than C₁₆K₂ molecule. With increasing pH, C₁₆K₃ and C₁₆K₄ exhibit the transition from unaggregated state to spherical micelles to cylindrical micelles and to crystalline interdigitated bilayer. Here we were not able to capture the pure cylindrical micelle phase in C₁₆K₄ and we speculate that it may exist at very narrow pH range. The fitting of SAXS results yield that for C₁₆K₃, the spherical micelle has radius of $R_s = 2.8 \pm 0.3$ nm and the cylindrical micelle has radius of $R_c = 2.4 \pm 0.2$ nm. For C₁₆K₄, the spherical micelle has radius of $R_s = 2.9 \pm 0.2$ nm. Since C₁₆K₃ and C₁₆K₄ have the same hydrocarbon chain as C₁₆K₂, the electron densities and the length of hydrophobic tail used in the model fittings are fixed to the values from what we discussed in C₁₆K₂ model fittings. The electron densities measured for headgroup regions are 420 ± 55 e⁻/nm³ for C₁₆K₃ spherical micelle, 440 ± 30 e⁻/nm³ for C₁₆K₃ cylindrical micelle, and 450 ± 40 e⁻/nm³ for C₁₆K₄ spherical micelle. The cryo-TEM images also show the transformation into 1-D cylindrical fiber structures for C₁₆K₃ when the pH is increased to 8.4. When C₁₆K₃ and C₁₆K₄ are nearly uncharged (pH 8.8 for K₃ and pH 10 for K₄), the intensity profiles can be reasonably fit by the linear combination of cylindrical core-shell model and symmetric bilayer membrane model, and Cryo-TEM images of both C₁₆K₃ and C₁₆K₄ show the mixture of nanofibers (cylindrical micelle) and nanoribbons (bilayer). The fitting results reveal that, for the bilayer component, the thicknesses of hydrophobic tail region are $t_f = 2.0 \pm 0.2$ nm (C₁₆K₃) and 1.9 ± 0.2 nm (C₁₆K₄). The electron

density of the hydrophobic region $\rho_t = 330 \text{ e}^-/\text{nm}^3$ corresponds to a crystalline packing of the alkyl tails as C_{16}K_2 bilayer. Same as C_{16}K_1 and C_{16}K_2 , the hydrophobic region thicknesses of the C_{16}K_3 and C_{16}K_4 are substantially smaller than the length of two fully extended C_{16} alkyl tails, indicating C_{16}K_3 and C_{16}K_4 also self-assemble into strongly interdigitated crystalline bilayers when the headgroup charge is significantly reduced. From packing parameter theory, the amphiphiles with large headgroup compared with hydrocarbon tail have the conical packing shape, and should assemble into loosely packed micelles due to the steric repulsion from the headgroup. However, from geometric aspect, the molecular packing in the interdigitated bilayer state increases the inter-headgroup spacing and decreases the inter-tail distance, which could reduce the steric repulsion between the large ionizable headgroups, and also maximize the van der Waals attractions among the alkyl tails. Therefore, we believe that interdigitated state should be a general characteristic of the bilayer assemblies of amphiphiles with headgroup cross-section areas much larger than the alkyl tail, which provides an extension to the well-accepted packing parameter theory.

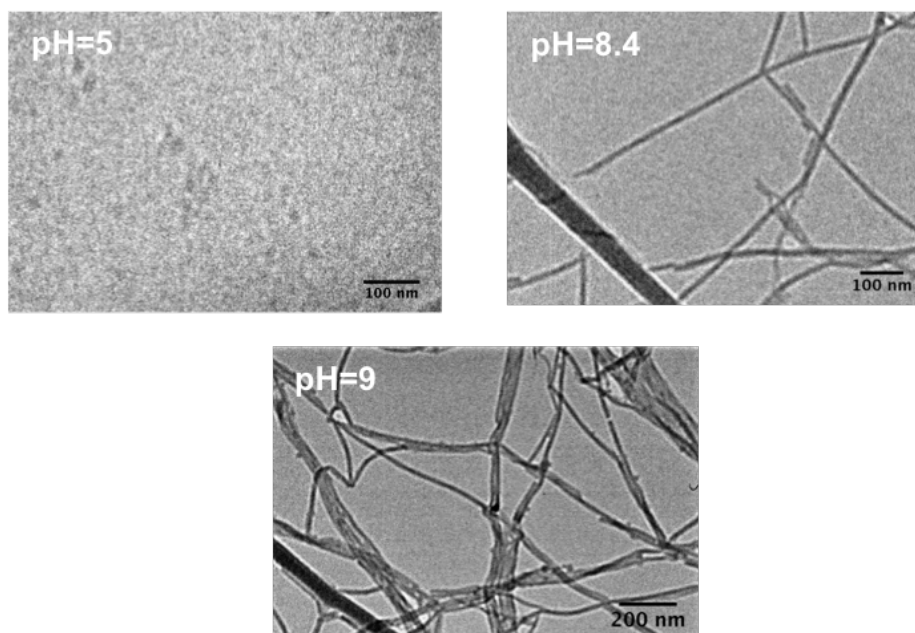


Figure 4.6. Representative cryogenic TEM images of self-assembly formed by $C_{16}K_3$. No elongated objects are observed at pH 5, and the solution at pH 8.4 shows only the long fibers. Further increase to pH 9 induces the formation of flat ribbons in addition to long fibers.

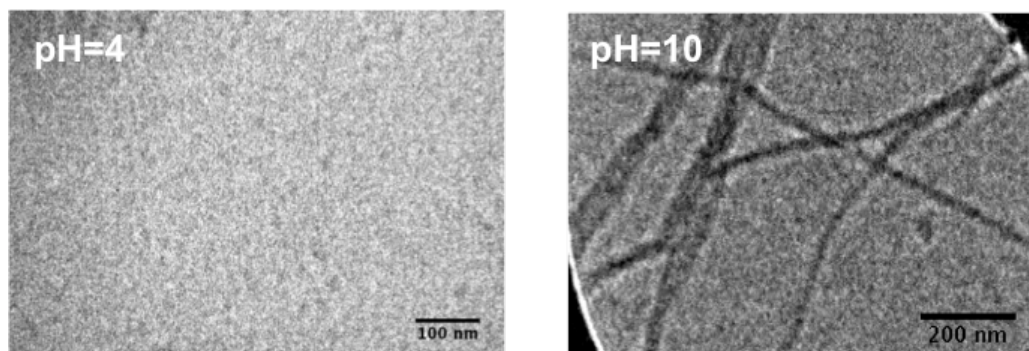
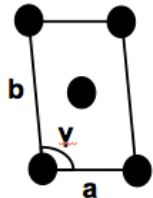
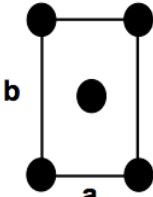
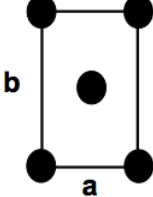


Figure 4.7. Representative cryogenic TEM images of self-assembly formed by $C_{16}K_4$. Similar with $C_{16}K_3$, no objects are observed at low pH. The formation of both flat ribbons and long fibers is shown at pH 10. Intermediate phase with the only cylindrical fibers is not captured in $C_{16}K_4$.

The diffraction peaks observed at the WAXS region are used to deduce the angstrom scale molecular packing within the $C_{16}K_n$ crystalline bilayers. The strongest Bragg reflections were found in the $13 < q < 16 \text{ nm}^{-1}$ range, which roughly corresponds to real space distances of $0.48 > 2\pi/q > 0.4 \text{ nm}$. These distances are close to the cross-sectional diameter of the C_{16} alkyl tails. Therefore, within the $C_{16}K_n$ bilayers, the molecular alkyl tails are packed on a crystalline lattice such that the nearest neighbor distances are commensurate with the tail diameter. Table 4.2 lists the peak positions and corresponding lattice types and lattice parameters of crystalline bilayers. For $C_{16}K_1$, $C_{16}K_2$ and $C_{16}K_3$, two strong diffraction peaks in the WAXS region are observed with an approximately 1:2 intensity ratio, which indicate a two-dimensional rectangular-C lattice ($C_{16}K_2$ and $C_{16}K_3$) or a lattice slightly distorted from rectangular-C ($C_{16}K_1$). However, in $C_{16}K_4$, the second peak at Q2 becomes significantly weaker than the first peak at Q1. We speculate that this might be attributed to the preferential orientation of lattice structure with respect to the high-aspect-ratio ribbon morphology. As an extension of the current study, the WAXS-predicted molecular arrangement will be refined in future grazing-incidence WAXS (GIWAXS) studies on bilayers deposited on solid substrates. This aligned geometry may also allow observation of higher order diffraction peaks, which may have been smeared out due to the intrinsic powder averaging in solution scattering, thereby yielding higher spatial resolution for molecular packing.

Table 4.2. WAXS diffraction peak positions and derived lattice structures of $C_{16}K_n$ bilayers

WAXS data	Peak positions	Lattice type	Lattice constant
$C_{16}K_1$ at pH 4.6	$Q1 = 13.9 \text{ nm}^{-1}$ $Q2 = 15.0 \text{ nm}^{-1}$ $Q3 = 16.2 \text{ nm}^{-1}$ $Q4 = 25.8 \text{ nm}^{-1}$	Oblique 	$a = 0.49 \text{ nm}$ $b = 0.85 \text{ nm}$ $\gamma = 100^\circ$
$C_{16}K_2$ at pH 9	$Q1 = 13.3 \text{ nm}^{-1}$ $Q2 = 15.2 \text{ nm}^{-1}$	Rectangular-C 	$a = 0.46 \text{ nm}$ $b = 0.95 \text{ nm}$
$C_{16}K_3$ at pH 8.8	$Q1 = 13.3 \text{ nm}^{-1}$ $Q2 = 15.2 \text{ nm}^{-1}$	Rectangular-C 	$a = 0.46 \text{ nm}$ $b = 0.95 \text{ nm}$
$C_{16}K_4$ at pH 10	$Q1 = 13.1 \text{ nm}^{-1}$ $Q2 = 15.2 \text{ nm}^{-1}$	Undefined	N/A

Based on the above SAXS/WAXS and Cryo-TEM results, we are able to establish a phase diagram shown in Figure 4.8 as function of pH and headgroup. In this diagram, we can observe that as the headgroup size decreases and pH increases (i.e. headgroup charge decreases), the equilibrium self-assembly structure transforms from ill-defined unaggregated state to spherical micelles, to cylindrical micelles, to nanoribbons, and finally to microtubules, which depicts the correlation between intermolecular interaction and resulting assembly structures. Strong

intermolecular repulsion (electrostatic and steric) could lead to loosely packed assembly structures (spherical micelles) or even no assembly at all, while the weak repulsion favors the formation of closely packed assemblies such as crystalline bilayers. Future work could focus on the theoretical simulation of the assembly structures (i.e. Molecular Dynamic simulation) to quantitatively describe the correlations between the thermodynamic equilibrium structures and the strength of intermolecular interactions.

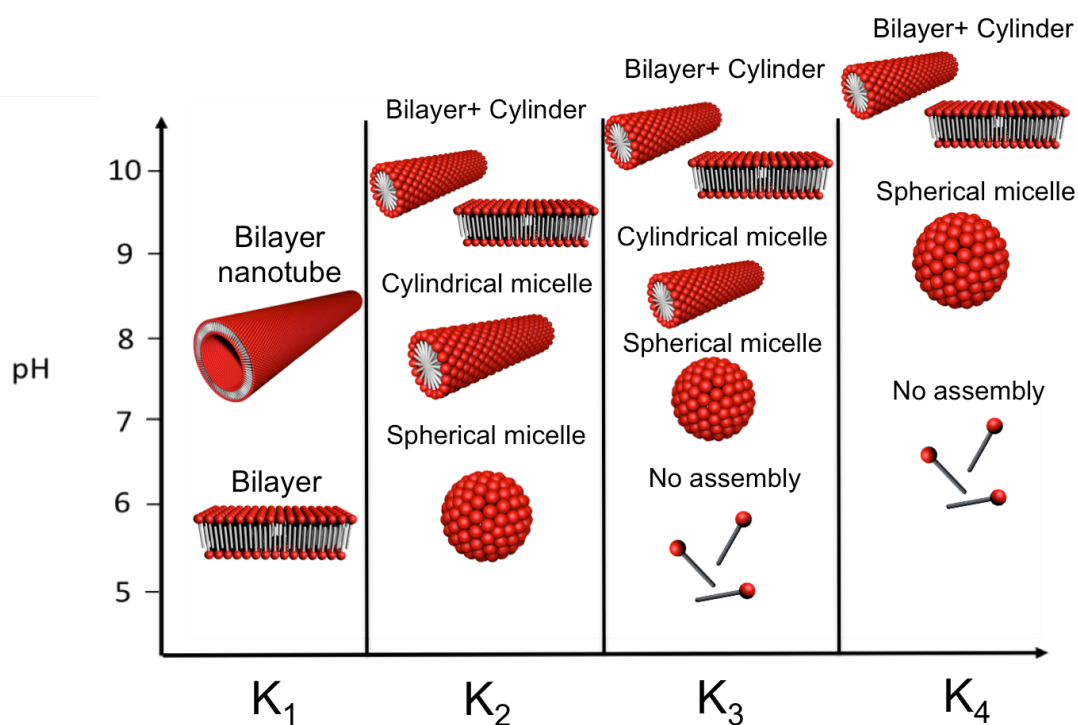


Figure 4.8. Phase diagram showing the formation and transition of self-assembly morphology of $C_{16}K_n$ peptide amphiphile as a function of headgroup size and pH.

4.4. Summary

We designed an ionic peptide amphiphile series $C_{16}K_n$ and show that charge regulation via pH and headgroup size regulation can induce polymorphism of self-assembly structures from spherical micelles to cylindrical nanofibers to crystalline bilayer membrane and to nanotubes. The transition from loosely packed (micelles) to tightly packed assembly (bilayer) can be observed when the intermolecular electrostatic repulsion is reduced. By contrast, the tightly packed assembly (bilayer) is still favorable even for $C_{16}K_4$ where the headgroup size is much larger than the alkyl tail. SAXS analysis exhibit that the crystalline bilayer structures of $C_{16}K_n$ are strongly interdigitated. The interdigitation between the two bilayer leaflets increase the interheadgroup spacing and also maximize the intermolecular van der Waals' interaction. Therefore, this should be a general characteristic of the bilayer assemblies of the amphiphiles with headgroup dimensions much larger than the alkyl tail diameter.

Chapter 5. Electrostatic Control of Nanoribbon-to-Cochleate Transition in a Charged Peptide Amphiphile Assembly

5.1. Introduction

Amphiphilic molecules can self-assemble into a variety of 3D, 2D and 1D nano- and meso-structures. These structures serve as simplified models for understanding biological assemblies and their functions and have wide-ranging applications in drug delivery[5, 6, 45, 46], regenerative medicine[47], biosensing[48], hydrogen fuel production[49, 50] and clean water technologies[51]. An interesting assembly structure is the nanoribbon, which is a high aspect ratio ($\sim 10:1$ or greater) bilayer. Nanoribbons are gateway to a number of morphologies with distinct functionalities. For example, nanoribbons of a charged chromophore amphiphile transform to scroll-like (cochleate) morphology when the ionic strength of the solution is increased.[49] These cochleate structures serve as efficient charge transfer agents for photocatalysts in hydrogen production. Cochleate formation from liposomes of negatively charged phospholipids in the presence of multivalent cations also involves a nanoribbon intermediate.[45, 52, 53] Biocompatible phospholipid cochleates are being explored as drug-delivery agents because they can trap macromolecules such as proteins, peptides and DNA, and provide protection against degradation due to their multilayer geometry. Nanoribbons have also been observed in peptide amphiphiles (PA), which are amphiphiles where a sequence of amino acids are covalently linked to an alkyl tail. In a PA with alternating charged and neutral amino acids, nanoribbons were found to transform to helical ribbons as the PA concentration was

reduced[34] and to helical and twisted nanoribbons when the amino acid sequence was permuted.[24] Helical supramolecular assemblies have been previously used to template semiconductor nanohelices.[54] Despite the progress, the correlation between experimental conditions such as molecular design, ionic strength, pH, amphiphile concentration and the attained nanoribbon-related morphology are not fully established. Therefore, precise control of nanoribbon assembly architecture requires further understanding of the delicate interplay between intermolecular interactions and elastic and interfacial energies.

A recent theoretical study showed that for charged molecules, tuning the range of electrostatic interactions could induce transitions between different nanoribbon-related morphologies.[55] Specifically, a phase diagram was deduced for a 2D lattice of charged points, which interacted *via* long-ranged repulsive electrostatic interactions and short-ranged attractive interactions. Planar nanoribbon to wavy ribbon with periodic undulations to helical ribbon transitions were predicted as the range of the electrostatic interactions is increased. This study suggests a facile experimental method for accessing distinct nanoribbon architectures by varying the ionic strength (μ) of the solution because the range of electrostatic interactions as parameterized by Debye length (λ_D) scales as $\mu^{-1/2}$. Recent experiments also attest that tuning the ionic strength leads to predictable changes in the nanoribbon-related assembly morphology. For example, the period of the twists in amyloid fibril aggregates monotonically increases with decreasing ionic strength. [56]

In this study, we focus on the morphological changes in charged planar nanoribbons as a function of increasing ionic strength. In this regime, the inter-nanoribbon interactions become

prominent and as mentioned above nanoribbon to cochleate transformations have been observed in phospholipids[52] and chromophore amphiphiles[35, 49, 50, 57]. However, the generality and the mechanistic details of this transition are still unknown. In particular, the correlation between the ionic strength induced changes in the molecular packing and the mesoscopic morphology transformations are elusive. The principal aim of this study is to start with a nanoribbon structure and experimentally trace the μm to \AA length scale transformations in the membrane structure as a function of ionic strength by using a combination of cryo-transmission electron microscopy (cryo-TEM), atomic force microscopy (AFM) and in situ small and wide angle X-ray scattering (SAXS/WAXS). The experiments are coupled with simplified theoretical models that qualitatively explain each of the observed morphological transitions.

5.2 Materials and Methods

5.2.1. Sample Preparation

C_{16}K_1 Peptides were synthesized in the Peptide Synthesis Core at the Simpson Querrey Institute for BioNanotechnology of Northwestern University using a CEM Liberty microwave-assisted peptide synthesizer. Standard fluorenylmethoxycarbonyl (Fmoc) solid-phase peptide synthesis was used with rink amide MBHA resin (100-200 mesh). For each coupling, 5 equivalents of Fmoc-protected amino acid (or palmitic acid) in DMF was added with 5 equivalents of N,N,N',N' -tetramethyl- O -(1H-benzotriazol-1-yl)uronium hexafluorophosphate (HBTU) in DMF and 10 equiv of N,N -diisopropylethylamine (DIPEA) in NMP. Fmoc removal was accomplished using a solution of 20% piperidine in DMF and 0.1 M 1-hydroxybenzotriazole

(HOBt). Peptides were cleaved from the resin using a mixture of 95% trifluoroacetic acid (TFA), 2.5% water, and 2.5% triisopropylsilane for 3 h. Crude peptide was precipitated from this solution using cold diethyl ether. Purification was carried out on a Waters Prep 150 HPLC using a water/acetonitrile with 0.1% TFA solvent system and a Phenomenex Kinetex 30x150 mm C18 column. Eluting fractions were analyzed by ESI-MS using an Agilent 6520 Q-TOF LCMS before lyophilization and purity analysis by the same Agilent LCMS (water/acetonitrile with 0.1% formic acid solvent system and Phenomenex Proteo 100 x 1 mm column).

5.2.2. Characterization Methods

To monitor the assembly structure of $C_{16}K_1$ as a function of salt concentration, $C_{16}K_1$ molecules with trifluoroacetate counterions (CF_3COO^-) are dissolved in aqueous solution at 4 mM concentration with different NaCl concentrations (from 1 to 100 mM). SAXS/WAXS, Cryogenic transmission electron microscopy (Cryo-TEM) imaging, and Atomic Force Microscopy (AFM) are then used to study the structure of the PA assemblies in aqueous solution. Grazing Incidence Wide Angle X-ray Scattering (GIWAXS) is used to determine the 2D crystalline structure of $C_{16}K_1$ bilayer membranes drop-casted on the solid silicon substrate. Detailed experimental setups are discussed in Chapter 3.

5.3 Results and Discussion

For the present work, we chose the simplest possible charged peptide amphiphile (PA): $C_{16}K_1$, where a single ionizable amino acid lysine (K) is covalently linked to a palmitoyl (C_{16})

alkyl tail (Fig. 5.1a). The choice of this PA ensures that the inter-headgroup interactions are Coulombic. This is unlike the case of other PAs with multiple amino acids, where the assembly is strongly modulated by intermolecular hydrogen bonding. Also in Chapter 4, the preliminary Cryo-TEM and SAXS/WAXS results on $C_{16}K_1$ shows purely the bilayer nanoribbon morphology, while increasing the headgroup size to $C_{16}K_2$ could induce the formation of loosely packed spherical micelle structure.

Figure 5.1b shows the atomic force microscopy (AFM) image of $C_{16}K_1$ assemblies at a silica (SiO_x)/water interface. It reveals that in the absence of added salt, $C_{16}K_1$ assembles into flat, rectangular ribbons, with widths (w) in the range of a few hundred nm, lengths (l) ranging from 2 to 20 μm , and aspect ratio (l/w) as high as 30. All the ribbons exhibit the same thickness of ~ 4.0 nm, as shown by a representative AFM height scan in Figure 5.1c. This thickness is intermediate of the expected heights of ~ 2.7 nm and ~ 5.4 nm for a monolayer and a bilayer of fully extended $C_{16}K_1$ molecules (Fig. 5.1a). The above observation suggests that the $C_{16}K_1$ ribbons are bilayers with the alkyl tails of the two leaflets strongly interdigitated. The interdigitated bilayer configuration, which has also been observed in Chapter 4 about $C_{16}K_n$ assemblies, is expected for molecules with headgroup cross-sectional areas much larger than that for the alkyl tails. We will show later *via* a simple theoretical model that the observed high aspect ratio in the charged nanoribbon can arise due to a competition between the membrane surface energy and the long range electrostatic interactions.

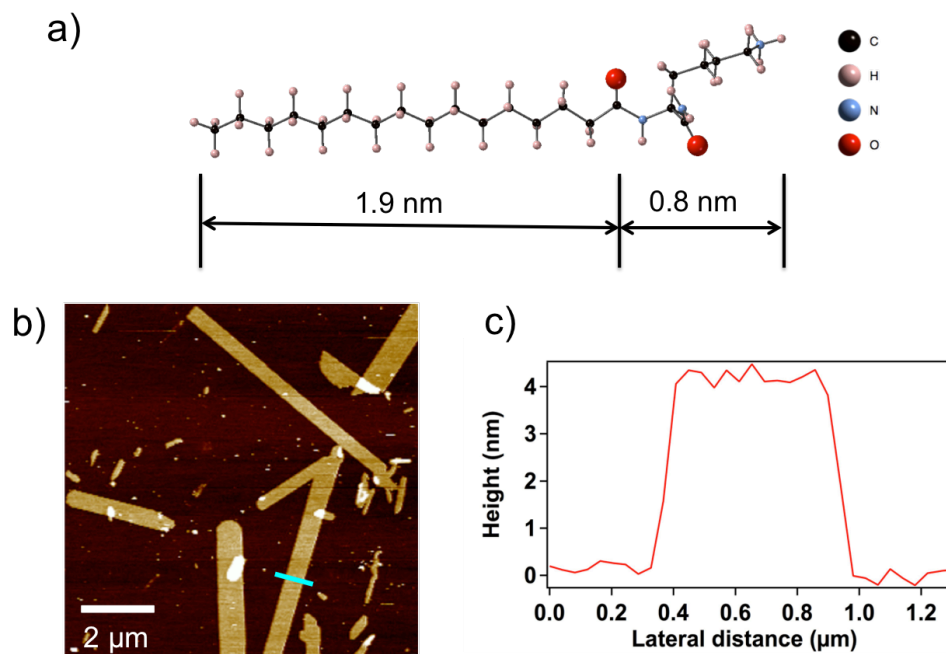


Figure 5.1. (a) Molecular structure of +1 charged C₁₆K₁ peptide with estimates for hydrophobic tail length and hydrophilic headgroup length. The molecular conformation was derived from an MD simulation for a single C₁₆K₁ molecule in water using the Universal force field.[58] (b) Atomic Force Microscopy image at a silica/water interface showing high aspect ratio C₁₆K₁ ribbons. (c) The height profile for a nanoribbon. The scan was performed along the green line in Figure 5.1b.

To understand the effects of screening of intermolecular electrostatic interactions on the assembly morphology, we analyzed dispersions of C₁₆K₁ in solutions containing NaCl at concentrations ($c = \Delta\mu$) ranging from 0 to 100 mM. Figure 5.2a-d show atomic force microscopy (AFM) images of C₁₆K₁ assemblies at Si/NaCl solution interfaces for $c = 0, 1, 3$ and 5 mM.

Peakforce error images are shown because they deliver better 3D representation of the assembly morphologies. As the NaCl concentration is increased the aspect ratio of the ribbons decreases, and at $c = 3$ mM, nearly isotropic sheets of 1-2 μm diameter are observed (Figure 5.2c). At or above this threshold concentration c_{th} , the sheets roll into scrolls or cochleates (Figure 5.2d). The multi-layered nature of the scrolls is better observed in cryo-transmission electron microscopy (cryo-TEM) images (Figure 5.2e-h). These cryo-TEM images (Figure 5.2f-h) further reveal that the interlayer spacing (D) within the cochleate structure monotonically decreases with increasing c . Overall, AFM and cryo-TEM show that for C_{16}K_1 , increasing the solution ionic strength first induces the ribbon to cochleate transition, and thereafter, reduces the inter-lamellar spacing within the cochleates.

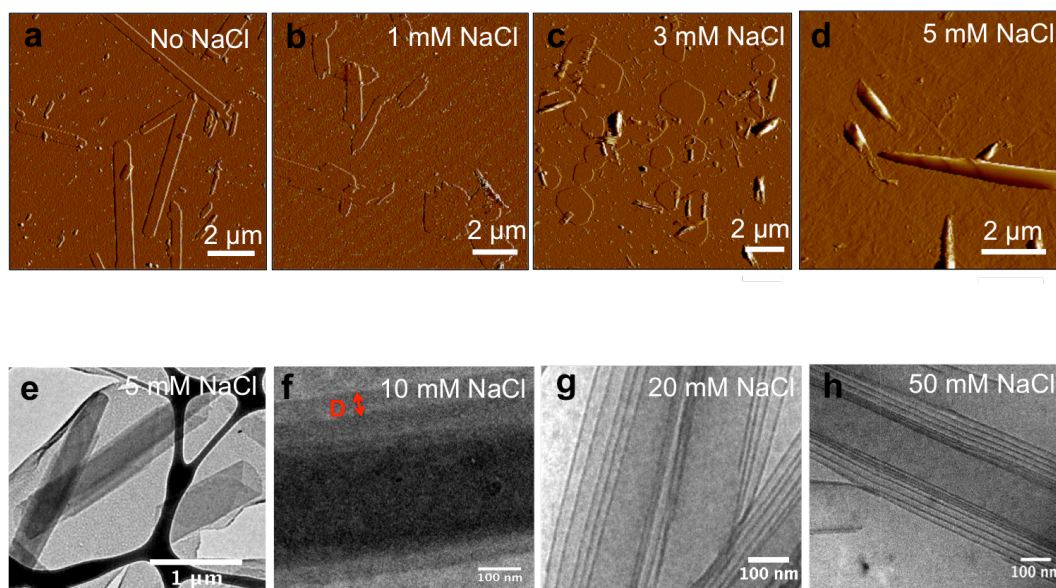


Figure 5.2. (a-d) AFM peakforce error images for C_{16}K_1 membranes at Si/NaCl solution interfaces. As the NaCl concentration increases, nanoribbon to isotropic sheet and to rolled-up cochleate transformations are observed. (e-h) Cryogenic TEM images of cochleates exhibit scroll

morphology and the internal multilayer features. It can be readily seen that the interbilayer spacing D within the cochleate structure decreases with increasing NaCl concentration.

In situ small and wide angle X-ray scattering (SAXS/WAXS) was performed to obtain ensemble-averaged, quantitative details of the mesoscopic morphology (SAXS) and the molecular packing (WAXS) in the ribbons and the cochleate structures. We first describe the X-ray scattering from $C_{16}K_1$ ribbons in pure water. Figures 5.3a and 5.3b show the background subtracted SAXS and WAXS data, respectively, as a function of scattering vector magnitude $q = 4\pi\sin(\theta)/\lambda$. Here, λ is the X-ray wavelength, and 2θ is the scattering angle. Two key qualitative observations can be made. First in the very low q region: $q < 0.4 \text{ nm}^{-1}$ (Figure 5.3a), the intensity I drops off as q^{-2} . This exponent of -2 is indicative of mesostructures with extended sizes in 2D, and is consistent with the AFM observation of flat ribbons, which have length and width both greater than $2\pi/q_{\min} \sim 2\pi/0.02 \sim 300 \text{ nm}$. Here, q_{\min} is the minimum accessible scattering vector magnitude in the experiments. Second, Figure 5.3b shows multiple diffraction peaks in the WAXS regime. The strongest Bragg reflections were found in the $\sim 13 < q < 16 \text{ nm}^{-1}$ range, which roughly corresponds to real space distances of $0.48 > 2\pi/q > 0.4 \text{ nm}$. These distances are close to the cross-sectional diameter of the alkyl tails. Therefore, within the ribbons, the molecular alkyl tails are packed on a crystalline lattice such that the nearest neighbor distances are commensurate with the tail diameter. This crystalline packing also suggests that the alkyl tails or at least significant segments of the alkyl tails adapt extended all-trans configuration.

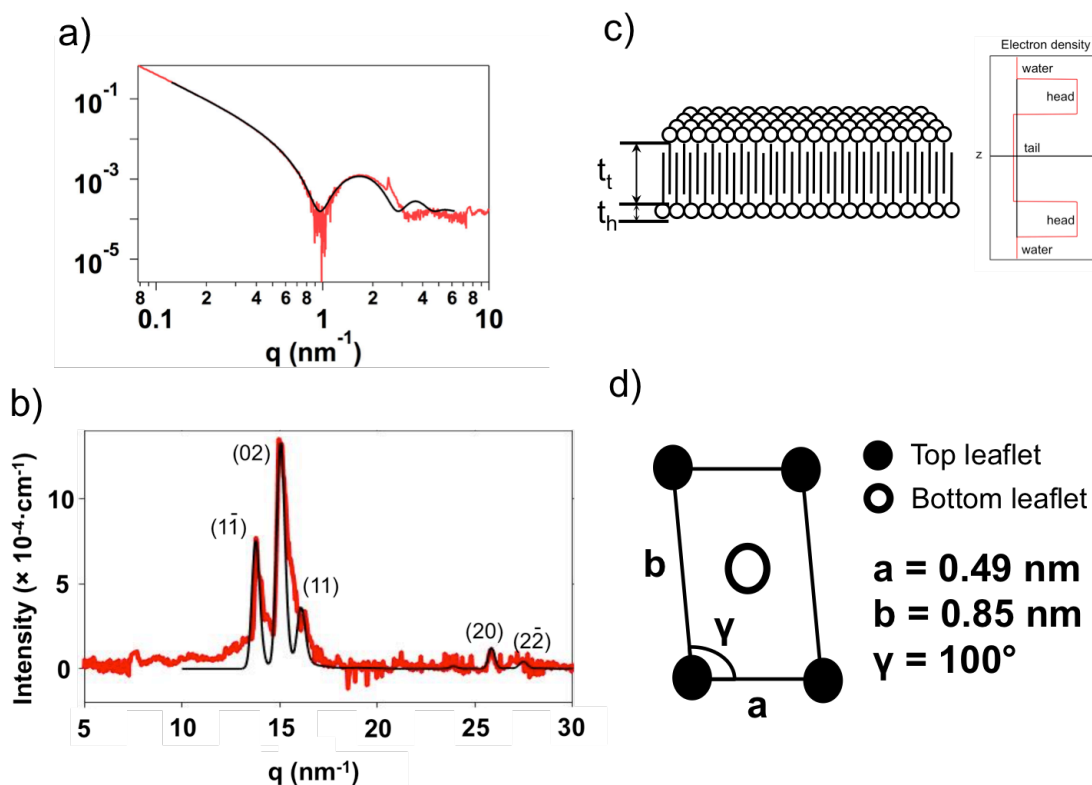


Figure 5.3. (a) Background subtracted *in situ* small-angle X-ray scattering intensity profile for $C_{16}K_1$ ribbon in zero salt condition. The solid black curve is the best fit over the range of $0.1 < q < 6 \text{ nm}^{-1}$ using a symmetric bilayer model. (b) Background subtracted *in situ* wide-angle X-ray scattering intensity profile for $C_{16}K_1$ ribbons in pure water shows diffraction peaks over the range of $10 < q < 30 \text{ nm}^{-1}$. The solid black curve is the simulated diffraction pattern. (c) The interdigitated $C_{16}K_1$ bilayer structure and electron density profile determined from small-angle X-ray scattering data. (d) 2D oblique unit cell and lattice parameters derived from wide-angle X-ray scattering data.

For fitting the SAXS data in Figure 5.3a, we used a simplified symmetric bilayer model with a uniform density hydrophobic tail region sandwiched between two hydrophilic headgroup regions. The electron density for the hydrophobic tail region was fixed at $\rho_t = 320 \text{ e}^-/\text{nm}^3$, the expected value for crystalline arrangement of densely packed alkyl tails. The best match for the SAXS data (black curve, Figure 5.3a) was obtained with thicknesses $t_t = 2.3_{-0.0}^{+0.5} \text{ nm}$ and $t_h = 0.85_{-0.45}^{+0.0} \text{ nm}$ for the tail and the head regions, respectively and $\rho_h = 386_{-0}^{+61} \text{ e}^-/\text{nm}^3$ for the electron density of the headgroup. For the fitting, the upper bound for t_h was set to 0.85 nm, based on the molecular dynamics simulations for a single C_{16}K_1 molecule in water (Figure 5.1a). The most robust fitting parameter corresponding to the bilayer thickness $2t_h + t_t = 4.0_{-0.4}^{+0.0} \text{ nm}$ is clearly consistent with the AFM measurements (Figure 5.1c). The fitting of the SAXS data for the ribbons reveals a much lower thickness of the hydrophobic region as compared to the length of two fully extended C_{16} tails ($2 \times 1.9 \text{ nm}$). This supports our earlier hypothesis that the two leaflets of the bilayer are strongly interdigitated. The SAXS observations are summarized schematically in Figure 5.3c. It should be noted that the close packing of molecular tails as suggested by the WAXS data is prohibitive in a monolayer (or an individual bilayer leaflet) of C_{16}K_1 because of the large width of the C_{16}K_1 headgroup as compared to the alkyl tail diameter. Interdigitation overcomes this constraint, and allows the tails to pack tightly to maximize the intermolecular van der Waals interactions.

The WAXS data (Figure 5.3b) shows three strong Bragg reflections peaked at $q = 13.9$, 15.0 and 16.2 nm^{-1} due to the crystalline packing of alkyl tails. In general, if the alkyl tails can be considered as cylindrical on average due to static or thermal disorder then the diffraction pattern

consists of a single 3-fold degenerate first order peak arising from the arrangement of tails on a hexagonal lattice. This degeneracy can be lifted, for example, due to a strain induced by the alignment of alkyl tail backbone planes along specific crystallographic directions. In particular, three closely spaced diffraction peaks indicate an oblique unit cell. In the present case, the diffraction pattern is consistent with a primitive unit cell defined by $a = 0.49$ nm, $b = 0.53$ nm and $\gamma = 127^\circ$. In order to distinguish between the alkyl tails from the two leaflets, the unit cell may be redefined by $a = 0.49$ nm, $b = 0.85$ nm and $\gamma = 100^\circ$. In this unit cell, the tails at the vertices and the center belong to different leaflets, as shown in Figure 5.3d. By using these unit cell parameters and a parallelepiped model for the alkyl tails (see *Appendix B* for details), we could replicate in a simulation the positions and the intensities of the Bragg reflections over an extended range $10 < q < 30$ nm⁻¹ (Figure 5.3b, black curve). The WAXS analysis also reveals an average 2D crystal domain size of ~ 15 nm that is significantly smaller than the ribbon size, indicating that the ribbons are polycrystalline.

SAXS/WAXS data from planar ribbons exhibit weak, but sharp Bragg reflections even in the $q \leq 10$ nm⁻¹ regime. The most prominent of these reflections is centered at $q = 2.5$ nm⁻¹, and rides over the broad intensity modulation due to the bilayer form factor (Figure 5.3a). A much weaker, but reproducible reflection is also observed at $q = 7.5$ nm⁻¹ (Figure 5.3b). In fact, complementary grazing incidence X-ray scattering (GIXS) measurements of ribbons drop-casted onto a Si substrate reveal q_z -extended intensity rods at $q_{xy} = 2.5, 5.0, 7.5$ and 10 nm⁻¹ (Figure 5.4). Here, q_{xy} and q_z are the components of the scattering vector in the bilayer plane and along the bilayer-normal direction, respectively. Thus GIXS shows that the low q Bragg reflections

originate from an in-plane ordering within the bilayer, most likely due to a preferred orientational alignment of C₁₆K₁ headgroups with respect to the crystallographic axes defining the alkyl tail lattice. This headgroup ordering is commensurate with the alkyl tail lattice, and can be defined by a unit cell that is a 1 × 3 supercell of the alkyl tail unit cell in Figure 5.3d. This is because the magnitude of the first Bragg reflection ($q_1 = 2.5 \text{ nm}^{-1}$) equals one third of the magnitude of (01) reciprocal lattice vector for the alkyl tail lattice: $q_1 = 1/3 \times b^* = 1/3 \times 2\pi/(b \times \sin\gamma)$. Perhaps, the headgroups of the neighboring C₁₆K₁ molecules along the *b* axis are rotated 120° clockwise (or anticlockwise) relative to each other about the bilayer-normal. Such an arrangement would explain the 3× larger periodicity in the headgroup ordering. However, proving this hypothesis requires a detailed molecular modeling that is beyond the scope of the current studies. This aspect along with other subtle structural features of the ribbons and cochleates will be discussed elsewhere. Overall, the SAXS/WAXS analysis of C₁₆K₁ ribbons in pure water proves that ribbons are bilayers with interdigitated leaflets and that the packing of alkyl tails as well as headgroups exhibits crystalline ordering.

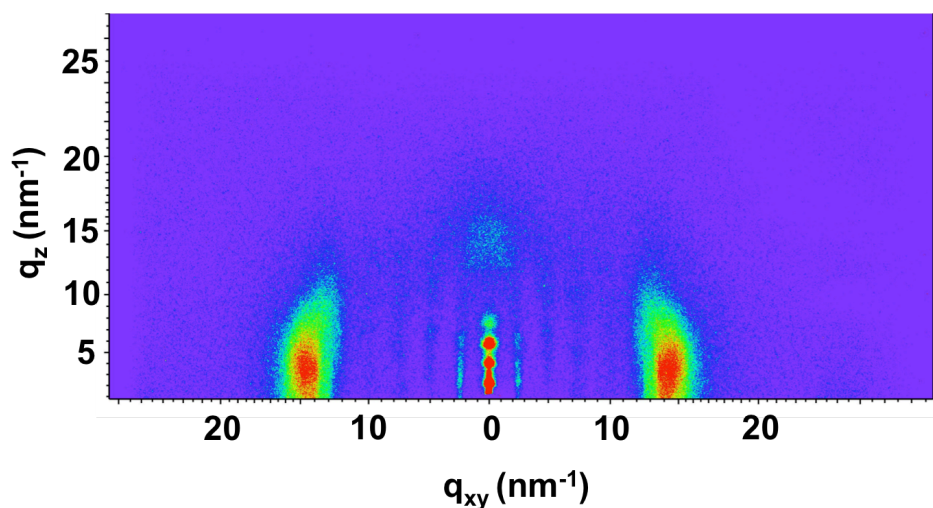


Figure 5.4. Grazing-Incidence X-ray scattering from $C_{16}K_1$ bilayer drop-casted on Si (001) substrate. Scattered intensity was scaled from blue (weak) to red (strong). The long exposure time required to clearly discern the intensity rods at $q_{xy} = 2.5, 5, 7.5$ and 10 nm^{-1} resulted in detector saturation in the region $13 < q_{xy} < 16 \text{ nm}^{-1}$. Therefore, the three diffraction peaks from the packing of alkyl tails observed in solution SAXS in this region appear as a broad maximum in GIXS, and cannot be separated out.

In situ solution SAXS/WAXS was also used to trace the ribbon to cochleate transformation as well as the changes in the cochleate structure as a function of NaCl concentration. Figures 5.5a and 5.5b show X-ray scattering from 4 mM $C_{16}K_1$ at low ($c = 1 - 5 \text{ mM}$) and high ($c = 5 - 50 \text{ mM}$) NaCl concentrations, respectively. Figure 5.5a shows that for $c \geq 2 \text{ mM}$ and for $q < 0.1 \text{ nm}^{-1}$, the monotonic fall in intensity ($I \propto q^{-2}$) is replaced by multiple intensity modulations due to cochleate formation. The SAXS-deduced threshold NaCl concentration of 2 mM for ribbon to

cochleate transition is only slightly lower than the threshold $c_{th} = 3$ mM in AFM experiments. More importantly, this threshold concentration of 2-3 mM NaCl for the ribbon to cochleate transition appears to be independent of the $C_{16}K_1$ concentration, as the SAXS experiments on 10 mM $C_{16}K_1$ solutions show the same threshold concentration (Figure 5.6). Therefore, rolling of the membrane into cochleates is driven by the solution ionic strength; in other words, the range of intermolecular electrostatic interactions controls the ribbon to cochleate transition.

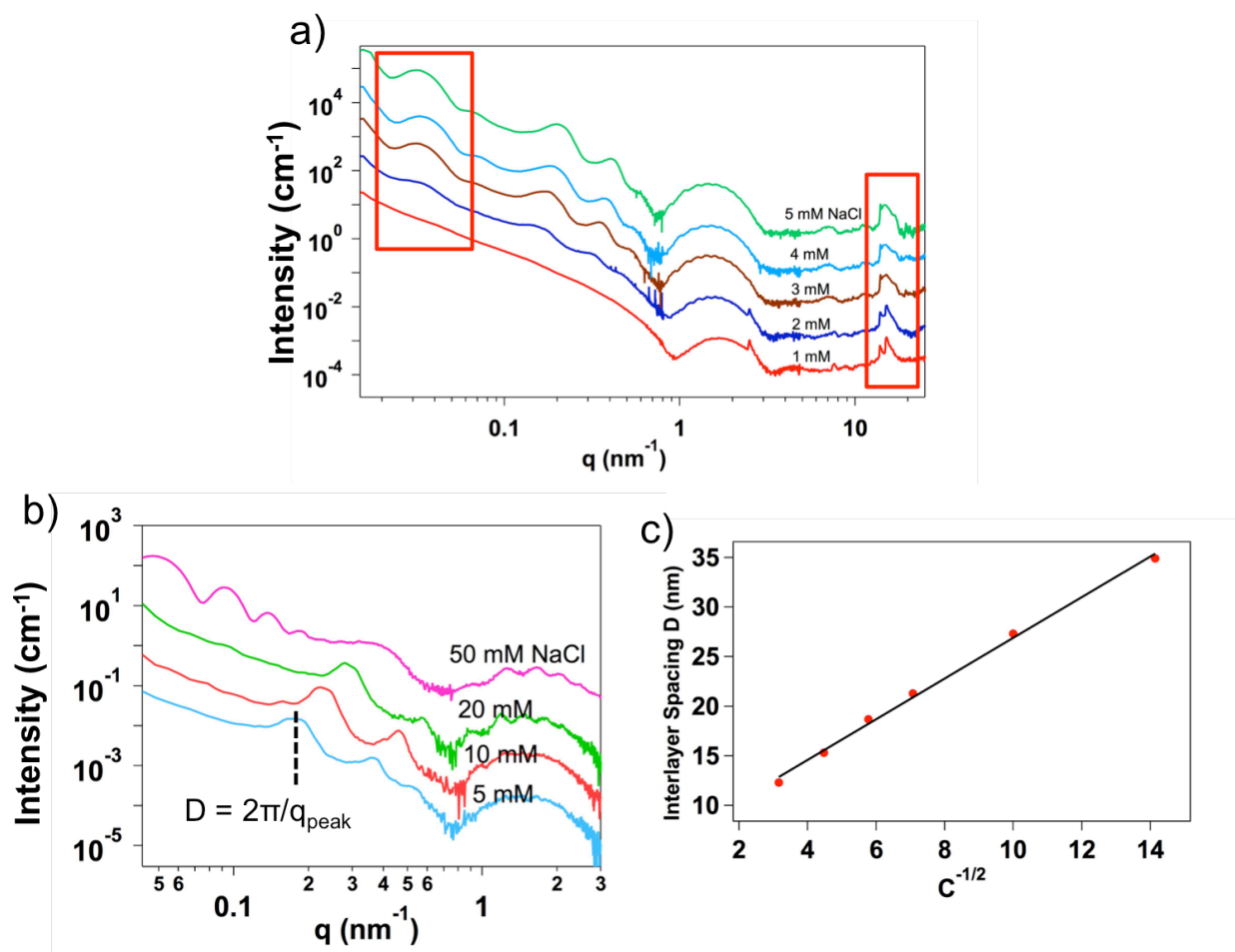


Figure 5.5. (a) Background subtracted *in situ* small- and wide-angle X-ray scattering data for 4 mM $C_{16}K_1$ as the solution NaCl concentration is increased from 1 to 5 mM. The data sets are

offset vertically for clarity. For NaCl concentration $c \geq 2$ mM, the appearance of multiple intensity modulations for $q < 0.1 \text{ nm}^{-1}$ and the reduction in the intensity of the sharp Bragg reflections in the WAXS regime are due to the ribbon-to-cochleate transition. (b) Background subtracted *in situ* small-angle X-ray scattering data for 4 mM C_{16}K_1 as the solution NaCl concentration is increased from 5 to 50 mM. The data sets are offset vertically for clarity. The position of first order small angle diffraction peaks ($0.1 < q < 1 \text{ nm}^{-1}$) is used to determine the interbilayer spacing D inside the cochleate. We note that the data in (a) and (b) are from different synthetic batches of C_{16}K_1 . Small deviations, for example, in the interbilayer spacing D were observed from batch to batch. The relationship between D and the NaCl concentration in the text and in (c) is based on the data in (b). (c) SAXS-derived interbilayer spacing of cochleate varies linearly as function of $c^{-1/2}$, where c is molar NaCl concentration. The solid black line is the best fit: $D \text{ (nm)} = 6.40 + 2.05 \times c^{-1/2}$.

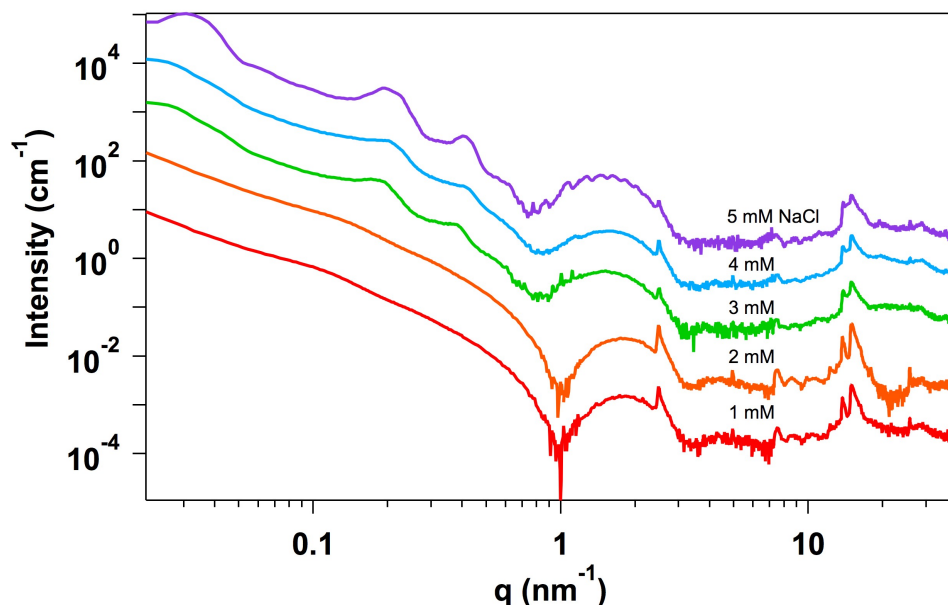


Figure 5.6. Background subtracted *in-situ* SAXS/WAXS intensity profiles of 10 mM $C_{16}K_1$ solution as the NaCl concentration is increased from 1 to 5 mM. The data sets are offset vertically for clarity. The data shows similar trends as the 4 mM $C_{16}K_1$ solution.

Figure 5.5a shows intensity modulations across the entire accessible q range of 0.02 to 30 nm^{-1} . These features can be divided into four groups, each yielding structural information at a different length scale about the cochleates. (1) The $0.02 < q < 0.06 \text{ nm}^{-1}$ modulation (Figure 5.5a, left red box) arises from the overall size; more specifically, from the cross-section of the cochleates. If we assume the overall shape of a cochleate to be a cylinder, then the scattering amplitude or the form factor $F_{cyl}(q) \propto \frac{J_1(qR)}{(qR)}$. Here, J_1 is the first order Bessel function of the first kind, and R is the cylinder radius. The first zero of $\frac{J_1(qR)}{(qR)}$ occurs at $qR = 3.8$. Therefore, the

minimum at $q \sim 0.022 \text{ nm}^{-1}$ yields an average cochleate radius $R = 3.8 / 0.022 \sim 173 \text{ nm}$, which is consistent with the TEM image of the cochleates in 5 mM NaCl (Figure 5.2e). (2) For $0.1 < q < 1 \text{ nm}^{-1}$, the positions of the intensity maxima follow the sequence $q_{max}: 2 \times q_{max}: 3 \times q_{max}$, implying that the intensity modulations in this q range are Bragg reflections due to periodic lamella within the cochleates. It can be seen from Figure 5.4a, and more clearly from Figure 5.4b that the position of the first maximum monotonically shifts to a higher q with increasing NaCl concentration (c). This shows that the interlamellar spacing $D = 2\pi/q_{max}$ continually decreases with increasing c . In fact, based on q_{max} for $0.005 \leq c \leq 0.1 \text{ M}$, $D \text{ (nm)} = 6.40 + 2.05 \times c^{-1/2}$ (Figure 5.4c). Therefore, for the range of NaCl concentration used, the interlamellar spacing could be continuously tuned from 13 to 35 nm. The intercept of 6.4 nm for infinite NaCl concentration may be interpreted as the sum of the thickness of a C_{16}K_1 bilayer (4.3 nm, *see below*) and an intervening 2.1 nm aqueous layer. The above relationship shows that the interlamellar spacing varies linearly with the electrostatic screening or the Debye length ($\lambda_D \propto c^{-1/2}$). Thus, the range of electrostatic interactions also controls the interlayer spacing. (3) As noted in the SAXS analysis of ribbons, the broad intensity modulation for $0.8 < q < 3 \text{ nm}^{-1}$ is due to an individual C_{16}K_1 bilayer. Fig. 4a shows that the minimum position at $q \sim 0.9 \text{ nm}^{-1}$ shifts to a lower q value when the ribbons are transformed into cochleates. This shift is observed up to NaCl concentration of 4 mM. Thereafter, the minima position is independent of NaCl concentration (Figure 5.4b). Based on SAXS fitting (not shown), the bilayer thickness increases from 4.0 nm (ribbon) to 4.3 nm (cochleate, at 4 mM NaCl), primarily due to a corresponding increase in the thickness of the hydrophobic tail region. This observation suggests that a curvature-induced strain in the cochleates reduces the extent of interdigitation between the

bilayer leaflets. (4) Finally, the curvature also induces a significant degree of disorder in the packing of $C_{16}K_1$ alkyl tails and headgroups. For the case of 4 mM $C_{16}K_1$, the sharp diffraction peaks corresponding to these crystalline ordering are completely smeared out for $c \geq 3$ mM. Qualitatively, similar behavior is observed for 10 mM $C_{16}K_1$ solutions. In this case, the integrated intensity for the sharp Bragg reflections at $q = 2.5 \text{ nm}^{-1}$ (headgroup ordering) and at $q = 13.9 \text{ nm}^{-1}$ (tail ordering) reduce by $\sim 67 \%$ and 50% , respectively, when the NaCl concentration is increased from 1 mM (ribbons) to 5 mM (cochleates). To summarize, the above X-ray scattering analysis reveals that above a threshold NaCl concentration of 2-3 mM, $C_{16}K_1$ assembles into cochleates of ~ 350 nm diameter. The interlayer spacing within these cochleates depends linearly on the electrostatic screening length, and that curved morphology of the cochleates induces a reduction in the interdigitation between the bilayer leaflets and the crystallinity in the molecular packing.

To qualitatively understand the origins of the observed structural changes in the ribbon to cochleate transition from the perspective of interplay between various intermolecular interactions, and membrane bending and interfacial energies, we develop simple theoretical models. Three aspects are focused upon: (1) The decrease in the ribbon aspect ratio with increasing salt concentration, (2) The origin of curvature in the membranes, and (3) the linear relationship between the interbilayer separation within the cochleates and the electrostatic screening length.

We first discuss the ribbon to sheet transformation. For this we model the membrane as a uniformly charged parallelepiped (Figure 5.7a), and formulate the membrane energy per unit volume as a sum of long-ranged electrostatic interaction energy and an interfacial energy term

that accounts for the direct exposure of hydrophobic tails to water on the membrane's side surfaces (eq. 5.1). Short ranged interactions such as intermolecular van der Waals' interactions are neglected because the contribution of these interactions to the areal or volume normalized energies is expected to be a constant. Furthermore, we assume that the area of the membrane is independent of the salt concentration. This assumption is justified based on AFM images in Figure 5.1b, where membranes with areas in the range $\sim 1\text{-}5 \mu\text{m}^2$ are observed, regardless of the salt concentration.

$$\frac{U_{electrostatic}+U_{surface}}{V} = 2 \left(\frac{N_T^2}{VA} \right) k_B T l_B \int_0^W \int_0^L \frac{e^{-\frac{\sqrt{x^2+y^2}}{\lambda_d}}}{\sqrt{x^2+y^2}} dx dy + \frac{2\gamma \left(\sqrt{A/\chi} + \sqrt{A\chi} \right)}{A} \quad (5.1)$$

In the above equation, A and V are the area and volume of the membrane, N_T is the total membrane charge, γ is the interfacial tension for the membrane side surfaces, l_B is the Bjerrum length, λ_d , as defined earlier, is the electrostatic screening length, which is proportional to $\sqrt{1/c}$, where c is the salt concentration, and $\chi = W/L$ is the inverse of membrane aspect ratio (Figure 5.7a). Numerical values of the fixed parameters: A , V , l_B , γ and N_T used in the equation 5.1 are presented in Table 5.1. Equation 5.1 shows that the interfacial energy term monotonically increases with increasing aspect ratio, whereas electrostatic energy can be formulated differently under low and high salt condition (See Eq. in *Appendix C*). Figure 5.7b shows that at low salt condition, the competition between electrostatic and interfacial energy leads to an equilibrium aspect ratio, which minimizes the membrane energy per unit volume, thus the equilibrium morphology of membrane is an elongated ribbon. By contrast, the electrostatic term becomes

independent of the aspect ratio at high salt condition, and the interfacial energy term drives the membrane to the lowest possible aspect ratio: $\chi = 1$ (Figure 5.7b).

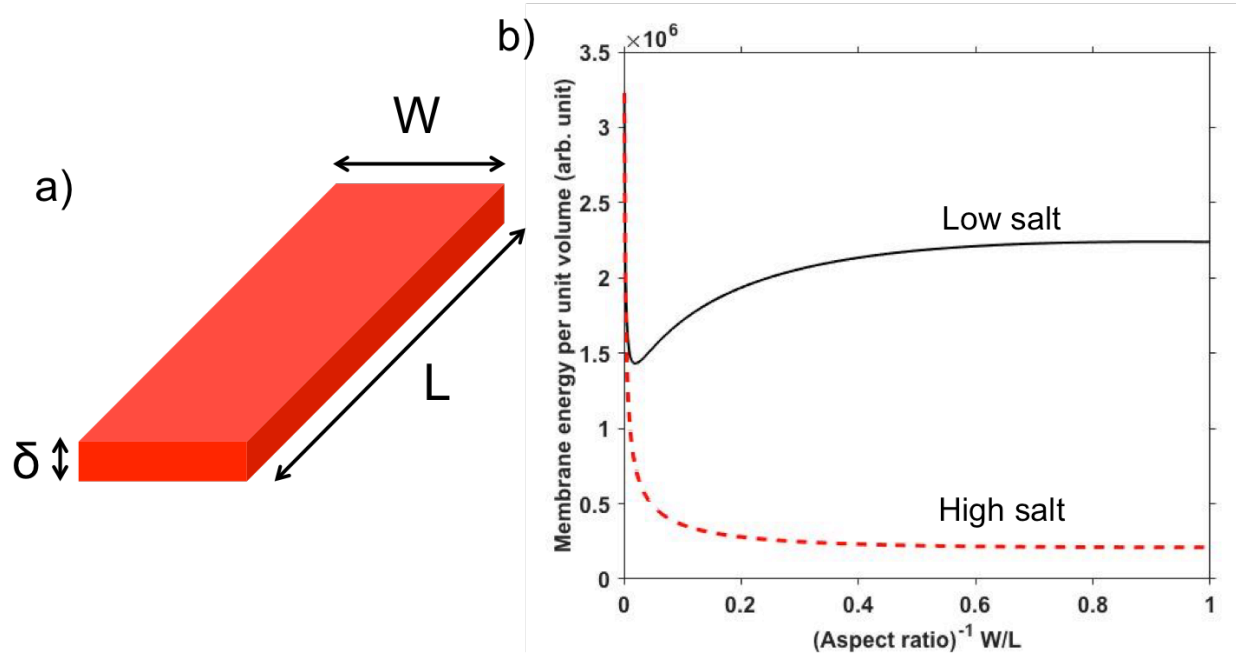


Figure 5.7. (a) Schematic representation of $C_{16}K_1$ nanoribbon showing ribbon dimensions used for the energy calculation. (b) The calculated membrane energy per unit area in equation 5.1 as a function of the inverse of membrane aspect ratio D_1/L for low salt and high salt conditions.

Table 5.1. Numerical values of parameters used in equation 5.1

Parameters	Values	Notes
Ribbon area A	$2 \times 10^{-12} \text{ m}^2$	Estimated from AFM image in Figure 5.1
Ribbon thickness δ	$4 \times 10^{-9} \text{ m}$	AFM (Figure 5.1) and SAXS (Figure 5.3)
Ribbon volume V	$A \times D_2 = 8 \times 10^{-21} \text{ m}^3$	
Membrane charge density ρ	$1.219 \times 10^{27} / \text{m}^3$	Estimated from WAXS results shown in Figure 5.3
Bjerrum length l_B	0.7 nm	
Membrane edge surface tension γ	$7.2 \times 10^{-2} \text{ J/m}^2$	Hydrocarbon-water interfacial energy[59]

Next, we consider the rolling of a flat membrane. This process involves a change in intermolecular electrostatic repulsion energy and the membrane elastic energy. When a thin membrane of a fixed perimeter length is bent, the intermolecular distances become shorter (Figure 5.8a). This increases the overall membrane electrostatic energy. Furthermore, unless the membrane has an intrinsic curvature, external work must also be done to bend the membrane. To test whether the $C_{16}K_1$ membranes possess an intrinsic curvature, we could refer to the self-assembly of $C_{16}K_1$ at elevated pH (= 10) by adding excessive NaOH. In chapter 4, we have shown that at pH 10, the majority of the $C_{16}K_1$ headgroups are deionized. Figure 4.4 shows that under these conditions, the equilibrium morphology of $C_{16}K_1$ assembly is a nanotube. Although counterintuitive, the above observation shows that the symmetric $C_{16}K_1$ bilayer has an intrinsic spontaneous curvature, and rolling of a flat membrane could in fact decrease the curvature energy. To further illustrate the membrane rolling, we use a simple model consisting of an array of charged species with pre-defined array length L_0 and an intrinsic spontaneous curvature C_0 ,

and calculate the total energy (electrostatic + curvature energy) as a function of curvature and salt concentration.

$$\frac{U_{electrostatic} + U_{curvature}}{L_0} = 2\rho^2 L_0 \int_{d_0}^{L_0} l_B \frac{e^{-\frac{2}{C_1} \sin(C_1 l/2)} \lambda_d}{\frac{2}{C_1} \sin(\frac{C_1 l}{2})} dl + \frac{\kappa_c}{2} L_0 (C_1 - C_0)^2 \quad (5.2)$$

In equation 5.2, ρ is the molecular density along the array, d_0 is the nearest neighbor intermolecular distance, κ_c is the membrane bending stiffness, C_l is the curvature of the array and C_0 is the intrinsic spontaneous curvature. For the limiting case of very high salt concentration ($\lambda_d \rightarrow 0$), equation 5.2 shows that the electrostatic energy term is negligible, and the resulting morphology would possess the intrinsic membrane curvature ($C_l = C_0$). To elaborate, we present results from calculations of total array energy as a function of curvature for four salt concentrations in Figure 5.8b. Numerical values for the fixed parameters (ρ , d_0 , C_0 , κ_c , L_0) are presented in Table 5.2. For the zero salt condition, the total energy increases with curvature (Figure 5.8b, top left). Therefore, the flat membrane is the equilibrium shape. As the salt concentration is increased, the total energy shows a minimum for an optimal curvature value, which continues to increase towards the intrinsic membrane curvature with increasing salt concentration.

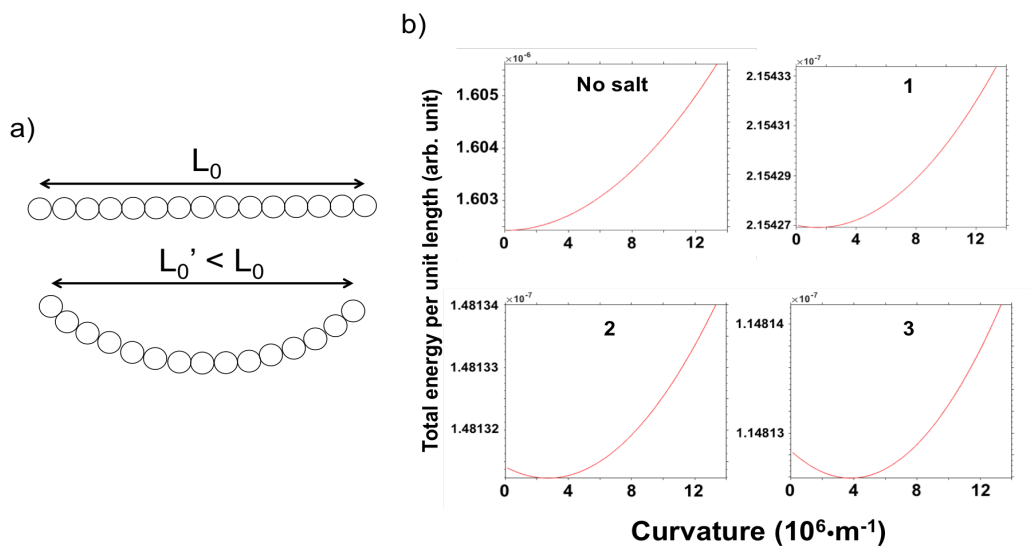


Figure 5.8. (a) An array of charged species with predefined array length L_0 and intrinsic spontaneous curve C_0 . This model is used to calculate the sum of electrostatic and curvature energy as a function of salt concentration and curvature. (b) Total energy per unit length in equation 5.2 versus array curvature C_l for different salt concentrations ($3 > 2 > 1 > \text{No salt}$).

Table 5.2. Numerical values of parameters used in equation 5.2

Parameters	Values	Notes
Molecular density along array: ρ	$2.438 \times 10^{11}/\text{m}$	Estimated from WAXS results shown in Figure 5.3
Bjerrum length l_B	0.7 nm	
Nearest intermolecular spacing d_0	5×10^{-10} m	Estimated from WAXS results shown in Figure 5.3
Length of the charged array L_0	5×10^{-8} m	A test value
Bending Stiffness κ_c	2×10^{-19} J	DPPC crystalline bilayer membrane stiffness[60]
Intrinsic curvature	$1/(75 \times 10^{-9}) \text{ m}^{-1}$	Cryo-TEM image Figure 4.4

Finally, we investigate the relation between interbilayer separation within the rolled-up C₁₆K₁ cochleate and salt concentration. We start with a theoretical model that is used to model the interactions in stacks of planar lipid bilayers. This model takes into account the interlayer van der Waals attraction, short-range hydration repulsion and electrostatic repulsion between charged lipid bilayer membranes in solution. Specifically, van der Waals attraction $U_d(\delta, d)$, hydration $U_h(d)$ and electrostatic repulsion energies per unit area are:

$$U_d(\delta, d) = -W \left[\frac{1}{d^2} - \frac{2}{(d+\delta)^2} + \frac{1}{(d+2\delta)^2} \right] \quad (5.3)$$

$$U_h(d) = H e^{-d/\Lambda_h} \quad (5.4)$$

$$U_e(d) = \frac{32\epsilon_0\epsilon_w(k_B T)^2}{q^2\lambda_d} \quad (5.5)$$

Here, δ is the bilayer thickness and d is the thickness of the aqueous layer between the bilayers (Figure 5.9a). Therefore, $\delta + d = D$, the interlayer spacing. W is the Hamaker constant, H is the hydration repulsion pressure, and Λ_h is the decay length for the hydration pressure (~ 0.2 nm). q is the electron charge, ϵ_0 is the vacuum permittivity, ϵ_w is the dielectric constant of the aqueous solution, and k_B is the Boltzmann constant.

Based on experimental results, the aqueous layer thickness d varies between ~ 31 and 9 nm when the salt concentration is varied between 5 and 100 mM. This thickness is much larger than decay length Λ_h . Therefore, the hydration energy term can be neglected in our theoretical model. The thickness d is also much larger than λ_d , which varies from 4.3 nm to 1 nm when c is

increased from 5 to 100 mM. Therefore, the use of the asymptotic form for the Debye-Hückel equation (equation 5.5) is valid.

In addition to the above energies in planar lipid bilayer stacks system, we also considered the curvature energy per unit area of cochleate spiral sheet, which turned out to be independent of interlayer spacing D . Therefore, equilibrium interlayer spacing D is calculated at different salt concentrations c by minimizing the total free energy (U_d+U_e) with respect to aqueous thickness d . The numerical values of all fixed parameters used in these calculations are summarized in Table 5.3, and Figure 5.9b shows that the theoretical derived relationship between D and c . Similar to the experiments, the theoretical model also predicts that D varies linearly with $c^{-1/2}$, but with a slope that is $2.5 \times$ larger than the experimentally determined slope for $C_{16}K_1$ cochleates. This deviation is likely a result of the assumption of planar membrane stacks, and maybe corrected by deriving the correct form of van der Waals' energy for a spiral sheet. Nevertheless, the above simplified theoretical model shows that the linear relationship between the interlayer separation and the electrostatic screening length is not a result of system specific design, but a result of interplay between interlayer van der Waals' and electrostatic energies. Therefore, it is not a surprise that this linear relationship has been observed in other charged lamellar system such as such as clay mineral montmorillonite.[61, 62] It should however, be noted that this linear relationship does not appear to be generally valid in the presence of salts with multivalent ions. For example, traditional negatively charged phospholipid cochleates show little or no dependence of interlayer spacing the concentration of $CaCl_2$.[63] It is possible that the multivalent cations are covalently linked to the molecules. As such the resulting electrostatic interactions cannot be parameterized by the screening length λ_d . By contrast, the use of

monovalent salts to induce the $C_{16}K_1$ cochleate structure leads to tunable interlayer spacing over $\sim 10 - 40$ nm. This structural feature may have potential application for controlled encapsulation and release of drug particles within specific size range.

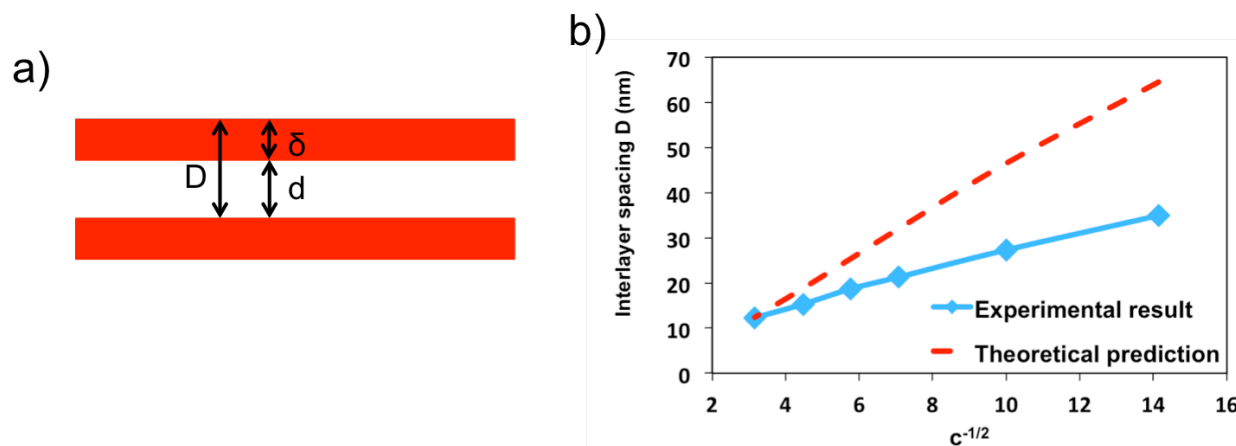


Figure 5.9. (a) The geometry of the lamellar stack. The thicknesses of the membrane and the interbilayer aqueous regions are δ and d , respectively. (b) Theoretical prediction showing a linear relation between interbilayer spacing $D = \delta + d$ and $c^{-1/2}$, where c is molar NaCl concentration. The deviation relative to experimental result is likely due to the assumption of a planar stack in calculations, as compared to the experimentally observed spiral geometry.

Table 5.3. Numerical values of parameters used in equation 5.3, 5.4 and 5.5

Parameter	Value	Notes
Hamaker constant: W	1.9×10^{-22} J	From ref. [64]
Temperature	298 K	Experimental
Bilayer thickness: δ	4×10^{-9} m	AFM (Figure 5.1) and SAXS (Figure 5.3)

5.4. Summary

We designed a peptide amphiphile molecule $C_{16}K_1$ to investigate the electrolyte-induced transformation of planar bilayers to a scroll-like cochleate morphology. Cryo-TEM, AFM and solution X-ray scattering were used to examine the assembly structures as a function of salt concentration. Our experiments show that with the addition of NaCl, the high aspect ratio $C_{16}K_1$ ribbons formed in zero salt conditions transform to isotropic sheets, prior to rolling upon themselves to form cochleates. Further addition of salt reduces, within the cochleates, the interbilayer separation, which scales linearly with the Debye length. Simplified theoretical models explain that the reduction in the range of electrostatic interactions is the driving force for high aspect ribbons \rightarrow isotropic sheets \rightarrow membrane rolling transformations. The linear relationship between the interbilayer separation and the screening length was qualitatively explained by considering the interplay between attractive van der Waals' and the repulsive electrostatic energies. These results suggest that the salt-induced structural transitions in the $C_{16}K_1$ system should also be observable in other charged bilayer membranes that possess a spontaneous curvature. Our combined experimental and theoretical study yields insight into attaining the cochleate structures and controlling their internal architecture. The results presented here should be useful for optimizing the structure and function of cochleates in many applications, including drug delivery and photocatalytic production of hydrogen.

Chapter 6. Thermodynamic Phase Behavior in Membranes of Binary Phospholipid Mixtures

6.1. Introduction

Mixtures of phospholipid molecules are common in naturally occurring cellular membrane[65] and artificial systems developed for drug-delivery[66, 67]. In those biological systems, lipid compositions strongly influence the membrane phase behaviors and corresponding membrane functions. Therefore, membranes consisting of lipid mixtures have been an attractive model system in biological research.[68-71] Previous studies on the coassembly of +3/-1[20] and +2/-1[21] cationic peptide amphiphile (PA) and fatty acid mixture have exhibited the rich morphologies of bilayer membranes as well as different crystalline structures within the bilayer. In this model system, electrostatic and van-der Waals attraction between the two components contributes to the tail crystallization, and the 2-D crystalline structure in the cationic bilayer is highly dependent on the degree of ionization and length of the carbon tail. Additionally, the local crystalline order of the amphiphile tails also acts to control the overall mesoscopic morphology of bilayers from closed faceted vesicles to bilayer ribbons. However, to understand the phase behavior of biological membranes from experimental model system, phospholipid molecules are better candidate to mimic the biological system than peptide amphiphile (PA) and fatty acid. Additionally, because of the low solubility of fatty acid and pH variation, the stoichiometric ratio of the cationic and anionic amphiphile composing the bilayers is unknown in the above PA/fatty acid system, so the charge distribution on the surface of the cationic membrane is also unclear.

As the electrostatic interactions between the amphiphiles have important effect in the membrane crystallization as well as the membrane phase behavior, it is important to design a system that we know the composition of cationic and anionic molecules within the membrane.

In this chapter, we focus on the bilayer systems of binary mixtures of phospholipid molecules that have headgroup charges of +1, 0, or -1 (Figure 6.1 and Table 6.1) under PBS buffer solution (pH ~ 7.4). Van der Waals interactions between the hydrophobic tails are kept constant by choosing molecules with the same aliphatic tails. First of all, we will illustrate how the gel (crystalline) to fluid (non-crystalline) transition temperature in phospholipid bilayer membrane depends upon the lipid composition, which reflects the contribution of headgroup electrostatic interactions to stabilizing the crystalline phase bilayer. Gel to fluid phase transition temperature of phospholipid bilayers could be determined from *in situ* SAXS/WAXS experiments at different temperatures. Moreover, by analyzing the WAXS diffraction peaks as a function of temperature and lipid composition, we can also investigate the thermal expansion behavior of 2D lattice, as well as the effect of headgroup electrostatic interactions on the intermolecular spacing within the crystalline phase bilayer.

6.2 Materials and Methods

6.2.1. Sample Preparation

DMPS (-1), DMPC (0), DMTAP (+1) were purchased from Avanti Polar Lipids, Inc. The phospholipid molecules are originally stored in chloroform solvent. To prepare the lipid binary

mixtures in aqueous solution, the original solution of two lipid components were taken through syringes and mixed into a glass vial. The volume of each lipid solution was calculated based on the original concentration and the mixing ratio. After mixing the original solutions, we blow dried the chloroform solvent using N₂ gas gun and placed the glass vial inside the vacuum chamber overnight to completely remove the remaining solvents. The dried lipid powders were then dissolved in standard PBS buffer solution (137 mM NaCl, 2.7 mM KCl, and 10 mM PO₄³⁻) to the total concentration of 10 mM. Based on previous studies, these phospholipid dispersions are expected to consist of multi-lamellar vesicles, which can be transformed to unilamellar vesicles via a sonication at high power with a titanium tip. Subsequently, the lipid solution was centrifuged at 10000 rpm for 10 min to remove the suspended Ti particles from the tip sonicator.

6.2.2. Characterization Methods

SAXS/WAXS were used to study the assembly structure of binary lipid mixture as function of temperature and lipid composition. Differential scanning calorimetry (DSC) measurements were performed to verify the WAXS-derived melting temperature of lipid bilayer. Cryogenic transmission electron microscopy (Cryo-TEM) imaging was used to study the morphology of bilayer membrane. The PBS buffer was diluted 10 times for better imaging. Dynamic light scattering (DLS) was also used to measure the size distribution of spherical bilayer vesicles. Detailed experimental setups are discussed in Chapter 3.

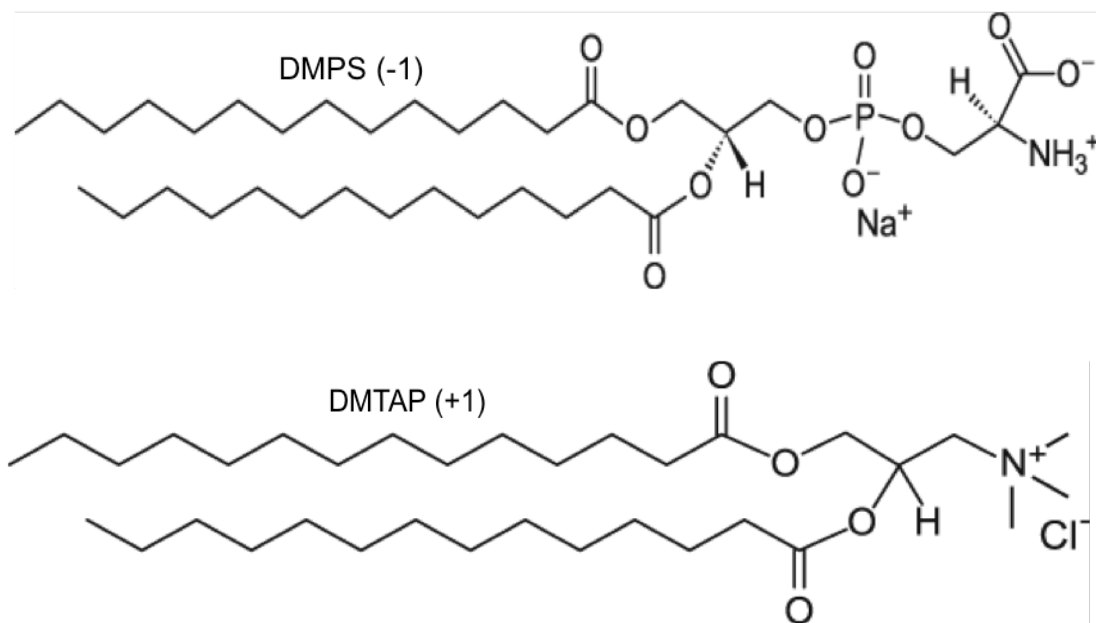
6.3. Results and Discussion

Different compositions of lipid binary mixtures with charge ratios of DMTAP (+1)/DMPS (-1) and DMTAP (+1)/DMPC (0) were studied (Table 6.1). In this two binary mixture systems, van der Waals attraction between the hydrocarbon tails are kept constant, and the electrostatic attraction between the catanionic lipids (eg. DMTAP (+1)/DMPS (-1) binary mixture) can be systematically tuned through lipid composition. When mixture of +1 charged lipid (DMTAP) and -1 charged lipid (DMPS) reaches the composition of 50%/50%, significant amount of precipitates form in the lipid solution due to the strong aggregation of the assemblies, therefore the data point from this composition is missing in this experiment. Lipid mixtures of all other compositions form clear and stable solutions ideal for SAXS/WAXS and TEM experiments. Figure 6.2 shows the SAXS/WAXS intensity profiles of pure DMPS (-1) solution as function of temperature. This figure exhibits several general observations about the temperature dependent structural evolution of lipid bilayers, which are also found in other lipid compositions. First of all, WAXS diffraction peaks are observed at low temperature in gel phase whereas no diffraction peaks are present at high temperature in fluid phase. Therefore we can determine the lipid bilayer transition temperature from *in situ* X-ray scattering measurements, with temperature ramping step of 2~5°C. For example, the WAXS region of pure DMPS (-1) bilayer has diffraction peak at 37 °C, but no diffraction peak at 39 °C, which indicates that the gel to fluid phase transition temperature of pure DMPS (-1) bilayer is between 37 and 39 °C. A higher resolution measurement of transition temperature using DSC is conducted as complementary experiment. In Figure 6.3, the DSC scan exhibit the gel to fluid transition peak at 37.5 °C, which validate our method of using *in situ* X-ray scattering to determine the transition temperature.

Figure 6.4 shows the WAXS-derived gel-fluid phase diagram as a function of lipid composition and temperature. For both DMTAP (+1)/DMPS (-1) and DMTAP (+1)/DMPC (0) mixture type, the lipid composition dependent fluid-gel phase boundary exhibits inverted parabolas with the highest transition temperature close to 50%/50% mixture. The result from DMTAP (+1)/DMPS (-1) mixture is consistent with the physical intuition that attractive electrostatic interaction between the cationic lipid headgroups stabilizes the gel-phase bilayer. For DMTAP (+1)/DMPC (0) mixture, the headgroup interaction should be a combination of electrostatic repulsion and attraction since the PC headgroup is zwitterionic. Previous experimental studies in DMTAP/DMPC monolayer system have shown that the net headgroup electrostatic interaction between PC and TAP headgroup is still attractive because of the reorientation of zwitterionic PC headgroup in gel phase, which bring the positive charged quaternary amine on TAP and negative charged phosphate on PC into close proximity.[70] Temperature renormalization of the asymmetric phase diagram is required to compare the effect of headgroup electrostatic attraction in DMTAP (+1)/DMPS (-1) with DMTAP (+1)/DMPC (0) systems on gel-to-fluid phase transition temperature. Additionally, to further explore the effect of headgroup electrostatic attraction on bilayer phase behavior, we can study the like-charged binary lipid mixture (eg. DMPG (-1) and DMPA (-1)) in a same manner and compare its phase diagram with DMTAP (+1)/DMPC (0) and DMTAP (+1)/DMPS (-1) mixture.

Table 6.1. Selected compositions of lipid binary mixtures for SAXS/WAXS studies

DMPS (-1) and DMTAP (+1) mixture	DMPC (0) and DMTAP (+1) mixture
100% DMPS	100% DMPC
90% DMPS + 10% DMTAP	90% DMPC + 10% DMTAP
70% DMPS + 30% DMTAP	70% DMPC + 30% DMTAP
50% DMPS + 50% DMTAP (precipitate)	50% DMPC + 50% DMTAP
30% DMPS + 70% DMTAP	30% DMPC + 70% DMTAP
100% DMTAP	10% DMPC + 90% DMTAP
	100% DMTAP



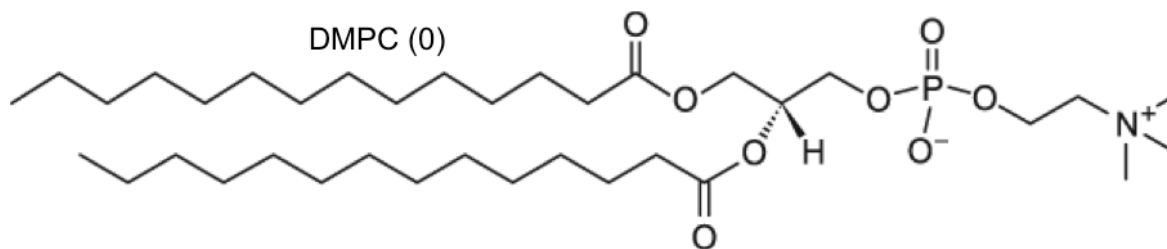


Figure 6.1. Molecular structures of phospholipids DMPS (-1), DMPC (0), and DMTAP (+1) described in Table 1

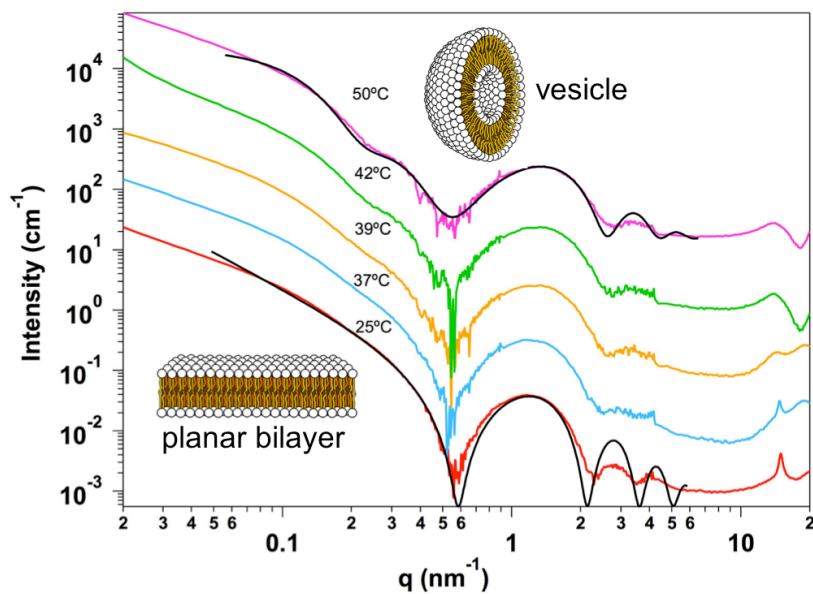


Figure 6.2. *In situ* small- and wide-angle X-ray scattering data showing background subtracted scattered intensity profiles for pure DMPS lipid bilayers as function of temperature. The data sets are offset vertically for clarity. The solid black curves are the best fits of SAXS data at 25 °C and 50 °C using planar bilayer and vesicle models, respectively. The WAXS diffraction peak at $q = 15 \text{ nm}^{-1}$ represents the crystalline order of gel-phase lipid bilayer.

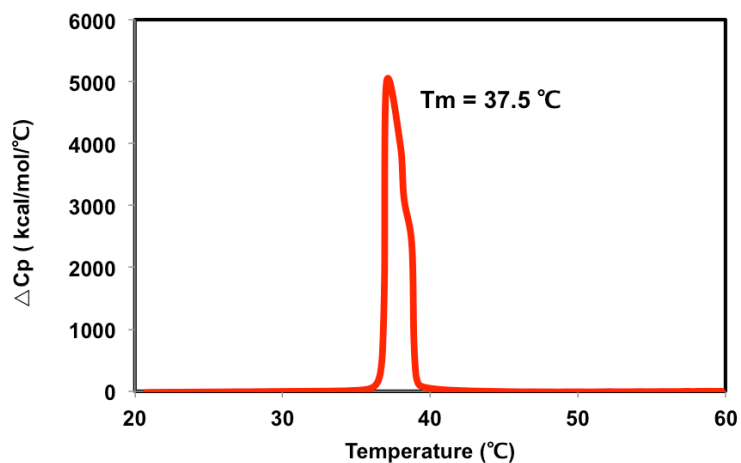


Figure 6.3. Differential Scanning Calorimetry (DSC) measurement for solution of pure DMPS lipid bilayers, shows the gel-to-fluid phase transition temperature at 37.5°C.

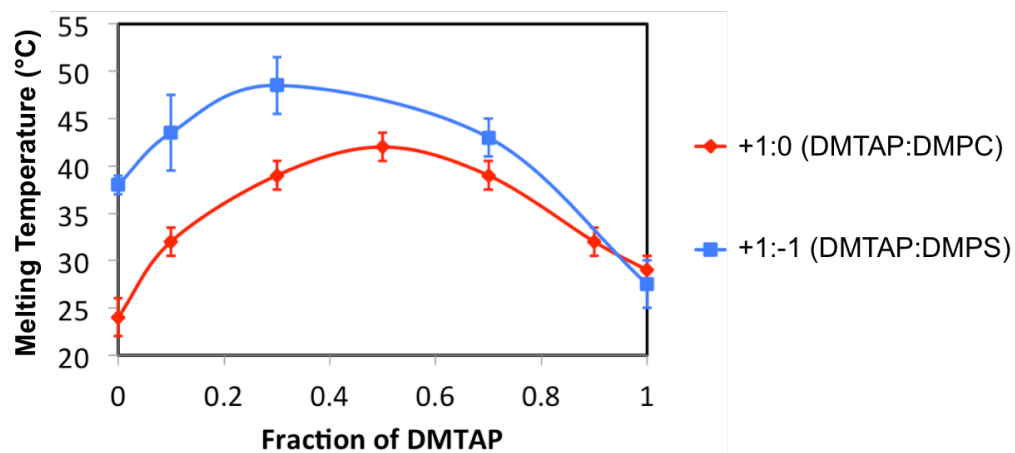


Figure 6.4. WAXS-derived gel-to-fluid transition temperature vs. composition for DMTAP (+1)/DMPS (-1) and DMTAP (+1)/DMPC (0) binary lipid mixtures showing inverted parabolas

with highest melting temperature close to 50%/50% mixture. The error bar of each data point is from the temperature step size (3 to 5 °C) of *in situ* X-ray scattering measurements.

The second observation in Figure 6.2 is the big oscillation of SAXS intensity profile between 0.5 and 2 nm⁻¹, associated with the lipid bilayer form factor. At low temperature in gel phase, we can successfully fit the SAXS intensity profile using the planar bilayer model (black line). In the fitting, the electron density of the hydrophobic tail is set to be 95% the electron density of water ($0.95 \times 334 \text{ e}^-/\text{nm}^3 = 317 \text{ e}^-/\text{nm}^3$), because of the crystalline packing. The fitting result shows that C₁₄ tail length in gel phase is 1.88 ± 0.16 nm. When the temperature increase to the fluid phase, the big oscillations at SAXS region still persist while a small hump appears around $q = 0.3 \text{ nm}^{-1}$, which is expected to be the bilayer vesicle formation because of the increase in membrane fluidity. As expected, cryo-TEM image of DMPS solution at 50°C (Figure 6.5) exhibited spherical vesicle structures with diameters around 20 to 50 nm. Therefore, we utilize a vesicle model to fit the SAXS intensity profile. Here we set the electron density of the hydrophobic tail to be 85% the electron density of water ($0.85 \times 334 \text{ e}^-/\text{nm}^3 = 284 \text{ e}^-/\text{nm}^3$) due to the fluidity of tail packing. The fitting results show that the C₁₄ tail length is 1.39 ± 0.22 nm in fluid phase, which is physically reasonable since the carbon tail in gel phase is more rigid and stretched than the tail in fluid phase. The fitting results also yield that the averaged diameter of the lipid vesicle is 26.7 ± 1.2 nm, with polydispersity of 0.35. These are also highly consistent with the vesicle size distribution result obtained through dynamic light scattering (Figure 6.6). The size distribution shows that the number-averaged vesicle diameter is 27.0 nm, with

polydispersity of 0.33. This unilamellar spherical vesicle structures have also been observed in other lipid mixtures such as 90% DMPS + 10% DMTAP. Possible future studies could focus on the variation of vesicle structures as function of phospholipid compositions.

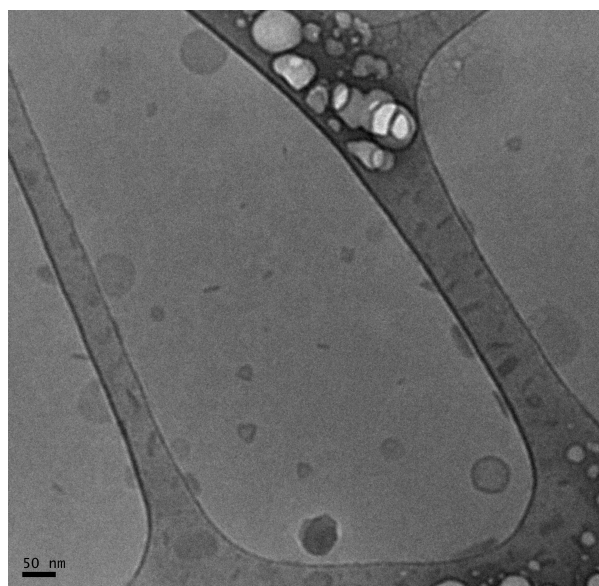


Figure 6.5. Cryo-TEM image of DMPS vesicles formed at 50°C, which is above DMPS transition temperature (~38°C). The size of vesicle in this image ranges between 20 and 50 nm.

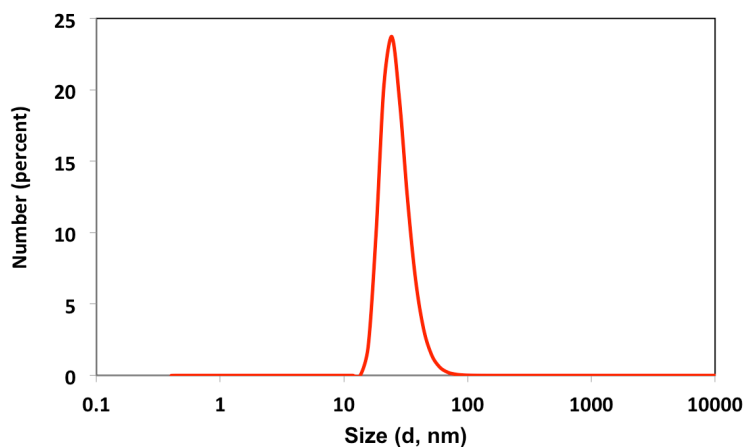


Figure 6.6. DMPS vesicle size distribution determined from Dynamic Light Scattering (DLS). The number-averaged diameter of vesicle is measured to be 27.0 nm, and polydispersity of size distribution is 0.33. Those values are highly consistent with SAXS fitting result.

The WAXS data for gel phase lipid bilayers shows that all binary mixtures are packed into single hexagonal lattice system, indicating that DMPS (-1), DMTAP (+1) and DMPC (0) phospholipids are completely miscible to form a homogeneous membrane. In addition, the WAXS peak position slightly shifts to lower q as the temperature increases, which reflects the thermal expansion behavior of the lipid bilayer lattice. The hexagonal lattice constants can be obtained using Bragg's law. Figure 6.7 exhibits the lattice parameters vs. temperature curves for both DMTAP (+1)/DMPS (-1) and DMTAP (+1)/DMPC (0) lipid mixtures. For both mixture systems, we observed similar trend of these curves showing almost linear relation to the temperature, indicating a “universal” thermal expansion behavior of the lipid bilayer lattice regardless of phospholipid compositions. Furthermore, we also noticed that at the same

temperature, pure DMPC, DMPS, DMTAP lipid bilayers have higher intermolecular spacing than their corresponding mixtures, and the nearest intermolecular spacing can be observed around 50%/50% mixture (Figure 6.8a). Again for DMPS (-1)/DMTAP (+1) mixture, this could be attributed to the strong electrostatic attraction between the two lipid components, which bring the lipid molecules in closer proximity to increase the gel phase stability. For DMPC (0)/DMTAP (+1) lipid bilayer, the molecular dynamics study by Gurtovenko et al. has shown a very similar relation between the area per lipid and the lipid composition, with a pronounced minimum area per lipid at roughly 50%/50% mixture (Figure 6.8b).[71] In this study, the author considered the reorientation of zwitterionic PC headgroup and proposed a schematic picture to explain the observed changes in the intermolecular spacing (Figure 6.8c). In this picture, we can see that the reorientation of PC headgroup as a function of DMTAP molar fraction is directed to maximize the headgroup electrostatic attraction. To further understand the role of headgroup electrostatic interaction in determining the 2D crystalline lattice constant, binary lipid mixture of like charge (eg. DMPG (-1) and DMPA (-1)) could be studied in a same manner, and compared with DMTAP (+1)/DMPC (0) and DMTAP (+1)/DMPS (-1) mixture. We speculate that -1/-1 mixture would not show the minimum lattice constant as a function of mixing ratio. Instead, -1/-1 mixture would be more likely to follow Vegard's law, where the lattice constant of mixture is equal to the linear combination of the lattice constants in pure constituents.

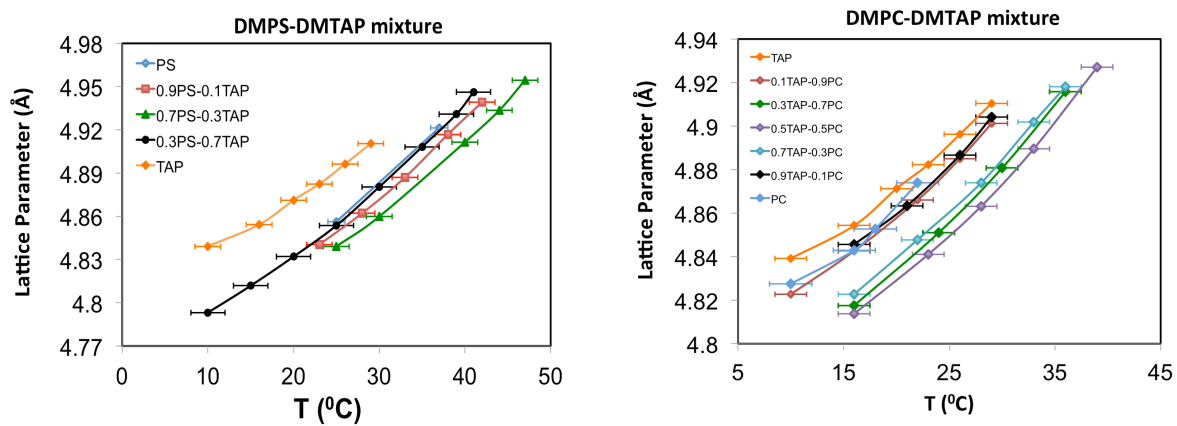


Figure 6.7. Lattice parameter of DMPS (-1)/DMTAP (+1) and DMPC (0)/DMTAP (+1) gel phase lipid bilayers as a function of temperature

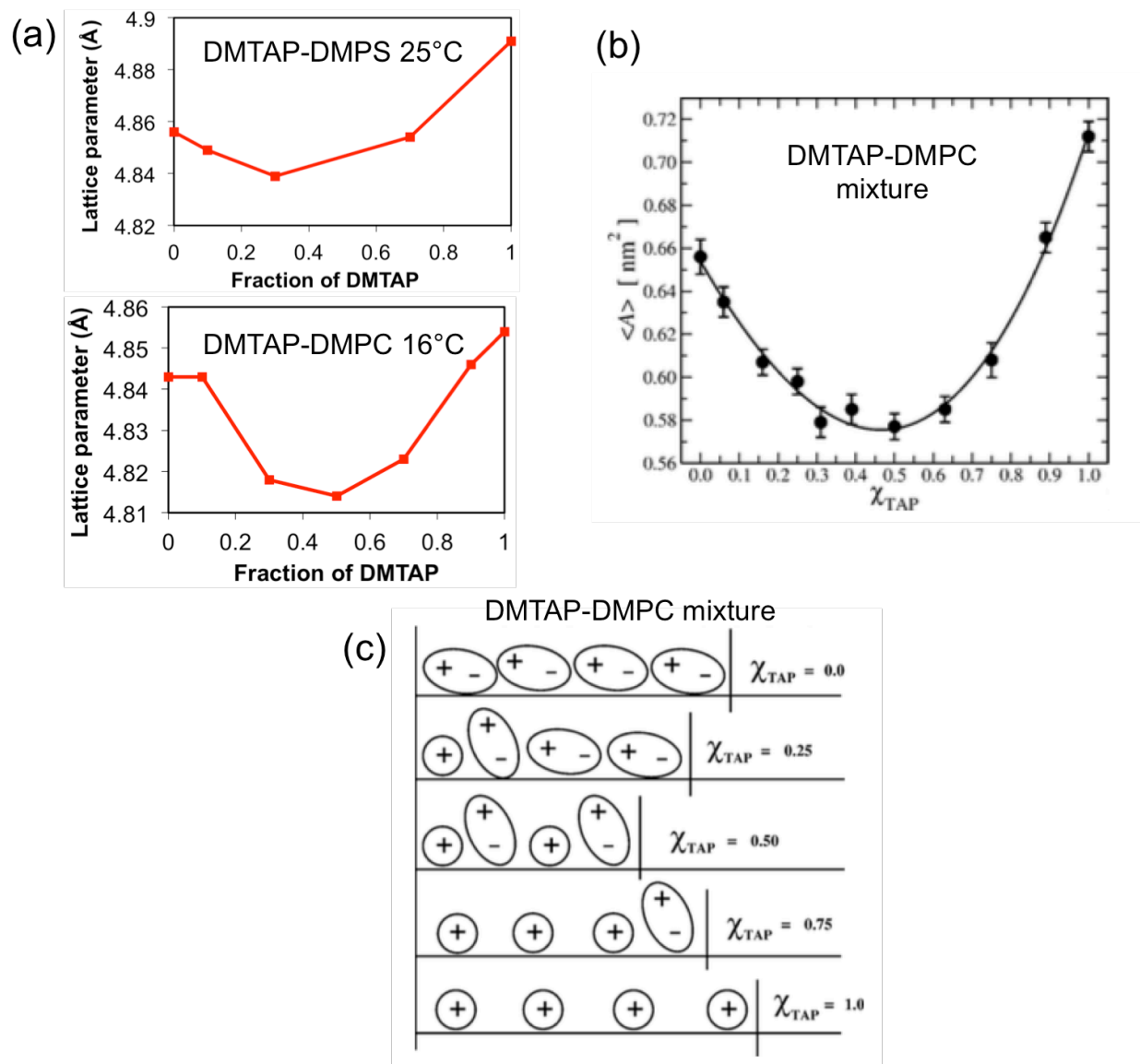


Figure 6.8. (a) Lattice parameter of DMPS (-1)/DMTAP (+1) and DMPC (0)/DMTAP (+1) lipid bilayer as a function of lipid composition under the fixed temperature. The lattice parameter values are determined from Figure 6.7. (b) Average area per lipid $\langle A \rangle$ as a function of the composition χ_{TAP} in DMTAP (0)/DMTAP (+1) lipid bilayer. (c) A proposed schematic picture of

the observed change in the area per lipid versus lipid composition χ_{TAP} . Only headgroups of the lipids are shown here.

6.4. Summary

We successfully used SAXS/WAXS to determine the nanostructures and transition temperatures of lipid bilayers consisting of DMTAP (+1)/DMPS (-1) and DMTAP (+1)/DMPC (0) binary mixture. A gel-to-fluid phase diagram is established as function of temperature and lipid composition, exhibiting the highest transition temperature for the mixture with composition of 50%/50%, where the electrostatic attraction between the two lipid components are maximized. Furthermore, the lattice constants of 2D crystalline structure as function of temperature show universal thermal expansion behavior, and we also observed that the headgroup electrostatic attraction could decrease the intermolecular spacing in lipid bilayer membrane. Further studies should focus on the bilayer with binary lipid mixture of like charge (eg. DMPG (-1) and DMPA (-1)), and compare the phase behavior and lattice constant variation with DMTAP (+1)/DMPS (-1) and DMTAP (+1)/DMPC (0) system.

Chapter 7. Summary and Outlook

7.1. Summary

In this thesis, we have designed several amphiphilic molecular assembly systems where the electrostatic interaction controls the structural transformation at different length scales, including mesoscopic assembly morphologies and the angstrom scale intermolecular packing. Electrostatic interaction in those assembly systems can be systematically tuned by varying the solution parameters or amphiphile mixture compositions. Therefore, it allows us to quantitatively understand the correlation between intermolecular electrostatic interaction and equilibrium structure, and explore the possibility of precisely control the assembly structures for various applications. For instance, $C_{16}K_n$ model system exhibits a rich diversity of assembly structures such as spherical micelles, cylindrical micelles, planar bilayers and nanotubes. pH and peptide headgroup size are the two major parameters that vary the intermolecular electrostatic and steric repulsion in this $C_{16}K_n$ model system. As the molecular charge and headgroup size decreases, the peptide amphiphile assembly transitions from loosely packed into densely packed assemblies such as crystalline bilayer. In addition, the crystalline bilayers formed by $C_{16}K_n$ peptide amphiphiles take the interdigitated configuration, which maximize the intermolecular van der Waals attraction as well as accommodate the steric constraints of the large ionic headgroup.

From $C_{16}K_n$ model system, we observed a peptide amphiphile molecule $C_{16}K_1$ with ability to self-assemble into high aspect-ratio flat nanoribbons even when the molecule is fully ionized.

Our experiments show that with the addition of NaCl to screen the electrostatic interaction, the high aspect-ratio $C_{16}K_1$ ribbons transform to isotropic sheets, prior to rolling upon themselves to form cochleates. Further addition of salt reduces, within the cochleates, the interbilayer separation, which scales linearly with the Debye length. Simplified theoretical models are built to explain that the reduction in the range of electrostatic interactions is the driving force for high aspect ribbons \rightarrow isotropic sheets \rightarrow membrane rolling transformations, as well as the linear relationship between the interbilayer separation and the screening length. Our combined experimental and theoretical study yields insight into attaining the cochleate structures and controlling their internal architecture. The ability to adjust the interbilayer separation within the cochleate will be useful in drug delivery systems for controlled encapsulation and release of drug particles within specific size range.

In addition to unary peptide amphiphile model system, we also successfully determined the nanostructures and gel-to-fluid phase transition temperatures of lipid bilayers consisting of DMTAP (+1)/DMPS (-1) and DMTAP (+1)/DMPC (0) binary mixture. A gel-to-fluid phase diagram is established as function of temperature and lipid composition. It exhibit that 50%/50% mixture of both DMTAP (+1)/DMPS (-1) and DMTAP (+1)/DMPC (0) binary mixtures has the highest gel-to-fluid transition temperature. Therefore, we can deduce that headgroup electrostatic attraction could stabilize the gel phase lipid bilayer. Furthermore, the lattice constants of 2D crystalline bilayer are also dependent on temperature and lipid mixing ratios. The adjustable intermolecular spacing could also be useful in drug delivery system and also understanding diffusion behavior of membrane in response to temperature and lipid composition variation.

7.2 Outlook

7.2.1. Cochleate Encapsulation Ability

In the studies of $C_{16}K_1$ ribbon-to-cochleate transition, we propose the possibility to explore the controlled encapsulation ability of those formed cochleates. In this system, the encapsulated object can be large protein or drug loaded nanoparticle, which can be stored at the interlayer regions within the cochleate. The encapsulation efficiency can be tested as a function of the particle size as well as the salt concentration. The analytical method has been reported to determine the lipid vesicle encapsulation efficiency.[72] Fluorescence microscopy and Cryogenic transmission electron microscopy could also be applied to image the drug encapsulated $C_{16}K_1$ cochleates. These results can provide us the insight about the ability of the $C_{16}K_1$ cochleate in encapsulating drug or protein particles within specific size range.

7.2.2. $C_{16}K_1$ Membrane Intrinsic Curvature

The intrinsic curvature of $C_{16}K_1$ membrane has been exhibited by the nanotube formation when the solution pH is increased to reduce the charge on headgroup, and also exhibited by the spiral cochleate formation when the salt concentration is increased to screen the intermolecular electrostatic repulsion. However the origin of the intrinsic curvature in $C_{16}K_1$ bilayer membrane is not well understood. Theoretical studies have developed models based on molecular chirality to explain the curvatures observed in helical ribbons and tubules.[73, 74] It was stated that the chiral molecules tend to pack at a slight angle with respect to their neighbors, and this twisted molecular packing could lead to the macroscopic curvatures of the membrane. In addition, experiments on a wide variety of tubule systems have shown that the helical markings on the

tubules exhibit a single sense of handedness related to the molecular chirality. Interestingly, our $C_{16}K_1$ cochleates also exhibit right-handed only spiral marks on the cochleate surface (Figure 7.1), and $C_{16}K_1$ molecule used in this thesis has only one chiral center and it possesses the pure ‘S’ configuration. Future experimental work could focus on the cochleate assembly of ‘R’ configuration $C_{16}K_1$ and compare the handedness of spiral cochleate with the ‘S’ configuration. If the membrane curvature originates from the molecular chirality, we should expect the formation of pure left-handed spiral edges on the ‘R’ configuration $C_{16}K_1$ cochleate.

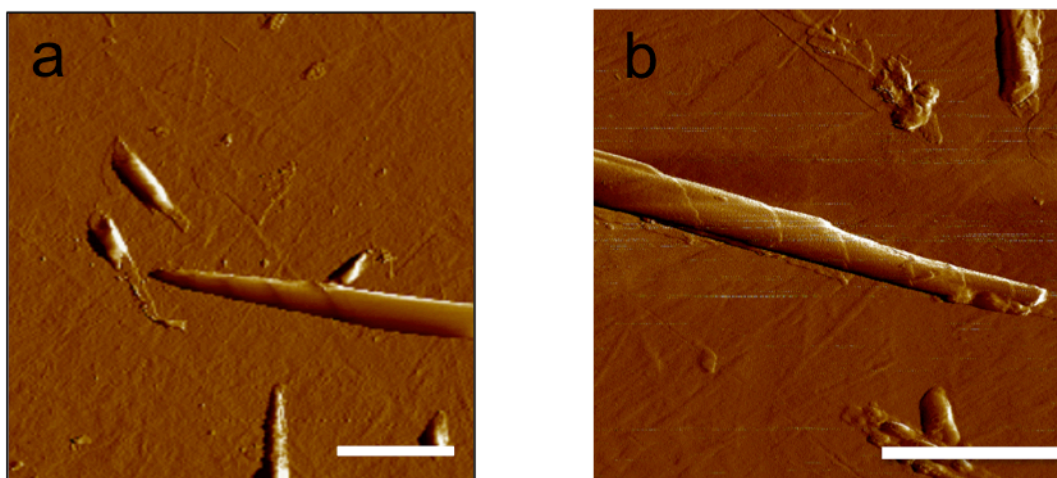


Figure 7.1. AFM Peakforce images showing right-handed spiral marks on $C_{16}K_1$ cochleate structure. The scale bars in both image a and b represent 2 μm .

Appendix

Appendix A. Alignment of C₁₆K₁ Nanoribbons Under Shear Flow

A.1. Anisotropic SAXS Pattern Induced by Nanoribbon Alignment

In Chapter 5, we discussed the high aspect ratio nanoribbon structure self-assembled by C₁₆K₁ peptide amphiphile. During the in-situ small-angle X-ray scattering (SAXS) experiments of C₁₆K₁ nanoribbons under the flow condition, we also observed that 2D SAXS pattern exhibits anisotropic scattered intensity distribution along different azimuthal angles (Figure A.1a), with stronger intensity distributed along the direction perpendicular to the flow direction in the capillary flow cell (Figure A.1c). By contrast, when solution pH increases, the 2D SAXS pattern turns into isotropic pattern (Figure A.1b) as the long nanoribbons transform into short nanotubes (Figure 4.4). Additionally, the 2D SAXS pattern of nanoribbons is less anisotropic when the flow is disabled in the capillary flow cell. These observations strongly indicate that the high aspect ratio C₁₆K₁ nanoribbons are highly oriented along the flow direction, which gives rise to the anisotropic SAXS pattern.

The alignment induced anisotropy in SAXS pattern has also been reported in flowing stream of long cylindrical micelles in a microchannel.[75, 76] In these studies, the orientational distribution of the cylinders can be determined from the scattering patterns through

$$I(q_x, q_y) = \int_0^{\pi/2} \int_0^{2\pi} P(q, \delta, \chi) h(\delta) d\chi d\delta \quad (\text{A.1})$$

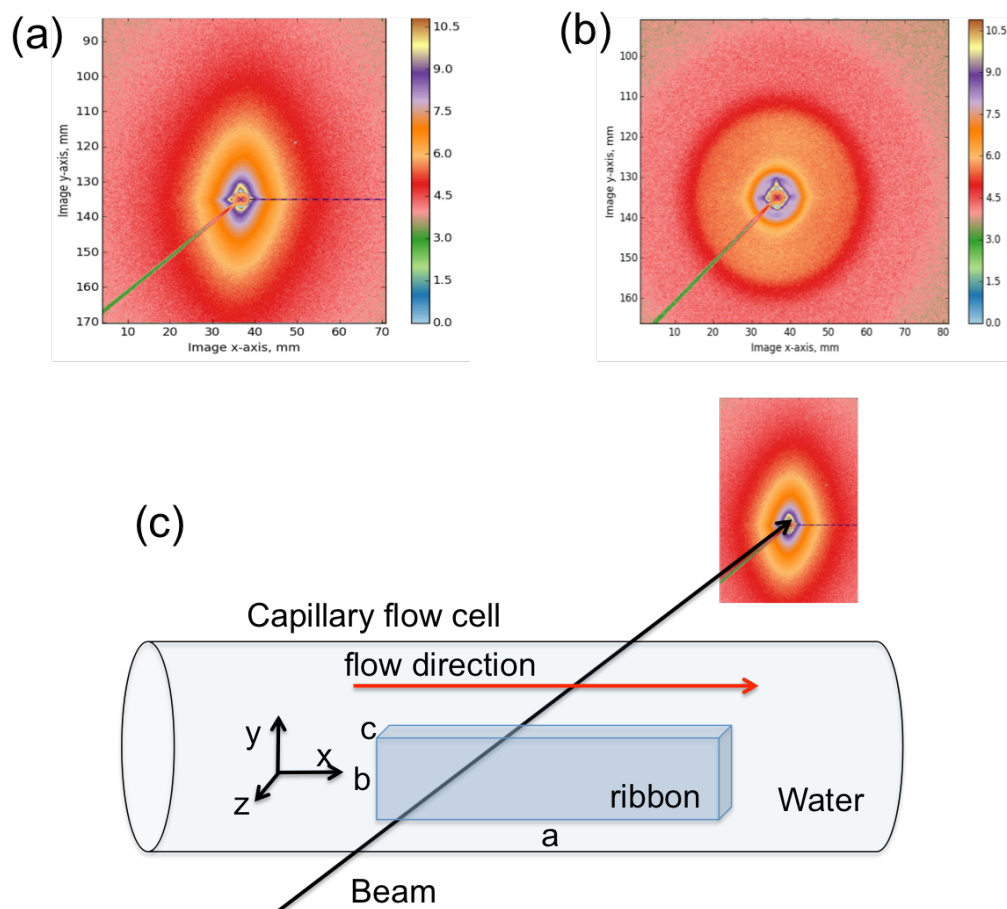


Figure A.1. (a) 2D SAXS pattern of $C_{16}K_1$ nanoribbon formed at pH 4.6 showing anisotropic shape. (b) 2D SAXS pattern of $C_{16}K_1$ nanotube formed at pH 10 showing isotropic shape. (c) Schematic representation of *in situ* SAXS measurement of $C_{16}K_1$ nanoribbon aligned in the capillary flow cell. The alignment of the nanoribbons leads to the anisotropic SAXS pattern.

In equation (A.1), $h(\delta)$ is the fraction of cylinders with a deviation angle δ between the cylinder axis and shear direction. The vectors describing the cylinder orientation are located on a cone having its central axis in the shear direction. The cylinder orientation is then completely determined by the rotation angle χ on the cone. From the angles (δ, χ) and the form factor of ideally aligned cylindrical micelle $P(q)$, the form factor of the cylinder $P(q, \delta, \chi)$ at different orientational angles can be computed. In our $C_{16}K_1$ nanoribbon system, we can also derive the orientational distribution of the nanoribbon using the same method. The form factor of ideally aligned nanoribbon shown in Figure A.1c can be formulated as

$$P(q) = (\rho_{\text{ribbon}} - \rho_{\text{wat}}) \times a \times b \times c \times \frac{\sin(q_x \frac{a}{2})}{q_x \frac{a}{2}} \times \frac{\sin(q_y \frac{b}{2})}{q_y \frac{b}{2}} \times \frac{\sin(q_z \frac{c}{2})}{q_z \frac{c}{2}} \quad (\text{A.2})$$

The parameters a , b and c in above equation is the nanoribbon length, width and thickness. Based on the experimental results discussed in Chapter 5, we set the ribbon length to be 10 μm , width to be 1 μm , and thickness to be 4 nm. The electron density of the ribbon ρ_{ribbon} is set to 350 e^-/nm^3 , and the electron density of water is 334 e^-/nm^3 .

As the orientational distribution function $h(\delta)$ is *a priori* unknown. Different functional forms such as Boltzmann ($\exp[-\delta/n]$), Gaussian ($\exp[-\delta^2/n]$), and Onsager distribution ($\exp[-\sin(\delta/n)]$) functions are investigated. Figure A.2 shows the simulated 2D SAXS patterns using different distributions, within which Boltzmann and Onsager distributions lead to similar elliptical SAXS pattern in Figure A.1a. The studies on the flow-induced alignment of cylindrical micelle also stated that Onsager distribution gives the best agreement between calculated and experimental scattering pattern[75, 76], which gives hint that nanoribbons may behave similarly

as cylindrical micelles under the shear flow. To further explore the orientational distribution of $C_{16}K_1$ nanoribbons, future work should focus on obtaining real-space images (i.e. polarized optical microscopy) of nanoribbon orientations in capillary flow cell. In addition, the correlation between the flow rate and nanoribbon orientational distributions could also be determined through the 2D SAXS patterns. We speculate that faster flow rate could lead to stronger anisotropy in 2D SAXS pattern, which could be simulated by a sharper orientational distribution $h(\delta)$. (i.e. Onsager distribution function $\exp[-\sin(\delta/n)]$ with smaller n)

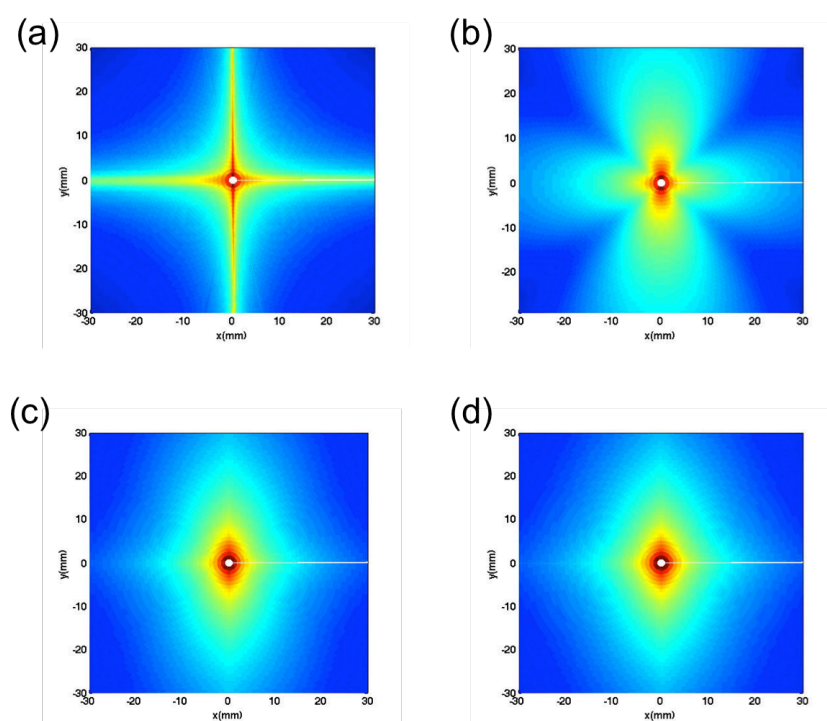


Figure A.2. Simulated 2D SAXS patterns of aligned $C_{16}K_1$ nanoribbon using equation (A.1) and (A.2) with different orientational distributions: (a) Ideally along flow direction, (b) Gaussian distribution, (c) Boltzmann distribution, (d) Onsager distribution. Simulated scattering intensity was scaled from blue (weak) to red (strong).

A.2. Shear-aligned Ribbons Deposited on Substrate

A.1 shows the flow-induced alignment of nanoribbons in solution. The aligned nanoribbons, when deposited on the surface, could also facilitate many other experiments. For instance, AFM image in Figure 5.1b have shown the faceted edges on the high aspect ratio $C_{16}K_1$ nanoribbons. Due to its crystalline nature of molecular packing, we speculate that there might be preferred crystalline orientations with respect to the ribbon morphology. Therefore, the aligned nanoribbons deposited on the solid substrate would be an ideal candidate for this experiment. Grazing Incidence X-ray Diffraction could be used to analyze the intensity variation of in-plane diffraction peaks with respect to the in-plane geometric orientation of the aligned nanoribbons. (Figure A.3). To prepare the aligned nanoribbons on the surface, we drop 20 μ L 4 mM $C_{16}K_1$ solution onto 3 cm \times 1 cm silicon substrate, and continuously shear the solution using a cover slip until the solution dries out on the substrate (Figure A.3a). We anticipate that the shear flow created using this method would align the nanoribbon in a certain degree based on the flow-induced nanoribbon alignment observed in A.1.

The Grazing Incidence X-ray Diffraction was conducted on a Rigaku SmartLab X-ray diffractometer. The sample is cut 1 cm \times 1 cm from above 3 cm \times 1 cm nanoribbon deposited silicon substrate. The incident angle is 0.2° , and the incident slit sizes are selected to produce a spot size 1.5 cm \times 1.5 cm to cover the entire sample during the experiment. The 2θ -chi scan is first conducted to measure the in-plane X-ray diffraction peaks. Figure A.3b shows the diffraction peaks at 1.39 \AA^{-1} and 1.5 \AA^{-1} from the bilayer nanoribbons, which coincide with the two strong peaks observed from solution WAXS experiment (Figure 5.3b). Then the point detector is fixed at the angles where the diffraction peaks are observed, and the aligned

nanoribbons are rotated in-plane to change their geometric orientation. Specifically, in this experiment, we rotate the sample stage in-plane from 0° to 180° so that the nanoribbon orientation are changed from parallel to the incident beam (0°), to perpendicular to the incident beam (90°), and back to parallel to the incident beam (180°). Figure A.3c shows that for both diffraction peaks at 1.39 \AA^{-1} and 1.5 \AA^{-1} , the peak intensity is independent of the in-plane rotation angle, which indicates that there might be no preferential crystalline orientation with respect to the $C_{16}K_1$ nanoribbon morphology.

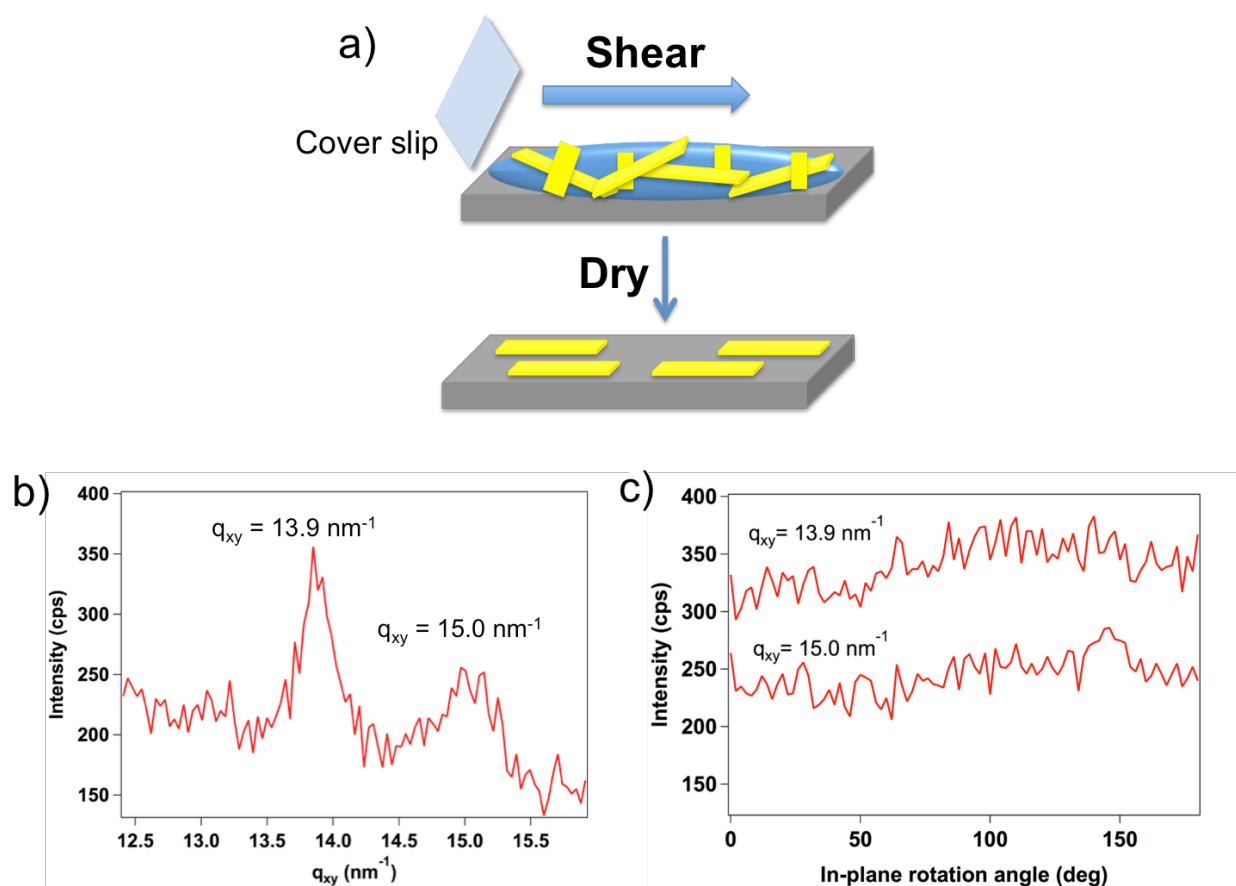


Figure A.3. (a) Aligned $C_{16}K_1$ nanoribbons on solid substrate prepared by shearing the $C_{16}K_1$ solution. (b) Grazing Incidence X-ray diffraction data showing intensity versus in-plane

scattering vector q_{xy} . The diffraction peaks at 13.9 and 15.0 nm^{-1} coincide with solution wide-angle X-ray scattering data. (c) The intensity of both diffraction peaks shows no significant variation when changing the in-plane rotation angle of aligned nanoribbons.

Appendix B. Solution WAXS Analysis on Flat C₁₆K₁ Bilayer

WAXS analysis for C₁₆K₁ bilayer membranes followed the procedure for 3D powder averaging of scattered intensity from a 2D lattice. This was described in our recent publication. Briefly, consider the bilayer 2D lattice in the x-y plane. The scattered intensity can be integrated over the surfaces of a series of spheres of radii q_i (scattering vector magnitudes) to yield the orientationally-averaged intensity profile $I(q)$. Under the assumption of large 2D crystallites[77]:

$$I(q) \propto e^{-q^2 \lambda_D^2} \sum_{hk} \int_0^\pi |F(\vec{q}_{hk}, q_Z)|^2 e^{-\left(\frac{1}{2\sigma_{hk}^2}\right)(q \sin(\theta) - q_{hk})^2} \sigma_{hk} \sqrt{\frac{2\pi \sin(\theta)}{q q_{hk}}} d\theta \quad (\text{B.1})$$

Here, h and k are the Miller indices for a given Bragg reflection, \vec{q}_{hk} is the corresponding reciprocal lattice vector, and is directly related to the oblique lattice constants a , b , γ described in the main text. $q_Z = q \cos(\theta)$ is the scattering vector component normal to the 2D lattice. $F(\vec{q}_{hk}, q_Z)$ is the unit cell form factor resulting from the interference of scattered X-rays from different molecules in a single unit cell. The other factors, including the Gaussian term in the integrand is the effective structure factor arising from the summation of scattering from distinct unit cells. This term is characterized by a spread σ_{hk} ($= 2\pi/L_{hk}$), which is inversely proportional to the correlation length L_{hk} in the direction perpendicular to \vec{q}_{hk} in the lattice plane. The term $e^{-q^2 \lambda_D^2}$ is the effective Debye-Waller factor, which characterizes the fall in scattered intensity with increasing q due to thermal fluctuations or static disorder. In our simulations h and k were independently varied from -4 to 4, and the length $L_{hk} = L_{10} (|h|/(|h|+|k|)) + L_{01} (|k|/(|h|+|k|))$ was used for a given (hk) reflection. This empirical formulation allowed for matching the WAXS data, which showed two strong diffraction peaks with slightly different widths.

In order to calculate unit cell form factor, we assumed two C₁₆K₁ molecules per unit cell and we only focus on the interdigitated tail region. Therefore we can simplify the molecule as perpendicular rods, and the 2D crystal structure consists of these rods arranging into a specific lattice type. The form factor of the rod can be written as

$$F_1(\vec{q}_{hk}, q_z) = \int \rho(\vec{r}) e^{i(\vec{q} \cdot \vec{r})} d^3r \propto \left(\text{sinc}(q_x \cdot \frac{t_x}{2}) \cdot \text{sinc}(q_y \cdot \frac{t_y}{2}) \cdot \frac{e^{iq_z l_z} - 1}{iq_z l_z} \right) \quad (\text{B.2})$$

Here the dimensions of the perpendicular rod are (t_x, t_y, l_z) . q_x and q_y are the x and y components of the reciprocal lattice vector \vec{q}_{hk} and q_z is the z component of the scattering vector. The length of rod l_z is preset to be the SAXS-derived thickness of interdigitated region in C₁₆K₁ bilayer (1.4 nm). Overall, the simulation of the scattered intensity profile was conducted by reasonably tuning the above-mentioned parameters, such as lattice constants, rod dimensions. In the present case, an optimum fit could be found without including the tail tilt ($\alpha = \beta = 0$).

Appendix C. Theoretical Calculation of Ribbon-to-cochleate Transition

C.1. Ribbon-to-sheet Transition

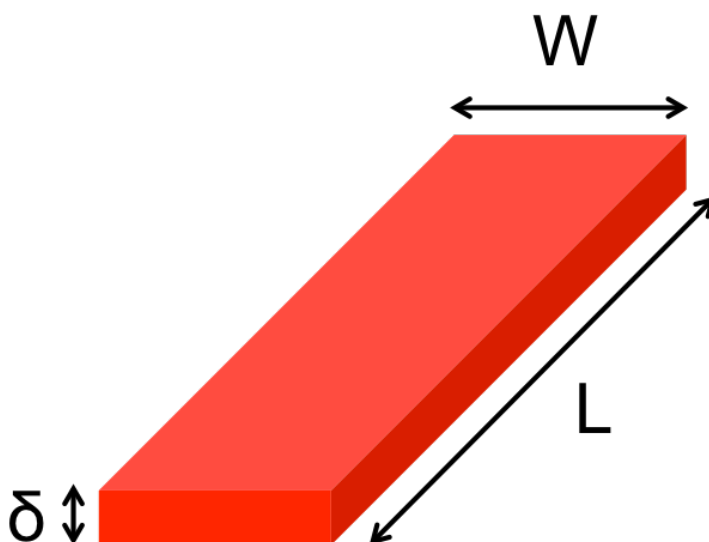


Figure C.1. Simple membrane model with uniform charge density to understand aspect ratio (L/W) change in $C_{16}K_1$ bilayer membrane as the salt concentration increases.

The bilayer ribbon is modeled as a parallelepiped of length L , which extends to μm , thickness δ , which is roughly 4 nm, and width W . The ribbon energy per volume can be written as a sum of electrostatic energy and interfacial energy, which accounts for the contact between the hydrophobic chains and water on the side faces of the ribbon.

$$U_{\text{ribbon}} = U_{\text{electrostatic}} + U_{\text{surface}} \quad (\text{C.1})$$

The electrostatic energy is formulated as:

$$U_{electrostatic} = 2 \int u(r - r') d_r^3 d_{r'}^3 \rho(r) \rho(r') \quad (C.2)$$

$u(r - r')$ is the inter-particle electrostatic potential and is approximated as:

$$u(r - r') \propto l_B \frac{e^{-(r-r')/\lambda_d}}{|r-r'|} \quad (C.3)$$

Here, the Debye length $\lambda_d \propto c^{-1/2}$. When assuming all molecules are charged, $\rho(r)$ is the molecular density of the ribbon, and can be approximated as a constant $\frac{N_T}{V}$, where N_T is the total number of molecules and V is the ribbon volume.

Therefore, equation C.2 can be rewritten as

$$U_{electrostatic} \propto 2 \left(\frac{N_T}{V} \right)^2 k_B T \int l_B \frac{e^{-(r-r')/\lambda_d}}{|r-r'|} d_r^3 d_{r'}^3 \quad (C.4)$$

Since for the $C_{16}K_1$ ribbon, only the top and bottom surfaces are charged, the volume integral can first be thought of as a 2D integral. Let $r - r' = \bar{r}$

$$U_{electrostatic} \propto 2 \left(\frac{N_T}{V} \right)^2 V \delta k_B T \iint_{W,L} l_B \frac{e^{-\bar{r}/\lambda_d}}{\bar{r}} d_{\bar{r}}^2 \quad (C.5)$$

To simplify the equation C.5, we first consider the electrostatic interaction along the length and width of the ribbon

$$U_{electrostatic} \propto 2 \left(\frac{N_T}{V} \right)^2 V \delta k_B T l_B \int_0^W \int_0^L \frac{e^{-\sqrt{x^2+y^2}/\lambda_d}}{\sqrt{x^2+y^2}} dx dy \quad (C.6)$$

Here we distinguish between two conditions: low excess salt and high excess salt.

(1) At low excess salt condition, λ_d is very large, $e^{-\frac{\sqrt{x^2+y^2}}{\lambda_d}} \approx 1 - \frac{\sqrt{x^2+y^2}}{\lambda_d}$, thus C.6 becomes,

$$U_{electrostatic} \propto 2 \left(\frac{N_T}{V} \right)^2 V \delta k_B T l_B \int_0^W \int_0^L \left(\frac{1}{\sqrt{x^2+y^2}} - \frac{1}{\lambda_d} \right) dx dy \quad (C.7)$$

For the integral $\int_0^W \int_0^L \frac{1}{\sqrt{x^2+y^2}} dx dy$, we reformulate this term into a linear integral,

$$\int_0^W \int_0^L \frac{1}{\sqrt{x^2+y^2}} dx dy = \int_0^W \ln \left[\frac{L}{x} + \sqrt{1 + \frac{L^2}{x^2}} \right] dx \quad (C.8)$$

Substituting equation C.8 into C.7 we will have,

$$U_{electrostatic} \propto 2 \left(\frac{N_T}{V} \right)^2 V \delta k_B T l_B \left[-\frac{WL}{\lambda_d} + \int_0^W \ln \left(\frac{L}{x} + \sqrt{1 + \frac{L^2}{x^2}} \right) dx \right] \quad (C.9)$$

(2) At high excess salt condition where λ_d is very small, therefore we can consider the range of electrostatic energy in a small circle (with radius of $3\lambda_d$) about each charged molecule. For the

integral of $\int_0^W \int_0^L \frac{e^{-\frac{\sqrt{x^2+y^2}}{\lambda_d}}}{\sqrt{x^2+y^2}} dx dy$, it can be reformulated as,

$$\int_0^W \int_0^L \frac{e^{-\frac{\sqrt{x^2+y^2}}{\lambda_d}}}{\sqrt{x^2+y^2}} dx dy = \int_0^{3\lambda_d} \int_0^{2\pi} \frac{e^{-\frac{r}{\lambda_d}}}{r} r dr d\theta \quad (C.10)$$

The simplified integral here can be numerical solved, and the final formulation C.11 shows that the electrostatic energy is independent of aspect ratio.

$$U_{electrostatic} \propto 4 \left(\frac{N_T}{V} \right)^2 V \delta k_B T l_B \pi \lambda_d \quad (\text{C.11})$$

Now we have the electrostatic part for our formulation.

The interfacial edge energy part is simple,

$$U_{surface} = 2\gamma(L + W)\delta \quad (\text{C.12})$$

Here γ is the surface tension of hydrocarbon/water interface.

When combining equation C.12 with 11 and 9, we can have ribbon energy per unit volume at low and high salt conditions. Also based on AFM observations, we make a simplifying assumption that the total ribbon area $A = WL$ is independent of aspect ratio $\chi^{-1} = (L/W)$. Thus we can substitute the W and L with ribbon area A and the inverse of aspect ratio χ ,

$$\frac{U_{ribbon}}{V} = \left(\frac{2N_T^2}{VA} \right) k_B T l_B \left[-\frac{A}{\lambda_d} + \int_0^{\sqrt{A\chi}} \ln \left(\frac{\sqrt{A/\chi}}{a} + \sqrt{1 + \frac{A}{\chi a^2}} \right) da \right] + \frac{2\gamma \left(\sqrt{A/\chi} + \sqrt{A\chi} \right)}{A} \quad (\text{C.13})$$

$$\frac{U_{ribbon}}{V} = \left(\frac{4N_T^2}{VA} \right) k_B T l_B \pi \lambda_d + \frac{2\gamma \left(\sqrt{A/\chi} + \sqrt{A\chi} \right)}{A} \quad (\text{C.14})$$

Equation C.13 (low salt) and C.14 (high salt) are plotted in Chapter 5 to understand the relationship between ribbon energy and the ribbon aspect ratio χ^{-1} at different salt conditions.

C.2. Membrane Rolling

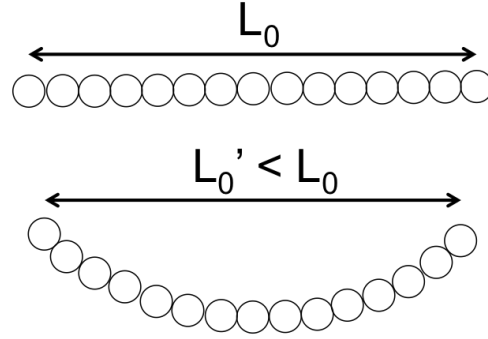


Figure C.2. Model system of an array of charged particles, the array has a fixed contour length L_0 and a spontaneous curvature C_0 .

In order to understand the rolling of the $C_{16}K_1$ membrane, we used a simplified model of an array of charged species. The array was assumed to possess a spontaneous curvature C_0 , and a contour length L_0 that was independent of the curvature of the array. The array energy was assumed to be a sum of electrostatic repulsion energy and the curvature energy. The electrostatic repulsion energy for a straight array of charged species (top configuration in Figure C.2) may be written as:

$$\frac{U_{electrostatic}}{L_0} = 2\rho^2 L_0 \int_{d_0}^{L_0} l_B \frac{e^{-\kappa l}}{l} dl \quad (C.15)$$

Here, ρ is the membrane charge density, and d_0 is the nearest neighbor distance.

If the array had a curvature C_1 , the intermolecular distances will become smaller, resulting in an increase in the electrostatic energy for the array. For instance, the distance between the two ends of the curved array L_0' is smaller than L_0 , and it can be written as,

$$L_0' = \frac{2}{c_1} \sin\left(\frac{c_1 L_0}{2}\right) \quad (\text{C.16})$$

In particular, the electrostatic repulsion energy for lower configuration is

$$\frac{U_{electrostatic}}{L_0} = 2\rho^2 L_0 \int_{d_0}^{L_0} l_B \frac{e^{-\kappa\left(\frac{2}{c_1} \sin\left(\frac{c_1 l}{2}\right)\right)}}{\frac{2}{c_1} \sin\left(\frac{c_1 l}{2}\right)} dl \quad (\text{C.17})$$

and the array curvature energy is

$$\frac{U_{curvature}}{L_0} = \frac{\kappa_c}{2} L_0 (c_1 - c_0)^2 \quad (\text{C.18})$$

Here κ_c is the bending stiffness and c_0 is the spontaneous curvature, which could be set to 1/(75 nm) by measuring the nanotube diameter in Figure 4.4. Combining the C.16, 17 and 18, we are able to numerically calculate the total energy (electrostatic + curvature energy) at different curvature c_1 and salt concentration.

C.3. Interlayer Separation vs. Salt Concentration

In Chapter 5, we used the sum of interlayer van der Waals attraction and electrostatic repulsion energy to calculate the equilibrium interlayer spacing D inside the cochleate structure.

The van der Waals attraction energy U_d and electrostatic repulsion energy U_e are formulated as [64, 78, 79],

$$U_d(\delta, d) = -W \left[\frac{1}{d^2} - \frac{2}{(d+\delta)^2} + \frac{1}{(d+2\delta)^2} \right] \quad (\text{C.19})$$

$$U_e(d) = \frac{32\varepsilon_0\varepsilon_w(k_B T)^2}{q^2\lambda_d} \exp(-d/\lambda_d) \quad (\text{C.20})$$

where δ is the bilayer thickness and d is the aqueous region thickness. The sum of δ and d is the interlayer spacing D . W is the Hamaker constant. q is the electron unit, ε_0 is the vacuum permittivity, ε_w is the dielectric constant of the aqueous solution, k_B is the Boltzmann constant. λ_d is the Debye-Hückel screening length.

Curvature energy of the cochleate is also considered here in addition to the van-deer Waals attraction energy and electrostatic repulsion energy. The curvature energy of a bilayer membrane of area A takes the form of:

$$U_{curvature} = \frac{\kappa_c}{2} \int_A (c_1 + c_2 - c_0)^2 dA \quad (\text{C.21})$$

where κ_c is the bending stiffness, c_1 and c_2 are the principal curvatures, and c_0 is the spontaneous curvature. For cylindrical cochleate structure, since the membrane is curved only along one direction, c_2 can be set to zero. Thus the equation turns into:

$$U_{curvature} = \frac{\kappa_c}{2} L \int_l (c_1 - c_0)^2 dl \quad (\text{C.22})$$

Here L is the cochleate length, and l represents the spiral line of the cochleate. For the cochleate structure with constant interlayer spacing D , the radius of curvature at specific position on spiral line takes the form of

$$r = \frac{D}{2\pi}\theta + r_i \quad (\text{C.23})$$

r_i is the radius of curvature at the innermost end of the spiral line, θ is the rotation angle of the position relative to the innermost end. By using this equation to substitute the curvature c_l in equation C.22, we can have

$$U_{curvature} = \frac{\kappa_c}{2} L \int_0^{\theta_0} \left(\frac{1}{\left(\frac{D}{2\pi}\theta + r_i\right)} - c_0 \right)^2 \left(\frac{D}{2\pi}\theta + r_i\right) d\theta \quad (\text{C.24})$$

θ_0 is the rotation angle between outermost and innermost end of the spiral line, so the outermost radius of cochleate r_o takes the form of $\frac{D}{2\pi}\theta_0 + r_i$. After we analytically solved the integral in equation C.24 and incorporated the parameter r_o , the final formulation of curvature energy of the entire cochleate structure is

$$U_{curvature} = \frac{\kappa_c L \pi}{2D} \left(2 \ln \left(\frac{r_o}{r_i} \right) - 4c_0(r_o - r_i) + (r_o^2 - r_i^2)c_0^2 \right) \quad (\text{C.25})$$

The cochleate membrane area A can be formulated as

$$A = \frac{\pi L}{D} (r_o^2 - r_i^2) \quad (\text{C.26})$$

Therefore the curvature energy per unit area is

$$\frac{U_{curvature}}{A} = \frac{\kappa_c}{2(r_o^2 - r_i^2)} \left(2 \ln \left(\frac{r_o}{r_i} \right) - 4c_0(r_o - r_i) + (r_o^2 - r_i^2)c_0^2 \right) \quad (C.27)$$

Here the curvature energy per unit area is solely dependent on the innermost and outermost radii of the cochleate, not directly related to the interlayer spacing D . Therefore, for the purpose of calculating the equilibrium interlayer spacing D by minimizing the free energy, we neglect the effect from curvature energy.

Appendix D. SAXS and WAXS Data Processing and Fitting

D.1. SAXS/WAXS Data Processing

The raw solution X-ray scattering data collected from APS Sector 5-IDD consists of water, empty and solution sample scans. Each scan has three data files corresponding to SAXS, MAXS and WAXS intensity profiles collected from different 2D detectors. Matlab programs were written to calibrate the X-ray scattering intensity to the absolute intensity scale and subtract the water scattering background from the solution sample scattering. In addition, the SAXS, MAXS and WAXS data are merged to create a complete X-ray scattering intensity profile. Smearred data can also be produced to decrease the noise of scattering intensity profile. The matlab programs can be found in names of 'cal_merge.m', 'Absolute_intensity_water.m', and 'Info.m'. The 'Absolute_intensity_water.m' creates a file for absolute intensity calibration of water at different temperature. 'Info.m' contains the options and parameters for SAXS/WAXS data processing. 'cal_merge.m' is the main data processing program that realize the water background subtraction, absolute intensity calibration, SAXS/MAXS/WAXS data merging, and the data smearing.

D.2. SAXS Data Analysis and Fitting Programs

NIST is mostly used to fit the SAXS intensity profile. It is an excellent macro that can be installed in IgorPro for fitting form factors. This macro has many built-in fitting models such as bilayer, cylindrical or spherical structures that are available to fit different shapes. A very useful

manual of NIST can be found in the macro that describes the fitting equations for each model.

The fitting procedure is as follows

- 1) Create a graph by clicking “Window/ New graph” and select the appropriate x and y data set
- 2) Select the graph window. Click “Graph/Show info” to get the info toolbar that appears below the graph. Then drop the two cursers onto the curve and select the region need to be fitted.
- 3) Click “Data analysis/ Curve fitting”. There are some very basic functions that can be used.
- 4) To build our own fitting equations, we can choose “Function and data/New fit function” and type in the equations.
- 5) In the dialog box “Data option”, click “Cursor” to allow fitting of the selected region of the curve. The data error can be selected in the section “Weighing data”
- 6) Type in an initial guess of the fit in “Coefficients”. The coefficients can be saved by creating a new coefficient wave in the same dialog box
- 7) By clicking “Do it”, IgorPro will fit the data based on the initial guess of the data. One should also fine tune the parameters and try to get the best fit with several trials.

For fitting the SAXS data for mixture of bilayer and cylindrical micelle, the following equation is used to combine the form factor of symmetric bilayer membranes and core-shell cylinders.

$$I(q) = scale \cdot A \cdot \frac{4\pi\{(\rho_h - \rho_w) \cdot [\sin[q(d_h + d_t)] - \sin(qd_t)] + (\rho_t - \rho_w) \sin(qd_t)\}^2}{(d_h + d_t)q^4} + scale \cdot (1 - A) \cdot \frac{\int_0^{\frac{\pi}{2}} f^2(q, \alpha) \sin \alpha d\alpha}{\pi(r+t)^2 L} + background$$

The first term is symmetric bilayer membrane form factor and the second term is core shell cylinder form factor, the function $f(q, \alpha)$ is formulated as

$$f(q, \alpha) = 2(\rho_{core} - \rho_{shell})\pi r^2 L \cdot \frac{\sin\left(\frac{qL\cos\alpha}{2}\right) \cdot J_1(qr\sin\alpha)}{\left(\frac{qL\cos\alpha}{2}\right) \cdot (qr\sin\alpha)} + 2(\rho_{shell} - \rho_w)\pi(r+t)^2 L \cdot \frac{\sin\left(\frac{qL\cos\alpha}{2}\right) \cdot J_1(q(r+t)\sin\alpha)}{\left(\frac{qL\cos\alpha}{2}\right) \cdot (q(r+t)\sin\alpha)}$$

In the above equations, ρ_h and ρ_t represent the electron densities of hydrophilic and hydrophobic regions of bilayer membrane. d_t and d_h are the thicknesses of corresponding layers. ρ_{core} and ρ_{shell} are the electron densities of cylindrical micelle core and shell. r is the core radius of cylindrical micelle and t is the headgroup shell thickness. L is the total length of the cylindrical micelle. A represents the volume ratio of bilayer membrane in the mixture of bilayer membrane and cylindrical micelle.

Reference:

- [1] G.L. Eakins, R. Pandey, J.P. Wojciechowski, H.Y. Zheng, J.E.A. Webb, C. Valery, P. Thordarson, N.O.V. Plank, J.A. Gerrard, J.M. Hodgkiss, Functional Organic Semiconductors Assembled via Natural Aggregating Peptides, *Adv Funct Mater*, 25 (2015) 5640-5649.
- [2] J.G. Mei, K.R. Graham, R. Stalder, S.P. Tiwari, H. Cheun, J. Shim, M. Yoshio, C. Nuckolls, B. Kippelen, R.K. Castellano, J.R. Reynolds, Self-Assembled Amphiphilic Diketopyrrolopyrrole-Based Oligothiophenes for Field-Effect Transistors and Solar Cells, *Chem Mater*, 23 (2011) 2285-2288.
- [3] M.S. Arnold, M.O. Guler, M.C. Hersam, S.I. Stupp, Encapsulation of carbon nanotubes by self-assembling peptide amphiphiles, *Langmuir*, 21 (2005) 4705-4709.
- [4] W.J. Chen, L.Y. Zheng, M.L. Wang, Y.W. Chi, G.N. Chen, Preparation of Protein-like Silver-Cysteine Hybrid Nanowires and Application in Ultrasensitive Immunoassay of Cancer Biomarker, *Anal Chem*, 85 (2013) 9655-9663.
- [5] T. Bramer, N. Dew, K. Edsman, Pharmaceutical applications for cationic mixtures, *J Pharm Pharmacol*, 59 (2007) 1319-1334.
- [6] V.P. Torchilin, Recent advances with liposomes as pharmaceutical carriers, *Nat Rev Drug Discov*, 4 (2005) 145-160.
- [7] D. Peer, J.M. Karp, S. Hong, O.C. Farokhzad, R. Margalit, R. Langer, Nanocarriers as an emerging platform for cancer therapy, *Nat Nanotechnol*, 2 (2007) 751-760.
- [8] Y. Elani, R.V. Law, O. Ces, Vesicle-based artificial cells as chemical microreactors with spatially segregated reaction pathways, *Nat Commun*, 5 (2014).

- [9] J.H. Collier, P.B. Messersmith, Phospholipid strategies in biomineralization and biomaterials research, *Annu Rev Mater Res*, 31 (2001) 237-263.
- [10] H.G. Cui, M.J. Webber, S.I. Stupp, Self-Assembly of Peptide Amphiphiles: From Molecules to Nanostructures to Biomaterials, *Biopolymers*, 94 (2010) 1-18.
- [11] M.P. Hendricks, K. Sato, L.C. Palmer, S.I. Stupp, Supramolecular Assembly of Peptide Amphiphiles, *Accounts Chem Res*, 50 (2017) 2440-2448.
- [12] J.N. Israelachvili, Intermolecular and Surface Forces, 3rd Edition, Intermolecular and Surface Forces, 3rd Edition, DOI (2011) 1-674.
- [13] R. Nagarajan, Molecular packing parameter and surfactant self-assembly: The neglected role of the surfactant tail, *Langmuir*, 18 (2002) 31-38.
- [14] V.V. Kumar, Complementary Molecular Shapes and Additivity of the Packing Parameter of Lipids, *P Natl Acad Sci USA*, 88 (1991) 444-448.
- [15] C. Huang, J.T. Mason, Geometric Packing Constraints in Egg Phosphatidylcholine Vesicles, *P Natl Acad Sci USA*, 75 (1978) 308-310.
- [16] J.P. Schneider, Responsive hydrogels from the intramolecular folding and self-assembly of a designed peptide, *Abstr Pap Am Chem S*, 225 (2003) U321-U321.
- [17] A. Aggeli, I.A. Nyrkova, M. Bell, R. Harding, L. Carrick, T.C.B. McLeish, A.N. Semenov, N. Boden, Hierarchical self-assembly of chiral rod-like molecules as a model for peptide beta-sheet tapes, ribbons, fibrils, and fibers, *P Natl Acad Sci USA*, 98 (2001) 11857-11862.
- [18] A. Dehsorkhi, V. Castelletto, I.W. Hamley, Self-assembling amphiphilic peptides, *J Pept Sci*, 20 (2014) 453-467.

- [19] L. Tjernberg, W. Hosiya, N. Bark, J. Thyberg, J. Johansson, Charge attraction and beta propensity are necessary for amyloid fibril formation from tetrapeptides, *J Biol Chem*, 277 (2002) 43243-43246.
- [20] C.Y. Leung, L.C. Palmer, B.F. Qiao, S. Kewalramani, R. Sknepnek, C.J. Newcomb, M.A. Greenfield, G. Vernizzi, S.I. Stupp, M.J. Bedzyk, M.O. de la Cruz, Molecular crystallization controlled by pH regulates mesoscopic membrane morphology, *ACS Nano*, 6 (2012) 10901-10909.
- [21] C.Y. Leung, L.C. Palmer, S. Kewalramani, B.F. Qiao, S.I. Stupp, M.O. de la Cruz, M.J. Bedzyk, Crystalline polymorphism induced by charge regulation in ionic membranes, *P Natl Acad Sci USA*, 110 (2013) 16309-16314.
- [22] E.T. Pashuck, S.I. Stupp, Direct Observation of Morphological Transformation from Twisted Ribbons into Helical Ribbons, *J Am Chem Soc*, 132 (2010) 8819-+.
- [23] T.J. Moyer, H.G. Cui, S.I. Stupp, Tuning Nanostructure Dimensions with Supramolecular Twisting, *J Phys Chem B*, 117 (2013) 4604-4610.
- [24] H.G. Cui, A.G. Cheetham, E.T. Pashuck, S.I. Stupp, Amino Acid Sequence in Constitutionally Isomeric Tetrapeptide Amphiphiles Dictates Architecture of One-Dimensional Nanostructures, *J Am Chem Soc*, 136 (2014) 12461-12468.
- [25] D.M. Marini, W. Hwang, D.A. Lauffenburger, S.G. Zhang, R.D. Kamm, Left-handed helical ribbon intermediates in the self-assembly of a beta-sheet peptide, *Nano Lett*, 2 (2002) 295-299.
- [26] D.T. Bong, T.D. Clark, J.R. Granja, M.R. Ghadiri, Self-assembling organic nanotubes, *Angew Chem Int Edit*, 40 (2001) 988-1011.

- [27] D.M. Jens Als-Nielsen, Elements of Modern X-ray Physics, Second Edition ed., Wiley 2011.
- [28] L.A. Feigin, Svergun, D.I., Structure Analysis by Small-Angle X-Ray and Neutron Scattering, 1987.
- [29] L.X. Fan, M. Degen, S. Bendle, N. Grupido, J. Ilavsky, The Absolute Calibration of a Small-Angle Scattering Instrument with a Laboratory X-ray Source, J Phys Conf Ser, 247 (2010).
- [30] C.J. Newcomb, T.J. Moyer, S.S. Lee, S.I. Stupp, Advances in cryogenic transmission electron microscopy for the characterization of dynamic self-assembling nanostructures, Curr Opin Colloid In, 17 (2012) 350-359.
- [31] S.M. Zhang, M.A. Greenfield, A. Mata, L.C. Palmer, R. Bitton, J.R. Mantei, C. Aparicio, M.O. de la Cruz, S.I. Stupp, A self-assembly pathway to aligned monodomain gels, Nat Mater, 9 (2010) 594-601.
- [32] J.D. Hartgerink, E. Beniash, S.I. Stupp, Self-assembly and mineralization of peptide-amphiphile nanofibers, Science, 294 (2001) 1684-1688.
- [33] J.D. Hartgerink, E. Beniash, S.I. Stupp, Peptide-amphiphile nanofibers: A versatile scaffold for the preparation of self-assembling materials, P Natl Acad Sci USA, 99 (2002) 5133-5138.
- [34] H. Cui, T. Muraoka, A.G. Cheetham, S.I. Stupp, Self-Assembly of Giant Peptide Nanobelts, Nano Lett, 9 (2009) 945-951.
- [35] J.A. Lehrman, H.G. Cui, W.W. Tsai, T.J. Moyer, S.I. Stupp, Supramolecular control of self-assembling terthiophene-peptide conjugates through the amino acid side chain, Chem Commun, 48 (2012) 9711-9713.

- [36] Y.S. Velichko, S.I. Stupp, M.O. de la Cruz, Molecular simulation study of peptide amphiphile self-assembly, *J Phys Chem B*, 112 (2008) 2326-2334.
- [37] S. Tsonchev, K.L. Niece, G.C. Schatz, M.A. Ratner, S.I. Stupp, Phase diagram for assembly of biologically-active peptide amphiphiles, *J Phys Chem B*, 112 (2008) 441-447.
- [38] Y.R. Chen, H.X. Gan, Y.W. Tong, pH-Controlled Hierarchical Self-Assembly of Peptide Amphiphile, *Macromolecules*, 48 (2015) 2647-2653.
- [39] A. Ghosh, M. Haverick, K. Stump, X.Y. Yang, M.F. Tweedle, J.E. Goldberger, Fine-Tuning the pH Trigger of Self-Assembly, *J Am Chem Soc*, 134 (2012) 3647-3650.
- [40] T.J. Moyer, J.A. Finbloom, F. Chen, D.J. Toft, V.L. Cryns, S.I. Stupp, pH and Amphiphilic Structure Direct Supramolecular Behavior in Biofunctional Assemblies, *J Am Chem Soc*, 136 (2014) 14746-14752.
- [41] M.J. Webber, C.J. Newcomb, R. Bitton, S.I. Stupp, Switching of self-assembly in a peptide nanostructure with a specific enzyme, *Soft Matter*, 7 (2011) 9665-9672.
- [42] R.R. Netz, Charge regulation of weak polyelectrolytes at low- and high-dielectric-constant substrates, *J Phys-Condens Mat*, 15 (2003) S239-S244.
- [43] G. Vernizzi, D.S. Zhang, M.O. de la Cruz, Structural phase transitions and mechanical properties of binary ionic colloidal crystals at interfaces, *Soft Matter*, 7 (2011) 6285-6293.
- [44] J.F. Nagle, S. Tristram-Nagle, Structure of lipid bilayers, *Bba-Rev Biomembranes*, 1469 (2000) 159-195.
- [45] A. Pawar, C. Bothiraja, K. Shaikh, A. Mali, An insight into cochleates, a potential drug delivery system, *Rsc Adv*, 5 (2015) 81188-81202.

- [46] A. Rosler, G.W.M. Vandermeulen, H.A. Klok, Advanced drug delivery devices via self-assembly of amphiphilic block copolymers, *Adv Drug Deliver Rev*, 64 (2012) 270-279.
- [47] J.B. Matson, S.I. Stupp, Self-assembling peptide scaffolds for regenerative medicine, *Chem Commun*, 48 (2012) 26-33.
- [48] M. Yemini, M. Reches, J. Rishpon, E. Gazit, Novel electrochemical biosensing platform using self-assembled peptide nanotubes, *Nano Lett*, 5 (2005) 183-186.
- [49] R.V. Kazantsev, A.J. Dannenhoffer, A.S. Weingarten, B.T. Phelan, B. Harutyunyan, T. Aytun, A. Narayanan, D.J. Fairfield, J. Boekhoven, H. Sai, A. Senesi, P.I. O'Dogherty, L.C. Palmer, M.J. Bedzyk, M.R. Wasielewski, S.L. Stupp, Crystal-Phase Transitions and Photocatalysis in Supramolecular Scaffolds, *J Am Chem Soc*, 139 (2017) 6120-6127.
- [50] A.S. Weingarten, R.V. Kazantsev, L.C. Palmer, M. McClendon, A.R. Koltonow, A.P.S. Samuel, D.J. Kiebal, M.R. Wasielewski, S.I. Stupp, Self-assembling hydrogel scaffolds for photocatalytic hydrogen production, *Nat Chem*, 6 (2014) 964-970.
- [51] Y. Kaufman, A. Berman, V. Freger, Supported Lipid Bilayer Membranes for Water Purification by Reverse Osmosis, *Langmuir*, 26 (2010) 7388-7395.
- [52] K. Nagarsekar, M. Ashtikar, F. Steiniger, J. Thamm, F. Schacher, A. Fahr, Understanding cochleate formation: insights into structural development, *Soft Matter*, 12 (2016) 3797-3809.
- [53] D. Papahadjopoulos, W.J. Vail, K. Jacobson, G. Poste, Cochleate Lipid Cylinders - Formation by Fusion of Unilamellar Lipid Vesicles, *Biochim Biophys Acta*, 394 (1975) 483-491.
- [54] E.D. Sone, E.R. Zubarev, S.I. Stupp, Semiconductor nanohelices templated by supramolecular ribbons, *Angew Chem Int Edit*, 41 (2002) 1705-+.

- [55] Z.W. Yao, M.O. de la Cruz, Electrostatics-Driven Hierarchical Buckling of Charged Flexible Ribbons, *Phys Rev Lett*, 116 (2016).
- [56] J. Adamcik, R. Mezzenga, Adjustable twisting periodic pitch of amyloid fibrils, *Soft Matter*, 7 (2011) 5437-5443.
- [57] A.S. Weingarten, R.V. Kazantsev, L.C. Palmer, D.J. Fairfield, A.R. Koltonow, S.I. Stupp, Supramolecular Packing Controls H₂ Photocatalysis in Chromophore Amphiphile Hydrogels, *J Am Chem Soc*, 137 (2015) 15241-15246.
- [58] A.K. Rappe, C.J. Casewit, K.S. Colwell, W.A. Goddard, W.M. Skiff, Uff, a Full Periodic-Table Force-Field for Molecular Mechanics and Molecular-Dynamics Simulations, *J Am Chem Soc*, 114 (1992) 10024-10035.
- [59] R. Aveyard, D.A. Haydon, Thermodynamic Properties of Aliphatic Hydrocarbon-Water Interfaces, *T Faraday Soc*, 61 (1965) 2255-&.
- [60] L. Picas, F. Rico, S. Scheuring, Direct Measurement of the Mechanical Properties of Lipid Phases in Supported Bilayers, *Biophys J*, 102 (2012) L1-L3.
- [61] K. Norrish, The Swelling of Montmorillonite, *Discuss Faraday Soc*, DOI (1954) 120-134.
- [62] C.C. Tester, S. Aloni, B. Gilbert, J.F. Banfield, Short- and Long-Range Attractive Forces That Influence the Structure of Montmorillonite Osmotic Hydrates, *Langmuir*, 32 (2016) 12039-12046.
- [63] K. Nagarsekar, M. Ashtikar, J. Thamm, F. Steiniger, F. Schacher, A. Fahr, S. May, Electron Microscopy and Theoretical Modeling of Cochleates, *Langmuir*, 30 (2014) 13143-13151.
- [64] S. Komura, H. Shirotori, T. Kato, Phase behavior of charged lipid bilayer membranes with added electrolyte, *J Chem Phys*, 119 (2003) 1157-1164.

- [65] G.M. Cooper., *The Cell*, 2nd edition ed.2000.
- [66] T. Lian, R.J.Y. Ho, Trends and developments in liposome drug delivery systems, *J Pharm Sci*, 90 (2001) 667-680.
- [67] A. Sharma, U.S. Sharma, Liposomes in drug delivery: progress and limitations, *Int J Pharm*, 154 (1997) 123-140.
- [68] K. Hristova, D. Needham, Phase-Behavior of a Lipid Polymer-Lipid Mixture in Aqueous-Medium, *Macromolecules*, 28 (1995) 991-1002.
- [69] M. Lyte, M. Shinitzky, A Special Lipid Mixture for Membrane Fluidization, *Biochim Biophys Acta*, 812 (1985) 133-138.
- [70] R. Zantl, L. Baicu, F. Artzner, I. Sprenger, G. Rapp, J.O. Radler, Thermotropic phase behavior of cationic lipid-DNA complexes compared to binary lipid mixtures, *J Phys Chem B*, 103 (1999) 10300-10310.
- [71] A.A. Gurtovenko, M. Patra, M. Karttunen, I. Vattulainen, Cationic DMPC/DMTAP lipid bilayers: Molecular dynamics study, *Biophys J*, 86 (2004) 3461-3472.
- [72] T. Nii, F. Ishii, Encapsulation efficiency of water-soluble and insoluble drugs in liposomes prepared by the microencapsulation vesicle method, *Int J Pharm*, 298 (2005) 198-205.
- [73] J.V. Selinger, M.S. Spector, J.M. Schnur, Theory of self-assembled tubules and helical ribbons, *J Phys Chem B*, 105 (2001) 7157-7169.
- [74] J.V. Selinger, J.M. Schnur, Theory of Chiral Lipid Tubules, *Phys Rev Lett*, 71 (1993) 4091-4094.
- [75] S. Forster, M. Konrad, P. Lindner, Shear thinning and orientational ordering of wormlike micelles, *Phys Rev Lett*, 94 (2005).

- [76] M. Trebbin, D. Steinhauser, J. Perlich, A. Buffet, S.V. Roth, W. Zimmermann, J. Thiele, S. Forster, Anisotropic particles align perpendicular to the flow direction in narrow microchannels, *P Natl Acad Sci USA*, 110 (2013) 6706-6711.
- [77] B. Harutyunyan, A. Dannenhoffer, S. Kewalramani, T. Aytun, D.J. Fairfield, S.I. Stupp, M.J. Bedzyk, Molecular Packing of Amphiphilic Nanosheets Resolved by X-ray Scattering, *J Phys Chem C*, 121 (2017) 1047-1054.
- [78] M.Y. Lin, L. Li, F. Qiu, Y.L. Yang, Effect of added monovalent electrolytes on the myelin formation from charged lipids, *J Colloid Interf Sci*, 348 (2010) 505-510.
- [79] J.R. Huang, L.N. Zou, T.A. Witten, Confined multilamellae prefer cylindrical morphology, *Eur Phys J E*, 18 (2005) 279-285.